Michael Hollerer, BSc

AFM morphology investigation of pentacene OFETs at the semiconductor-metal contact

MASTER THESIS

For obtaining the academic degree
Diplom-Ingenieur

Master Programme of
Technical Physics

Graz University of Technology

Supervisor:
Ao.Univ.-Prof.i.R. Dipl.-Ing. Dr.techn. Adolf Winkler
Institute of Solid State Physics

Graz, January 2015

EIDESSTATTLICHE ERKLÄRUNG

AFFIDAVIT

Ich erkläre an Eides statt, dass ich die vorliegende Arbeit selbstständig verfasst, andere als die angegebenen Quellen/Hilfsmittel nicht benutzt, und die den benutzten Quellen wörtlich und inhaltlich entnommenen Stellen als solche kenntlich gemacht habe. Das in TUGRAZonline hochgeladene Textdokument ist mit der vorliegenden Masterarbeit/Diplomarbeit/Dissertation identisch.

I declare that I have authored this thesis independently, that I have not used other than the declared sources/resources, and that I have explicitly indicated all material which has been quoted either literally or by content from the sources used. The text document uploaded to TUGRAZonline is identical to the present master's thesis/diploma thesis/doctoral dissertation.

_____ _____

Datum / Date Unterschrift / Signature

Abstract

Organic electronics promise to take over profit-yielding niche-markets not covered by conventional silicon technology. Although organic materials have been investigated for years the underlying principles of charge transport are not yet fully understood. In this work the frequently used pentacene organic field effect transistor (OFET) is prepared under ultra-high vacuum condition to investigate basic questions such as the amount of layers contributing to the charge transport and the empirically found *best substrate temperature* at deposition for high performance devices. In our setup the sample can be tempered in a range of 150 K to 800 K and *in-situ* electrical measurements can be conducted throughout the experiment. The coplanar bottom-gate structure allows for successive ad- and desorption cycles without the sample leaving the system. Doing several cycles of ad- and desorption of pentacene establishes a well defined carbon contamination in the SiO_2 channel and on the gold electrodes. A contamination-free substrate can be achieved by sputter-cleaning. Auger electron spectroscopy (AES) is used to verify the carbon levels for the previously stated sample preparations. The main focus of this work lies on *ex-situ* atomic force microscopy (AFM) investigation of pentacene film growth at various temperatures and on differently prepared substrates as well as putting them into relation with corresponding electrical measurements. A special emphasis is put on the pentacene film development in the dielectric-electrode transition area. Additionally, a novel model is proposed explaining dewetting phenomena occurring above the previously stated *best substrate temperature*.

Kurzfassung

Organische Elektronik verspricht profitreiche Nischenmärkte zu übernehmen welche nicht von konventioneller Siliziumtechnologie abgedeckt werden. Obwohl organische Materialien schon seit vielen Jahren untersucht werden, sind die Grundlagen des Ladungstransports nur ungenügend erforscht. In dieser Arbeit wird der häufig verwendete organische Feld-Effekt-Transistor (OFET) mit Pentacen im Ultra-Hoch Vakuum hergestellt und untersucht um grundlegende Fragen, wie die Anzahl der beitragenden Schichten zum Ladungstransport und die empirisch gefundene *beste Substrattemperatur* für die Herstellung von Hochleistungstransistoren, zu klären. In unserem Aufbau kann die Probe von 150 K bis 800 K temperiert werden. Gleichzeitig können während des gesamten Experiments elektrische *in-situ* Messungen durchgeführt werden. Die koplanare bottom-gate Struktur erlaubt aufeinanderfolgende Ad- und Desorptionszyklen, ohne dass die Probe aus dem Aufbau entfernt werden muss. Mehrere Zyklen von Ad- und Desorption hinterlassen eine wohldefinierte Kohlenstoffkontaminierung im SiO_2 Kanal und auf den Goldelektroden. Ein reines Substrat kann wiederum durch Argon-Sputtern erzielt werden. Auger-Elektronen Spektroskopie wird genutzt um die Kohlenstoffkontamination zu quantifizieren. Der Fokus dieser Arbeit liegt auf *ex-situ* Untersuchungen des Pentacen Schichtwachstums mittels Rasterkraftmikroskopie (AFM) bei unterschiedlichen Temperaturen und unterschiedlich präparierten Substraten sowie deren Zusammenhang mit elektrischen Messungen. Ein besonderer Schwerpunkt liegt auf dem Pentacen Schichtwachstum im Dielektrikum-Elektrodenübergang. Zusätzlich wird ein neues Modell für das Auftreten von *Dewetting*-Phänomenen bei Temperaturen über der zuvor genannten *besten Substrattemperatur* vorgestellt.

Danksagung

An dieser Stelle möchte ich mich bei allen Personen bedanken, die mich bei der Erstellung dieser Arbeit unterstützt haben. Vor allem gilt der Dank meiner Familie für die persönliche wie auch finanzielle Unterstützung während der Studienzeit.

Ein besonderer Dank gilt meinem Professor Adolf Winkler, Ao.Univ.-Prof., der mir diese Arbeit ermöglicht hat, der stets für mich ansprechbar war und mir die Freiheit gelassen hat, die Arbeit nach eigenen Vorstellungen zu entwickeln.

Ebenfalls bedanken möchte ich bei meinem Betreuer Roman Lassnig, Dipl. Ing., der mich in die Grundlagen der Thematik und die Bedienung der Geräte einführte und mich bei der Durchführung der Experimente begleitete.

Bedanken möchte ich mich auch bei allen Mitarbeitern des Instituts für Festkörperphysik, für anregende Diskussionen und Vorschläge, die mit Ihrer Arbeit zum gelingen meiner Arbeit beigetragen haben.

Großer Dank gebührt auch meinen Freunden und Kommilitonen, sowie meiner Freundin, die während der Studiumszeit stets ein wichtiger Anlaufpunkt bei Problemen und Motivationskrisen waren.

Contents

1 Introduction and Motivation **3**

2 Fundamentals **5**

2.1 Organic Semiconductors 5

2.1.1 Pentacene 6

2.2 Growth Mechanism 9

2.2.1 Sticking coefficient 9

2.2.2 Growth Modes 10

2.2.3 Dewetting 12

2.3 Organic Field Effect Transistor - OFET 13

2.3.1 Transistor Structure 13

2.3.2 Basic Operation 14

2.4 Electrical Characterization 15

2.4.1 Output Characteristic 19

2.4.2 Transfer Characteristic 20

2.5 Transport Mechanism 22

2.5.1 Carrier Injection 22

2.5.2 Charge Transport 24

3 Experimental Setup **27**

3.1 Vacuum System 27

3.1.1 Sample and sample holder 28

3.1.2 Knudsen Cell 30

3.2 Experimental Methods 31

3.2.1 Quadrupole Mass Spectrometry - QMS 31

3.2.2 Thermal Desorption Spectroscopy - TDS 31

3.2.3 Sputter Cleaning 32

3.2.4 Auger Electron Spectroscopy - AES . . . 33
3.3 Electrical Measurements . . . 33
3.4 Atomic Force Microscopy - AFM . . . 34
3.4.1 Gwyddion . . . 37

4 Results and Discussion **39**
4.1 Surface Characterization . . . 39
4.1.1 Surface Roughness . . . 39
4.1.2 Electrode-Dielectric Transition . . . 41
4.2 Quantifying Pentacene Deposition . . . 43
4.2.1 AFM Thickness Evaluation . . . 43
4.2.2 Thickness Evaluation using TDS . . . 45
4.2.3 Layer Estimation for Thick Films . . . 47
4.3 Optical Measurements . . . 49
4.4 Pentacene Film-Morphology Correlation with Electrical Properties . . . 51
4.4.1 Electrical Properties: Function of Temperature and Coverage . . . 51
4.4.2 Morphology of 1.4 ML Films as a Function of Temperature . . . 53
4.4.3 Morphology of 6.8 ML Films as a Function of Temperature . . . 58
4.4.4 Morphology of 22.7 ML Films as a Function of Temperature . . . 64
4.5 Influence of Sputter Cleaning . . . 68
4.5.1 AFM Investigation . . . 68
4.5.2 Electrical Characterization . . . 69
4.6 Threshold Voltage . . . 70

5 Conclusion **75**

6 Appendix **77**
6.1 Matlab Analysis Code . . . 77
6.1.1 LabView Data Processing . . . 77
6.1.2 Extraction of Mobility and Threshold Voltages . . . 81

List of Figures **89**

7 Bibliography **93**

1 Introduction and Motivation

Organic electronics are approaching profit-yielding niche-markets, not covered by conventional silicon technology. The possibility of room temperature patterning and processing of organic materials allows for the fabrication of low-cost, large-area electronic devices on various substrates. This is a major advantage in comparison to inorganic technology which is mostly restricted to solid substrates. The promise of highly functionalized, flexible materials attracts economical interest and encourages worldwide industrial and academic research on the field of organic electronics [1, 2].

Although various organic materials have been successfully implemented in organic field effect transistors the underlying principles are only poorly understood. Different theoretical models have been proposed to best describe charge transport processes, but are only insufficiently able to explain measurement observations [3, 4, 5]. Additionally, commonly used organic materials are often subject to device degradation in ambient atmosphere and are not yet stable enough for industrial purposes.

Pentacene ($C_{22}H_{14}$) advanced to be todays working horse for the investigation of organic electronics because of its excellent growth behavior and its outstanding field effect mobilities of up to $3\,\frac{\mathrm{cm}^2}{\mathrm{Vs}}$, exceeding even amorphous silicon [6, 7]. A frequently used setup for the realization of working organic transistors is the deposition of pentacene in vacuum conditions on a SiO_2 substrate, acting as the gate dielectric and using gold as source and drain electrodes. Although the growth behavior of pentacene and its dependencies on the deposition parameters has been subject to intense investigation [8, 9], similarly prepared transistors often exhibit great variations in their electric properties. Various investigations on how many layers of the pentacene film contribute to the charge transport show huge discrepancies (2 monolayers to 20 monolayers) [8, 10, 11]. The often stated *best substrate temperature* of $\sim$330 K [12] for the fabrication of high performance pentacene transistors is another obscurity, as there are no supporting theoretical models.

For the investigation of the stated problems a coplanar bottom-gate structure (SiO_2 and gold) is used in an ultra-high vacuum chamber, achieving pressures of 1×10^{-8} mbar.

A special sample holder achieves temperature regulation for the sample of 150 K to 800 K, allowing successive ad- and desorption cycles without flooding the vacuum chamber. The pentacene deposition is monitored by a quartz microbalance (QCM) allowing for sub-monolayer deposition accuracy. Because we isolate the sample from the temperature control, electrical characterization of the sample via BNC-feedthroughs is possible at all times. Additionally, the setup is equipped with a sputter gun for cleaning the substrate as well as an Auger electron spectrometer (AES) for analysis of the established surface. A quadrupole mass spectrometer (QMS) is used for residual gas analysis as well as thermal desorption spectroscopy (TDS) on established pentacene films. An *ex-situ* atomic force microscope (AFM) complements the setup with a possible characterization of the pentacene film morphology.

This work focuses on relating *ex-situ* AFM film morphology measurements to *in-situ* electrical transistor characterizations for various deposition parameters. The previously stated problems are investigated and proposals for solutions are deduced.

2 Fundamentals

2.1 Organic Semiconductors

Organic materials are molecules or compounds of molecules mainly consisting of carbon and hydrogen atoms. Carbon compounds exhibiting alternating single and double bonds are called conjugated compounds. The sp^2 hybridization of the carbon atoms lead to the formation of σ and π bonds. The π bonds exhibit overlaps along the backbone of the molecule which leads to connected de-localized electron states. Strong overlaps of π bonds may lead to the transport of electrical charges and the presence of semiconducting properties. This composition is found in many polymers and aromatic ring structures. In fig. 2.1 and 2.2 the structural formula and the orbital overlap of the molecule benzene is depicted.

In molecular orbital theory one differentiates between the highest occupied molecular orbital (HOMO) and the lowest unoccupied molecular orbital (LUMO). The energy difference between the bonding π and the anti-bonding π^* state is smaller than for the stronger bound σ states, the π orbitals represent HOMO and LUMO and are therefore responsible for the charge transport.

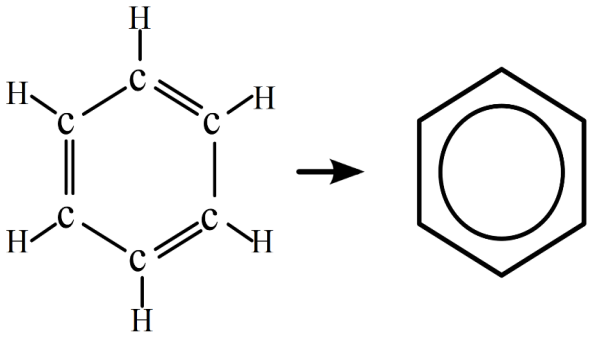

Figure 2.1: Structural and skeletal formula of benzene. The skeletal formula is often also depicted with three double lines instead of an inner circle.

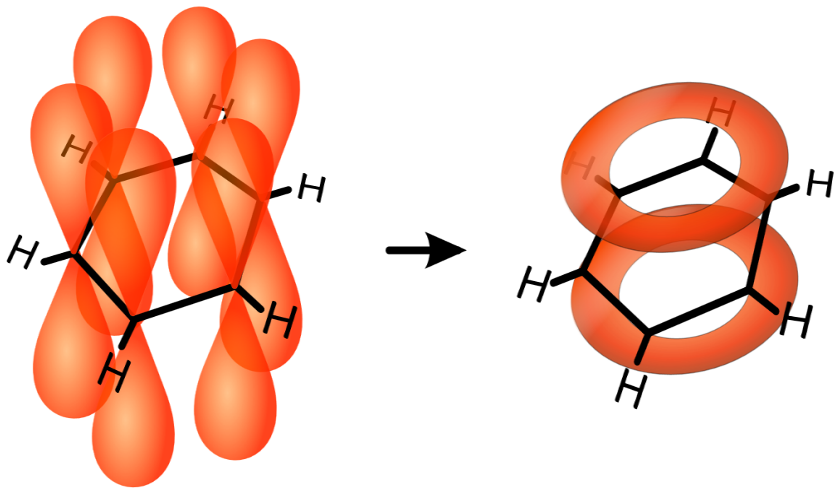

Figure 2.2: On top of the benzene structure the π_z orbital of each carbon atom is depicted. These are connecting to a de-localized orbital state which is schematically visualized on the right hand side [13].

Most organic materials exhibit p-type properties. This is due to the fact that conjugated materials favor the loss over the gain of an electron [14]. Additionally, the work function of the most common electrode materials are a better fit to the energy of the highest occupied molecular orbital (HOMO) then to the lowest unoccupied orbital (LUMO) level and therefore favor hole injection.

2.1.1 Pentacene

Pentacene is a polycyclic aromatic hydrocarbon consisting of five linearly-fused benzene rings. It exhibits one of the greatest hole mobilities for organic semiconductors of $3\,\mathrm{cm}^2/\mathrm{V\,s}$ [6, 7] outperforming even amorphous silicon. If evaporated on non-reactive substrates such as SiO_2 pentacene is shown to develop an exceptionally intact wetting layer of standing molecules (long axis perpendicular to the surface) with islands on top of it (Stranski-Krastanov mode).

It is also one of the first molecule that could be visualized with STM and AFM imaging (Fig. 2.3). Because of its excellent growth behavior together with its high hole mobilities pentacene advanced to be one of the most investigated organic semiconductors. Depending on the manufacturing procedures, crystal phases with different lattice spacings of 15.4, 14.4 and 14.1 Å have been observed, commonly named the *thin film*,

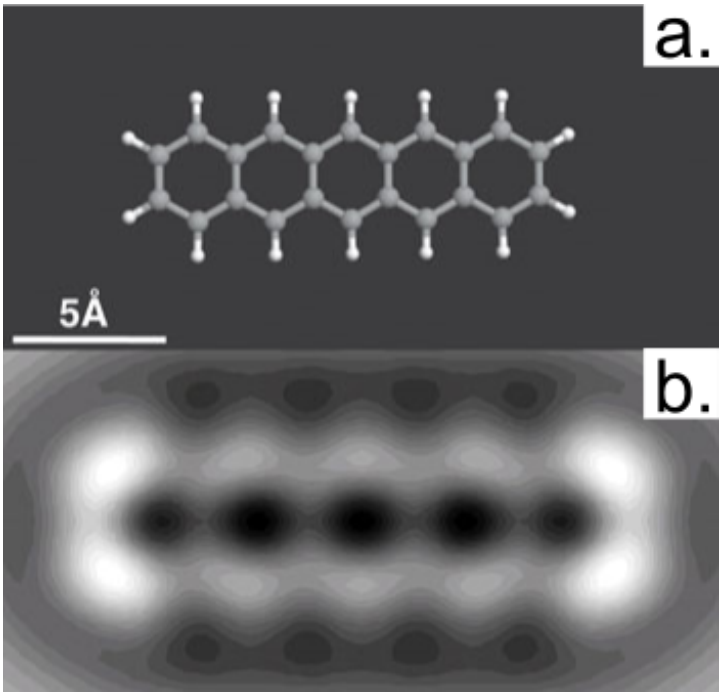

Figure 2.3: Structure of Pentacene. **(a.)** Ball and stick model. **(b.)** STM image with modified tip [15].

the *bulk* and the *single crystal* phase, respectively [8, 6, 16]. The lattice parameters of pentacene bulk and thin film phase are given in fig. 2.4. Although pentacene single crystals don't exhibit grain boundaries, the highest reported charge carrier mobilities (μ =0.3 $cm^2/V\,s$ to 2.2 $cm^2/V\,s$) don't supersede those of pentacene thin film transistors [17, 18].

This suggests a better intrinsic mobility of thin films due to a better inner crystal structure which can be attributed to a more perpendicular growth of the thin film phase leading to a better orbital overlap (ch. 2.1). By evaporation on polar substrates such as SiO_2 pentacene develops in the thin film phase. There are hints that the molecular tilt starts out perfectly perpendicular with a slowly increasing tilt at higher film thicknesses. As the charge transport is mostly attributed to the lowest layers this is further increasing the emphasis on the influence of the molecular tilt [12, 19].

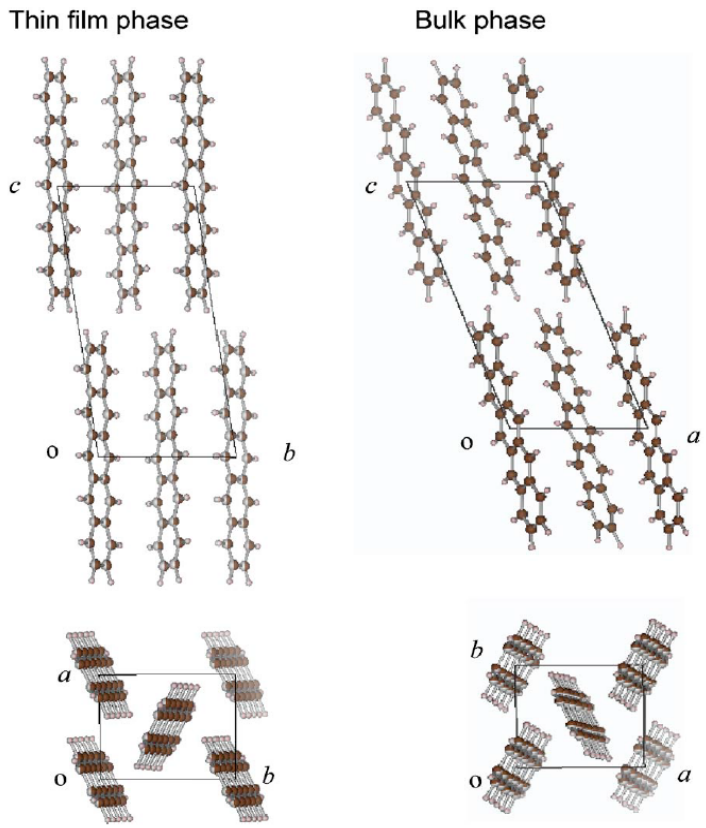

Figure 2.4: Pentacene in thin film and bulk phase with inter-planar spacings of d_{001} = 15.4 Å and d_{001} = 14.4 Å, respectively. The single crystal phase exhibits an even smaller spacing of d_{001} = 14.1 Å. Within the a - b plane pentacene is ordered in a herringbone structure. The lattice parameters of the thin film phase are: a = 0.593 nm , b = 0.756 nm, c = 1.565 nm, α =98.6°, β = 93.3°, γ = 89.8°. The cell volume is V = 0.693 nm^3 [20]

If evaporated on more reactive surfaces, such as gold, a wetting layer of lying pentacene molecules (long axis parallel to the surface) with big islands of lying pentacene molecules on top of it develops. In the case of polycrystalline gold with very small grains, even the development of islands of standing molecules on a wetting layer of lying molecules can occur as depicted in fig. 2.5.

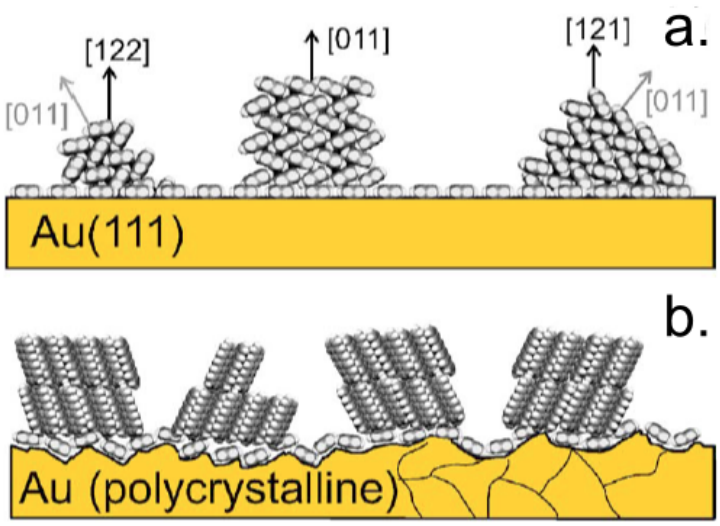

Figure 2.5: Growth of pentacene on gold substrates. **(a.)** Development of islands consisting of lying monomers on Au(111). **(b.)** Islands of standing monomers developing on polycrystalline surface exhibiting many domain boundaries. [21]

2.2 Growth Mechanism

The growth of crystalline thin films is governed by kinetics and thermodynamics. The microscopic structure of the films determine their semiconducting properties. It is therefore necessary to understand the growth mechanisms of thin films and their dependence on adsorption parameters.

2.2.1 Sticking coefficient

To describe the adsorption of the evaporated material on a surface by physical vapor deposition (PVD) several parameters have to be considered. The impingement rate I gives the number of particles per unit area and second:

$$I = \frac{p}{\sqrt{2\pi m k_b T}} \tag{2.1}$$

with the pressure p, the Boltzmann constant k_b, the mass of the impinging molecule m and the surface temperature T. To determine the resulting coverage by the impingement rate we need to consider how many particles will stick to the surface. Incoming particles may be reflected inelastically or adsorb at the surface. Adsorbed particles can

exist in a weakly bound state, allowing diffusion on the surface, before adsorbing to an energetically more favorable position or even re-desorption. The amount of particles permanently adsorbed r_{ads} is then defined by the sticking probability or sticking coefficient s:

$$r_{ads} = sI \tag{2.2}$$

The sticking coefficient is sensitive to the adsorbing surface, the surface temperature and sometimes also the kinetic energy of the incoming particles. Since the surface is changing with the amount of adsorbed particles the sticking coefficient is also dependent on the coverage. Especially for a Stranski-Krastanov growth the sticking coefficient of the first monolayer may differ from those of the succeeding layers.

2.2.2 Growth Modes

There are three primary modes (Fig. 2.6) characterizing the growth of a crystalline film on a crystalline substrate [22]. Depending on the bond strength in between the molecules and between the molecules and the surface, different growth modes will occur. The appearance of different modes of epitaxial films is therefore highly dependent on the substrate surface with its micro structure. Furthermore, it is also influenced by the temperature, deposition rate, ambient environment and film coverage.

The **Volmer-Weber** mode occurs if the bonds between the adsorbate molecules are stronger than the bonds between adsorbate and adsorbent, resulting in the growth of three dimensional islands. If the adhesive bonds between adsorbate and adsorbent are stronger, a two dimensional layer growth or **Frank-van der Merwe** mode will occur. The **Stranski-Krastanov** mode occurs in between the two former mentioned modes, and appears when the first monolayer (ML) passivates the surface-adsorbent interaction and the ongoing growth is dominated by cohesive bonding forces.

Inorganic adsorbates usually consist of atoms (or dimers) and are therefore mostly spherical and rather isotropic. They are assumed to chemisorb at the surface and are dominated by strong covalent and ionic bonds. Organic molecules are bigger, exhibit a wide range of shapes and are very anisotropic. The most significant difference is the reliance on weak Van-der-Waals interactions between the molecules and between molecules and surface [8]. For small organic molecules a sticking coefficient of $s = 1$ is generally assumed. Contributing mechanisms for film growths are the adsorption of

monomers, their diffusion on the substrate, the formation of islands once the critical island size is reached, the enlargement of those islands by incorporation of diffusing molecules and, if present, the re-desorption of adsorbed monomers [23].

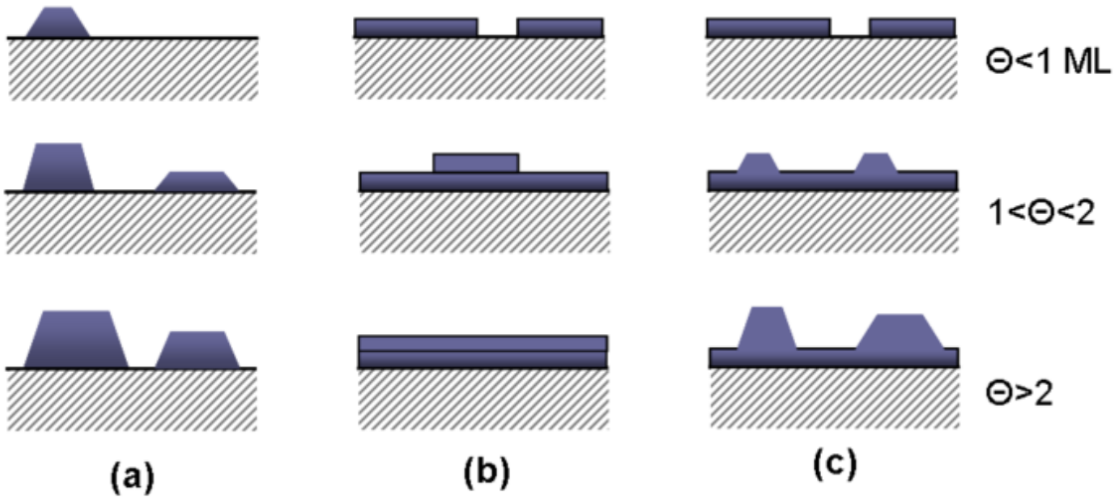

Figure 2.6: Growth modes of epitaxial films. **(a.)** *Island growth* or Volmer-Weber growth (VW). **(b.)** *Layer-by-layer growth* or Frank-van der Merwe growth (FM). **(c.)** *Layer plus island growth* or Stranski-Krastanov growth (SK). All modes are shown for three different film coverages (Θ). The coverage is given in Monolayers (ML) of film adsorbent.

Pentacene Film Growth

The growth of pentacene on SiO_2 is consistent with the Stranski-Krastanov model. The development of the wetting layer is described by a diffusion-mediated model where the amount of pentacene molecules to form a stable island is four (critical island size $i = 3$). The island growth on top of the intact layers is described by a distributed model [8]. The interaction between pentacene does not seem to be influenced by the substrate and the critical island size hence is similar to $i = 3$ of the first monolayer [24].

The nucleation of the islands strongly depends on temperature and deposition rate since it alters the surface mobility of the monomers, as well as the probability of finding another monomer within their diffusion length. The sticking coefficient s at room

temperature is close to unity. A particular process is the adsorption on energetically favorable sites close to a substrate transition as it is the case at an electrode-dielectric junction. This specific problem will be discussed in ch. 4.4.

The diffusion length of pentacene monomers on SiO_2 and on pentacene is in the μm range and not restricted to transport within their plane. Monomers may overcome step edges if its energy is larger then the *Ehrlich Schwoebel barrier*. *Zhu et al.* propose the presence of up and down diffusion of monomers which is depicted in fig. 2.7. Observing the development of pentacene thin film roughnesses they even conclude a *hopping up* dominated film growth [25].

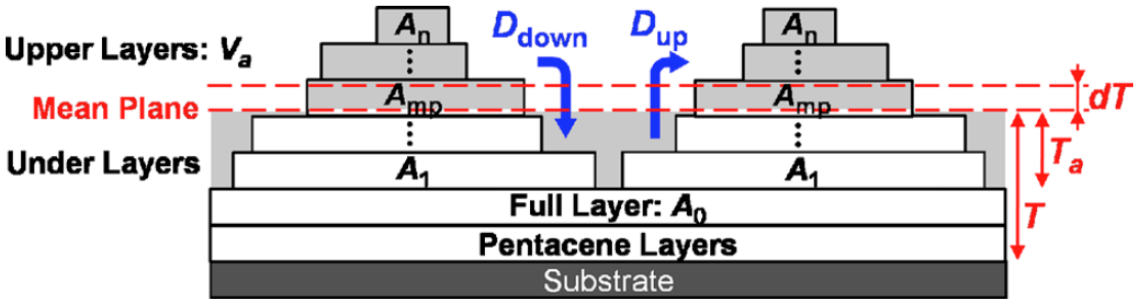

Figure 2.7: Diffusing pentacene monomers may overcome the Ehrlich-Schwoebel barrier in both directions. Roughness analysis suggest a greater probability for hopping up terraces D_{up} then for hopping down D_{down} [25].

2.2.3 Dewetting

Although many adsorbents exhibit the development of an intact wetting layer these films often proof to be unstable even at room temperature. Thus *dewetting* of the wetting layer may take place, resulting in the development of ad-layer islands and bare substrate surface. This process is driven by minimization of the surface energy. Recent studies show that this process is thermally activated and shows a minor dependence on the coverage. Dewetting was proven to occur for higher temperatures, for pentacene namely with dewetting thresholds of 325 K and 340 K for SiO_2 and Au respectively. Dewetting is also present at room temperature although on a larger timescale [26].

2.3 Organic Field Effect Transistor - OFET

Contrary to the well established metal-oxide-semiconductor field-effect transistors (MOSFET's) organic transistors are based on semiconducting organic compounds (Ch. 2.1). Against former prevailing opinion that only metals and semi-metals were conductive, *Shirakawa* was the first to show evidence for the conductive polymer of *Polyacetylene* in 1976 [27] for which he was awarded the Nobel prize in 2000. Since then many other conductive organic materials have been found that are now widely investigated. Although until now the only organic electronic devices to enter competitive market are organic LED's, the run for cheap, flexible and printable organic electronic circuits is on its height.

The great advantage of OFETs is that the manufacturing of the devices can be accomplished in a moderate temperature range around room temperature. The relatively low performance in comparison to silicon technology is therefore compensated by the possibility of light and cheap processing of devices on large and flexible substrates. Due to its prominent electronic properties and its growth behavior the organic compound of *pentacene* (2.1.1) advanced to be todays *working horse* for the investigation of organic semiconductor properties.

2.3.1 Transistor Structure

Since one of the basic requirements for organic semiconductors to compete with inorganic technology is thin and flexible devices, it needs to be applicable in thin film technology. There are several ways to realize transistor setups for thin films which are generally referred to as *thin film transistors* (TFTs) or *organic thin film transistors* (OTFTs) when using organic semiconductors. A thin film transistor is a special type of a field effect transistor although both expressions, OTFT and OFET, are often used for the same device in literature. Fig. 2.8 shows the nomenclature for the possible setups.

Each setup serves specific purposes depending on film manufacturing and growth mechanisms as well as electrical properties. For the investigation of transistor characteristics depending on film growth we choose a coplanar bottom-gate structure allowing us consecutive ad- and desorption cycles of organic films in UHV conditions without reconnecting the specimen.

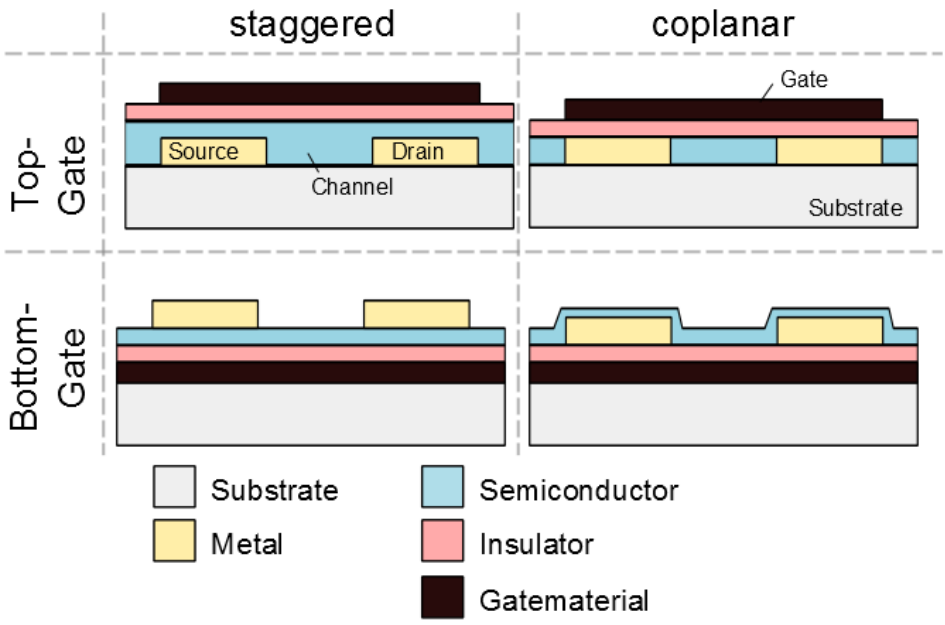

Figure 2.8: Nomenclature of transistor structures for thin semiconducting films [28]. The figure shows a matrix of bottom and top gate contacted devices with SC between gate and electrodes (*staggered*) or on the dielectric (*coplanar*).

2.3.2 Basic Operation

A field effect transistor (FET) consists of three electrical connections named **Gate**, **Source** and **Drain**. The geometrical setup is depicted in figure 2.9. The working principle of the FET is that only with the application of a voltage (U_{GS}) at the gate contact the source-drain current (I_{DS}) can be controlled. A biased gate will establish a field across the insulator (gate dielectric) which results in the accumulation of charge carriers in between the electrodes. The charge carriers form a *channel* connecting the source and the drain contacts. Depending on the prefix of the voltage either negative charge carriers (electrons) or positive ones (holes) will be drawn to the interface. If there is an additional voltage applied between the drain and the source electrode (U_{DS}) a current will flow between the electrodes. The performance of FETs is often characterized by their charge carrier mobility, switching time and on/off current ratio (Ch. 2.4).

In contrast to MOSFETs, organic field effect transistors are operated in the accumulation regime rather then the inversion regime. This implies that the off-current is of the same prefix as the on-current (negative or positive current). Although there are

profound differences in the operation mode of OFETs and MOSFETs the theoretical description for current/voltage characteristics of MOSFETs are used to quantify OFET performances.

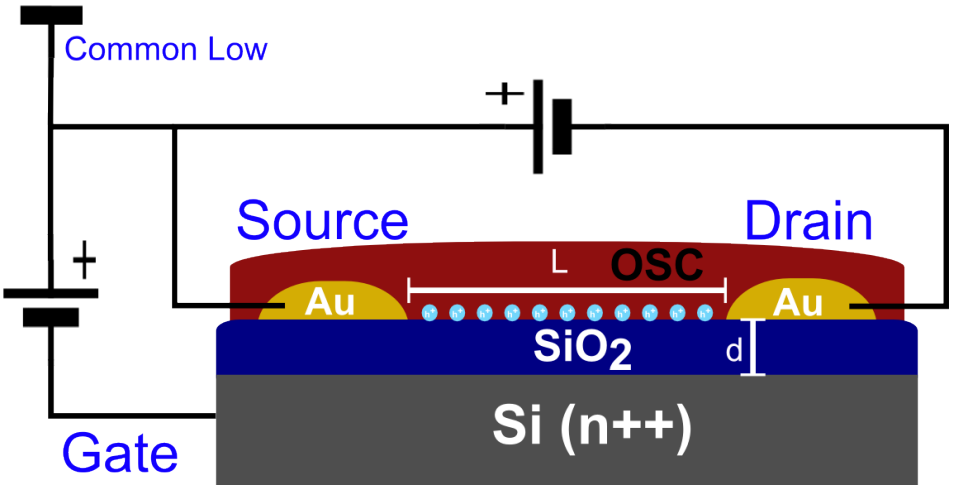

Figure 2.9: Geometrical setup of a coplanar bottom gate transistor. On top of the conducting gate substrate (highly n or p doped Si) is an insulator (SiO_2) of thickness **d**. Two electrodes (Au) are placed onto the insulator with an interspace of **L**. The length of the electrodes perpendicular to the paper plane is the channel-width **W**. On top of this structure an organic semiconductor (OSC) is deposited. Additionally the circuitry for a p-type transistor is depicted. A negative gate bias accumulates positive charge carriers (holes) at the interface. An additional bias drags the positive carriers from the positive source electrode through the channel to the negative drain electrode.

2.4 Electrical Characterization

In MOSFET technology the mobility of charge carriers μ describes the relation between the drift velocity v_d of a charge with an applied electrical field E:

$$v_d = \mu E \tag{2.3}$$

For a current solely dependent on the drift of the charges, a drain current I_D at a position x can be defined for a given charge density $Q(x)$ and an applied electrical field $E(x)$.

$$I_D(x) = W\mu Q(x)E(x) \tag{2.4}$$

with the charge carrier mobility μ and the channel width W. However, a charge carrier density is only present if the gate is biased high enough to accumulate any charges. As soon as a negative U_{GS} is applied, positive charges will accumulate at the semiconductor-dielectric interface to compensate the electrical field. In practice, defects at the interface will trap charge carriers permanently, leading to the compensation of the field without contributing to the charge transport. Thus a certain threshold has to be reached to fill all traps before mobile charge carriers can be accumulated. The voltage needed to accumulate enough carriers to create a conducting channel between source and drain is called threshold voltage U_{Th}. Therefore the charges at the surface need to be expressed with regard to the effective field induced by the effective voltage over the gate dielectric with its capacitance per unit area C_I:

$$Q = C_I(U_{GS} - U_{Th}) \tag{2.5}$$

If an additional drain-source voltage U_{DS} is applied the potential towards the gate $U(x)$ varies with the position x between source and drain from $U(0) = 0$ at source to $U(L) = U_{DS}$ at drain. If we introduce this change of the effective voltage as an addend in eq. 2.5 we obtain:

$$Q(x) = C_I(U_{GS} - U_{Th} - U(x)) \tag{2.6}$$

Substituting equation 2.6 for $Q(x)$ in equation 2.4 and using $dU(x)/dx = E(x)$ as an expression for the electric field we obtain equation 2.7. Integration of this equation yields equation 2.8.

$$I_D(x)\mathrm{d}x = W\mu C_I(U_{GS} - U_{Th} - U(x))\mathrm{d}U(x) \tag{2.7}$$

$$I_D = \frac{W\mu C_I}{L}\left((U_{GS} - U_{Th})U_{DS} - \frac{U_{DS}^2}{2}\right) \tag{2.8}$$

with the channel length L, the channel width W and C_I the capacitance per unit area of the gate dielectric. This equation defines the current, flowing from source to drain, as solely dependent on the applied voltages U_{GS} and U_{DS} once one deduces the threshold voltage U_{Th}. To derive this equation a linear potential drop across the channel

is presumed, which is also known as the *gradual channel approximation*. This is not always fulfilled because OFETs exhibit a deviating behavior especially in the saturation regime [29]. Furthermore, a constant mobility along the channel is assumed which is not the case for OFETs which show a definite V_{GS} dependence and are influenced by electrode-semiconductor contact resistances [30].

Although many things are not or only poorly taken into account, the equation is widely used in the quantification of OFETs. In chapter 2.4.2 the impact of the assumptions on the extraction of the threshold voltage U_{Th} and the charge carrier mobility μ by use of equation 2.8 will be discussed in more detail.

With respect to the derived equation the operation of an OFET can be divided into the *linear regime* and the *saturation regime* (Fig. 2.10).

Linear Regime

If the effective gate voltage $U_{GS} - U_{Th}$ is large compared to U_{DS}, the current I_D grows linearly with the applied voltage U_{DS} (Fig. 2.10.a). If U_{GS} is large enough, many charge carriers are present at the interface and I_D is only restricted by the channel and contact resistance. The resistance along the channel remains the same, although a nonlinear contact resistance effect might be superimposed on the linear rise (Ch. 2.4.1). Eq. 2.8 can be rewritten for $U_{DS} << U_{GS} - U_{Th}$ by neglecting the quadratic term:

$$I_D = \frac{W \mu C_I}{L} (U_{GS} - U_{Th}) U_{DS} \tag{2.9}$$

The linear mobility can then be expressed as:

$$\mu_{lin} = \frac{L}{W C_I U_{DS}} \frac{\mathrm{d}I_D}{\mathrm{d}U_{GS}} \tag{2.10}$$

Saturation Regime

If U_{DS} is large compared to $U_{GS} - U_{Th}$, the current I_D shows a saturating behavior (Fig. 2.10.b). The electric field $E(x)$ disappears at the drain contact when U_{DS} supersedes $U_{GS} - U_{Th}$. The conducting channel is *pinched off* at the drain electrode and the depletion area approaches source with increasing U_{DS}. As a result I_D is limited by the space charge in the depleted region. Equation 2.8 can now be rewritten for $U_{DS} >> U_{GS} - U_{Th}$ by substituting $U_{DS} = (U_{GS} - U_{Th})$:

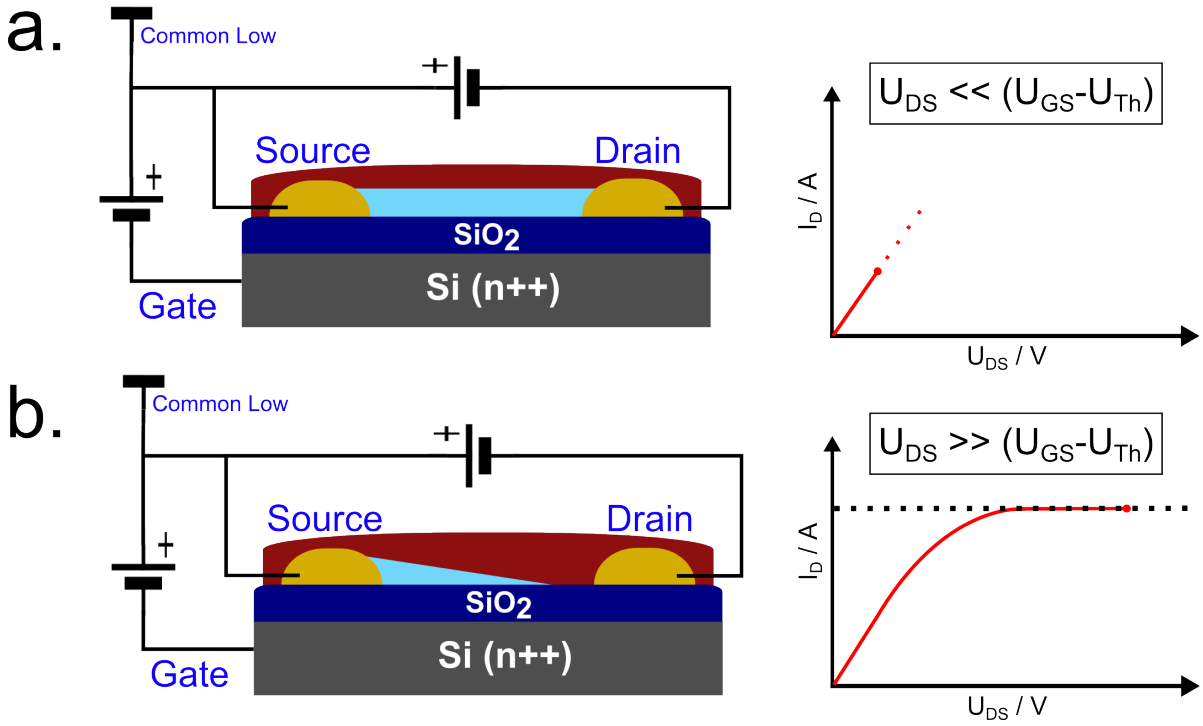

Figure 2.10: OFET operating regimes with schematic output characteristic. **(a.)** OFET in the linear regime. The conducting channel expands over the whole channel width. The corresponding I/U graph depicts a linear rise of I_D with V_{DS}. **(b.)** OFET in the saturation regime. The conducting channel decays as it nears the drain contact. Eventually it cuts off within the channel. The current is limited by the remaining space charges as soon as the conducting channel pinches off at $U_{DS} = U_{Sat}$. The corresponding graph shows the linear rise until U_{Sat} and the saturated current thereafter.

$$I_D = \frac{W\mu C_I}{2L}(U_{GS} - U_{Th})^2 \tag{2.11}$$

This results in a saturation mobility of:

$$\mu_{sat} = \frac{2L}{WC_I}\left(\frac{\mathrm{d}\sqrt{I_D}}{\mathrm{d}U_{GS}}\right)^2 \tag{2.12}$$

2.4.1 Output Characteristic

For the output characteristic U_{DS} is sweeped for fixed values of U_{GS} and I_D is measured (Fig. 2.11.a). Linear and saturation regime are clearly distinguishable and well defined. In the saturation regime an ongoing rise of I_D with U_{DS} can be observed especially for higher U_{GS}. This asymptotic behavior is mainly attributed to channel length modulation (effective shortening of channel length due to pinch-off shift). Other influences are contact resistance and mobility dependencies on U_{DS} as well as charge transport in the depleted semiconductor zone [31]. As for the linear regime an ohmic behavior and a bulk limited charge transport can be assumed.

An example for an output curve exhibiting a pronounced non-linear behavior or S-shape in the linear rise is given in 2.11.b. A non-ohmic behavior of the contact resistance is superimposed on the linear resistance of the inner channel conductance. The S-shaped slope indicates high injection barriers likely caused by an improper connection of the OSC film with the electrode [32].

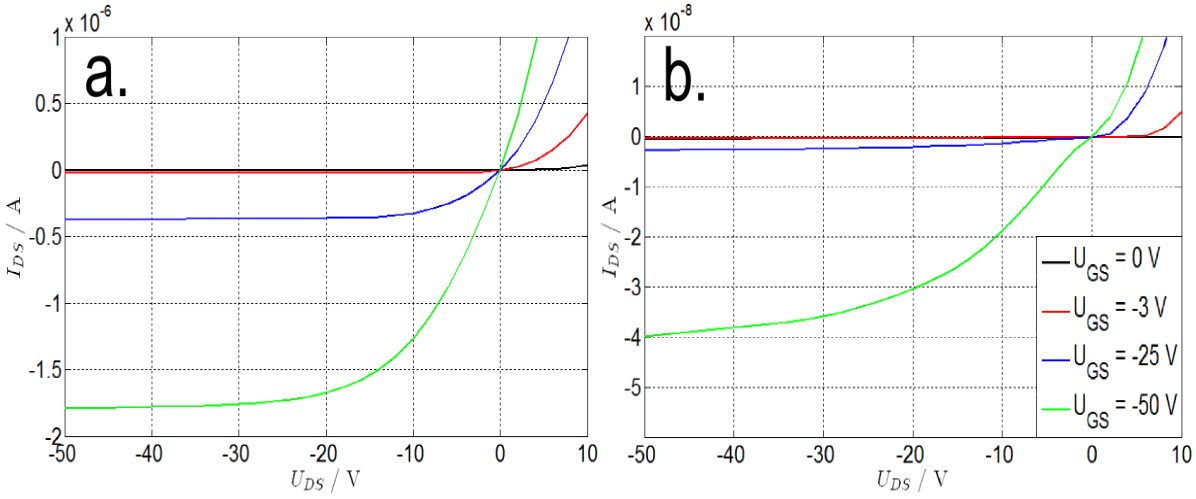

Figure 2.11: Output curves of self manufactured pentacene OFETs. **(a.)** The saturation and the linear regime can be easily distinguished. The former exhibits an almost perfect linear rise which indicates perfect ohmic behavior without contact limitation. The saturation for lower U_{GS} flattens out smoothly whereas for higher U_{GS} the current exhibits an asymptotic behavior. **(b.)** The linear regime exhibits an S-shaped slope indicating a contact limited charge transport behavior.

2.4.2 Transfer Characteristic

The transfer characteristic is obtained by sweeping U_{GS} at constant U_{DS} and measuring I_D. Many characteristic quantities can be derived from this measurement and performance and stability can be judged by its form. Figure 2.12.a depicts a typical transfer curve starting out smoothly and then sharply changing into a quadratic rise. A hysteresis can be observed between forward and backward sweep which is mostly attributed to the filling of shallow traps [10].

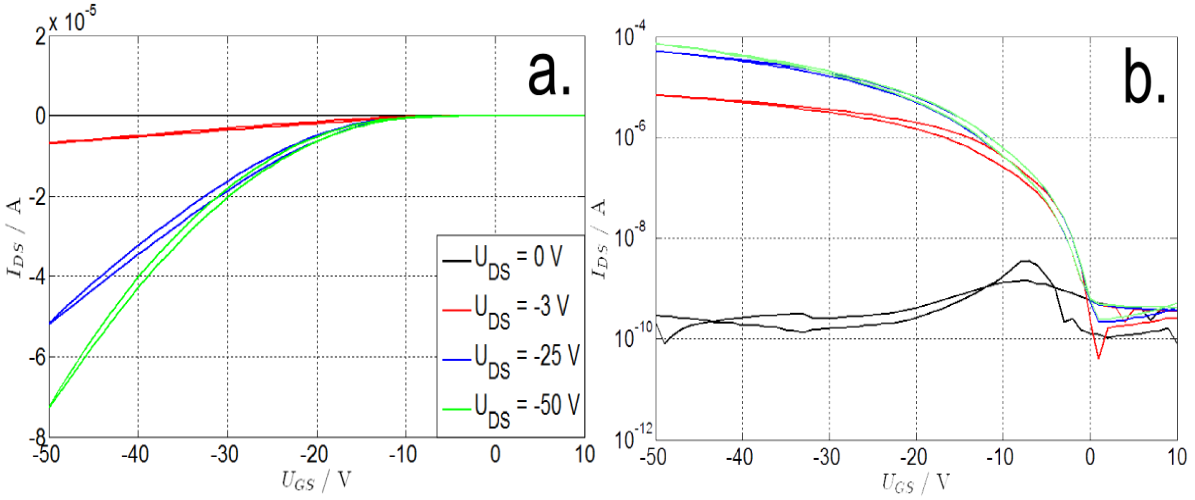

Figure 2.12: Transfer curves of self manufactured pentacene OFETs. **(a.)** Transfer curve for different U_{DS}. Since pentacene OFETs are p-type transistors I_D is negative. **(b.)** The semilog plot of the absolute I_D values is a common representation of the transfer curve. Contrary to the linear scaling the noise of the off current is clearly visible. The ratio between on and off current is taken from this representation and given in order of magnitude (here 10^5) for $U_{DS} = -50\,\mathrm{V}$.

To emphasize the switching behavior the transfer curve is often depicted in a semilogarithmic representation (Fig. 2.12.b). Because the current spreads over various orders of magnitude in this illustration the off current with its noise can be seen and compared to the on current. This on/off ratio is an important quantity for transistors and is given in powers of ten. The region in between on and off current is called the subthreshold region. The steeper the subthreshold-slope the faster a transistor can be operated. The reciprocal value is called the subthreshold-swing which states the volts (U_{GS}) needed to

apply to raise I_D by a decade and is usually given in mV/dec. Both on/off ratio and subthreshold-swing are crucial operational specifications for a working transistor. Additionally, the *switch-on voltage* U_{SO}, where I_D starts growing exponentially, is extracted from this representation. It marks the gate voltage needed to fill all traps and start forming a conducting channel. It is not to be confused with the threshold voltage U_{Th} indicating the voltage needed to establish a fully formed channel with ohmic behavior.

Threshold Voltage and Charge Carrier Mobility

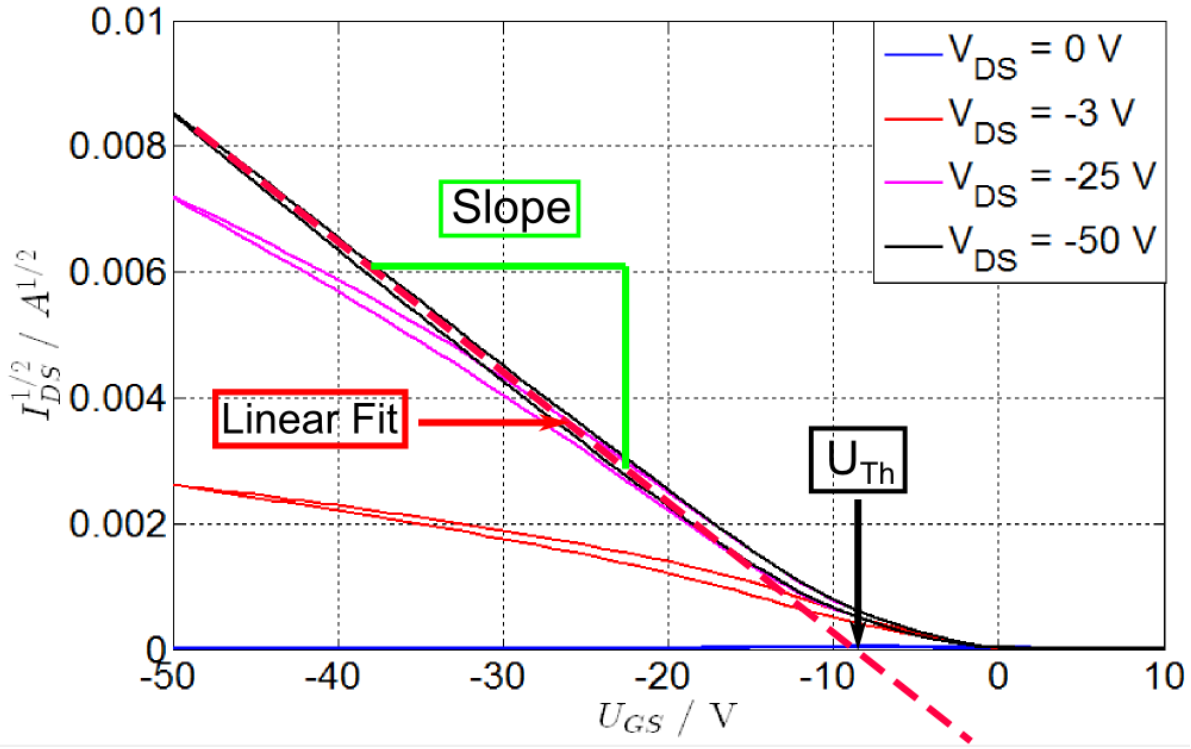

Figure 2.13: A square root representation of a transistor transfer characteristic. The continuous black line was measured for a fixed U_{DS} of -50 V. It is therefore, assuming a negative U_{Th}, operating in the saturation regime ($U_{DS} >> U_{GS} - U_{Th}$). A line is fitted (dashed red line) to the linear part of the transfer curve, yielding the interception point, the threshold voltage U_{Th} and the slope of the line.

The threshold voltage U_{Th} for the saturation regime is estimated out of the square root plot of the transfer curve. A linear fit is made for the upper linear part of the

transfer curve[1]. The intercept of the fitted line with the abscissa marks the threshold voltage (Fig. 2.13).

The threshold voltage is by definition a rather vague quantity and is also often derived by manually extending the linear part and reading the threshold voltage of the x-axis. To deduce the saturation mobility, the slope of the transfer curve in the saturation regime and the square-root representation $\left(\frac{\mathrm{d}\sqrt{I_D}}{\mathrm{d}U_{GS}}\right)$ is put into eq. 2.12. To obtain the linear mobility the slope of the transfer curve in the linear regime and the linear representation $\left(\frac{\mathrm{d}I_D}{\mathrm{d}U_{GS}}\right)$ is put in eq. 2.10. As already mentioned in ch. 2.3.2 the equations only hold approximately for OFET technology. Together with the introduced error by the estimation of V_{Th} one has to consider the trustworthiness of the absolute value of the calculated mobility.

By automating the extraction of U_{Th} we assure the objective comparability among our transistors, allowing us to interpret performance trends in terms of transistor mobilities rather then comparing absolute values. Although the extraction process lacks accuracy it is widely used in research as a vague comparison for transistor performance.

2.5 Transport Mechanism

Compared to the band-model charge transport of inorganic semiconductors the charge transport mechanism of organic thin films has to be described differently. Although a *band-like* transport is successfully used to describe the transport in single crystals, even if only for very low temperatures, polycrystalline films show a deviating behavior and need a different theoretical description accordingly [14]. In the following the charge transport is split into its main components. The carrier injection (Ch. 2.5.1), explaining the injection of charge carriers into the organic semiconductor as well as a brief discussion of proposed models for charge transport within the organic film (Ch. 2.5.2).

2.5.1 Carrier Injection

In order to achieve a current flow between the electrodes charge carriers have to be able to enter and leave the organic semiconductor into a metal contact. To achieve a close to ohmic contact we therefore need the metals work function to match the LUMO /

[1] For the automated evaluation of U_{Th} in ch. 4 the values from $I_{D,max}$ to $I_{D,max}/1.5$ from the mean forth and back measurements were used for fitting. For information on the script see ch. 6.1

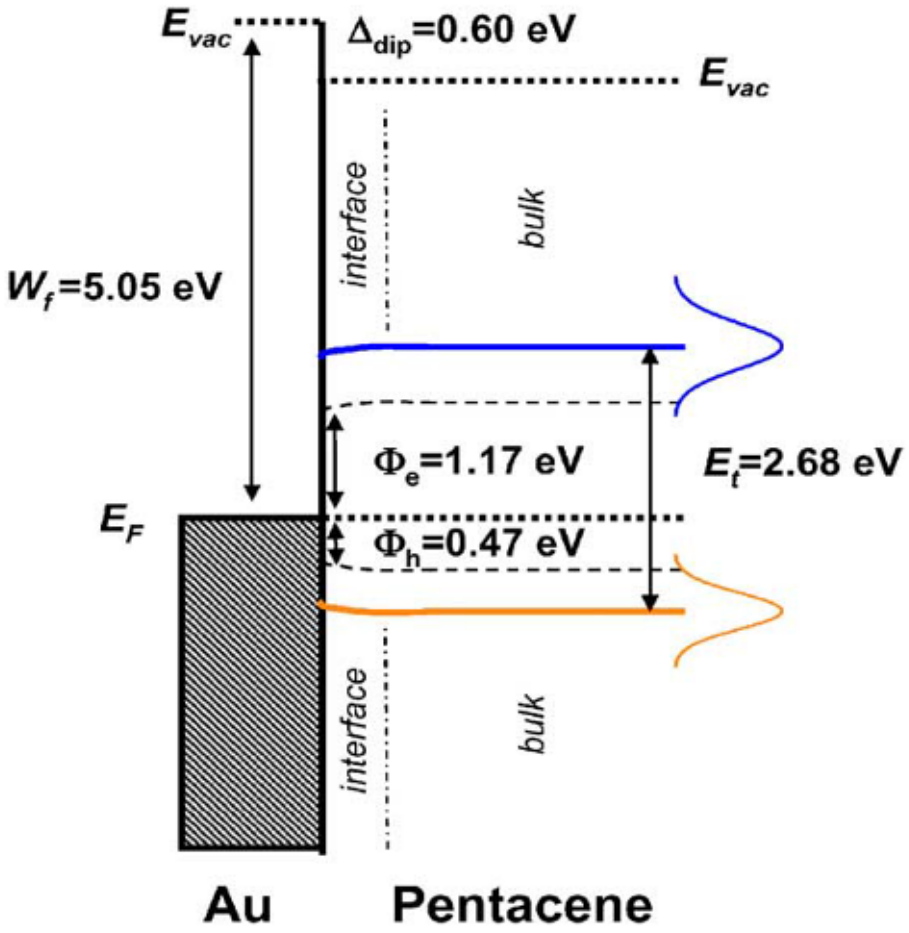

Figure 2.14: Lowering of vacuum level E_{vac} at the pentacene-gold interface due to polarization Δ_{dip}. Transport gap E_t and charge carrier injection barriers (ϕ_e, ϕ_h) deduced from UPS and IPES measurements [33].

HOMO level for a n/p type semiconductor, respectively, resulting in a Schottky contact. A common electrode material choice is gold with a work function of ϕ =5.1 eV [34]. This is a good match for pentacene with an ionization energy of $\chi = 4.9\,\text{eV}$ [35].

However, the gold-pentacene interface can massively change the energy relations of both materials. *Amy et al.* [33] investigated the combination and concluded a positive dipole layer of 0.6 eV and a reduction of the transport gap of 0.67 eV leading to an estimated hole injection barrier of 0.47 eV. This is still a large injection barrier compared to OLED technology where barriers greater then 0.25 eV lead to injection limited operation. The energy diagram of the pentacene-gold interface is depicted in figure 2.14.

Brondijk et al. [32] argue that image force lowering takes place at applied gate biases. This effect is even more pronounced for coplanar structures since the gate potential is screened at high accumulation states for their staggered counterparts. According to their thermionic emission model with image force lowering, injection barriers up to 1 eV will not result in injection limited transport for high gate biases. They also attribute *wavy* slopes in electrical output characteristics (Ch. 2.4.1) to injection limited transport. Although their model is based on thermionic emission they propose a thermally assisted charge hopping transport as a more likely description for the effective charge carrier injection transport. As a conclusion we regard coplanar bottom gate transistors as bulk limited devices with ohmic contact resistances with the premise of high gate biases. Extracted mobilities in the saturation regime will therefore approach bulk values.

2.5.2 Charge Transport

The charge transport within the polycrystalline film is still a controversial topic. Although the semiconducting properties of organic compounds are mostly attributed to the overlapping π-orbitals (Ch. 2.1) a delocalized band-like transport can only be observed for single crystals at very low temperatures. Structural and interface defects as well as grain boundaries lead to the localization of charges. Because of polarization there will be a lattice deformation (phonon cloud) accompanying the charge. These local deformations can be described in the quasi-particle model as *polarons* and their energy levels are residing in the energy gap between HOMO and LUMO.

To establish charge transport these charges need to *hop* from one localized state to another, which is typically called *hopping transport*. Because there is an activation energy necessary this form of transport needs to be thermally assisted. So in contrary to non-organic band-like transport, which is limited by electron-phonon interactions, polycrystalline organic films exhibit an increasing charge carrier mobility with increasing temperature [36]. Because of its high ordering polycrystalline films often exhibit anisotropies in the charge transport. This and other effects, such as the hysteresis of U-I curves which are attributed to shallow traps at the pentacene surface, are generally not accounted for in most models which have been suggested to describe the charge transport within the film best [5].

Multiple Trapping and Release Model

The multiple trapping and release model (MTR) was first used to describe charge transport for organic thin films which exhibit a well-ordered crystalline structure in the near range by *Horowitz et al.* [3]. It suggests that charge carriers can move in narrow localized bands within single crystallites. But at the grain boundaries and in structural defects the charge carriers get trapped in localized states. The dominant feature of the transport is given by the traps in the crystal and their thermal release barrier, which needs to be exceeded by charges in order to get to the transport level. Although this model can explain temperature and gate voltage dependency of the mobilities, it is still unable to explain the non-dependency of the mobility to temperatures for very low temperatures.

Grain Boundary Model

The grain boundary model was developed to account for the mentioned non-dependency of the mobility for low temperatures. Conceptually, a grain size far greater then the *Debye-length* would explain a band-like transport within the crystallites. The transfer of the charges through the grain boundaries is then becoming the bottle-neck for charge transport. In this case a non-uniform trap distribution is assumed because the traps are confined to the grain boundaries. Therefore charge transport is solely determined by the transport mechanism at the grain boundaries. For regimes $< 25\,\mathrm{K}$ tunneling dominates the transport. In the $25\,\mathrm{K} < 100\,\mathrm{K}$ regime activation barriers of $5\,\mathrm{meV}$ are estimated and thermally activated tunneling is assumed to determine the mobility. Finally for temperatures $100\,\mathrm{K} < 300\,\mathrm{K}$ with activation barriers of $0.1\,\mathrm{eV}$ thermionic emission is the dominating mechanism.

However this model is still neglecting temperature and gate-voltage dependencies on the potential barriers as well as the concentration of grain-boundary traps. If applicable, this model predicts a linear dependence of the mobility with the grain size [4].

3 Experimental Setup

3.1 Vacuum System

For the preparation of thin films and subsequent investigations, two vacuum chambers are at our disposable. The chambers are pictured in fig. 3.1. Both are equipped with a rotatable sample holder for aligning the sample with all flange-mounted instruments.

The main chamber (Fig. 3.1.a) is evacuated by a rotary vane pump and two turbo molecular pumps, achieving a minimum pressure of $p<1 \times 10^{-8}$ mbar. Evacuation over night results in a pressure of $\sim 1 \times 10^{-7}$ mbar, depending on the amount of time the setup was exposed to ambient environment. The sample may be cleaned with a sputter gun before a manually operated Knudsen cell is used to deposit materials on the sample. The setup is equipped with BNC adapters for electrical in-situ measurements on the transistor and Auger Electron Spectroscopy (AES) for surface analysis. Desorption can be achieved by the self-regulated sample-temperature control unit and evaluated with the quadrupole mass spectrometer.

The second chamber (Fig. 3.1.b) is not equipped with electrical adapters and is therefore only used to prepare films and samples for ex-situ AFM analysis. A rotary vane pump and a turbo molecular pump achieve slightly lower vacuums with $\sim 1 \times 10^{-7}$ mbar.

All installed instruments will be explained in more detail in the following. Additionally a detailed manual describing the operation of all instruments was generated during the work on the thesis[1].

[1] Manual present as a OneNote file on the AFM measurement PC at
C: | *Users* | *HollererM* | *Documents* | *OneNote Notebooks* | *Personal*

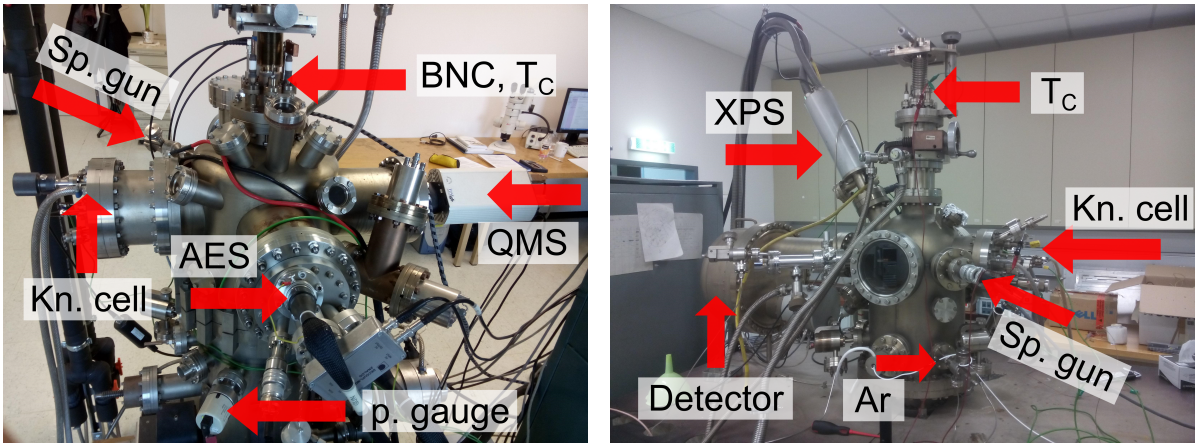

(a) (b)

Figure 3.1: Vacuum chambers used for preparation and investigation of thin films. The inscriptions show the installed analysis instruments with the following abbreviations: AES - Auger Electron Spectrometer, QMS - Quadrupole Mass Spectrometer, XPS - X-ray Photoelectron Spectrometer, BNC - BNC adapters, T_C Temperature control, Sp. gun - Sputter gun, Kn. cell - Knudsen cell, p. gauge - pressure gauge

3.1.1 Sample and sample holder

The silicon wafers consist of highly p doped silicon with a thermally grown oxide of 150 nm on top of it and are produced by SIEGERT WAFER GmbH[2]. They are cut into chips of 1 cm × 1 cm. The substrate is then further processed by our cooperation partners[3]. Oxygen plasma etching is performed before gold electrodes are evaporated onto the oxide via a shadow mask. This results in electrodes of 60 nm thickness which are separated by a channel of 25 μm.

Nickel wires with a diameter of 0.1 mm are then attached to the electrodes with off-the-shelf contact-silver solutions. The gate contact is attached to the highly p doped Si wafer, acting as an ohmic contact. The wires are then connected to the shielded UHV cables of the BNC adapters by spot welding.

The prepared sample is clamped to a steel plate with isolating ceramic washers. A *NiCr-Ni* thermocouple is welded to the steel plate to measure its temperature. The steel plate itself is mounted on 0.5 mm tantalum wires which run into the basic copper

[2]For more information on the substrates visit: *www.siegertwafer.com*
[3]*Materials Division, Joanneum Research Weiz*

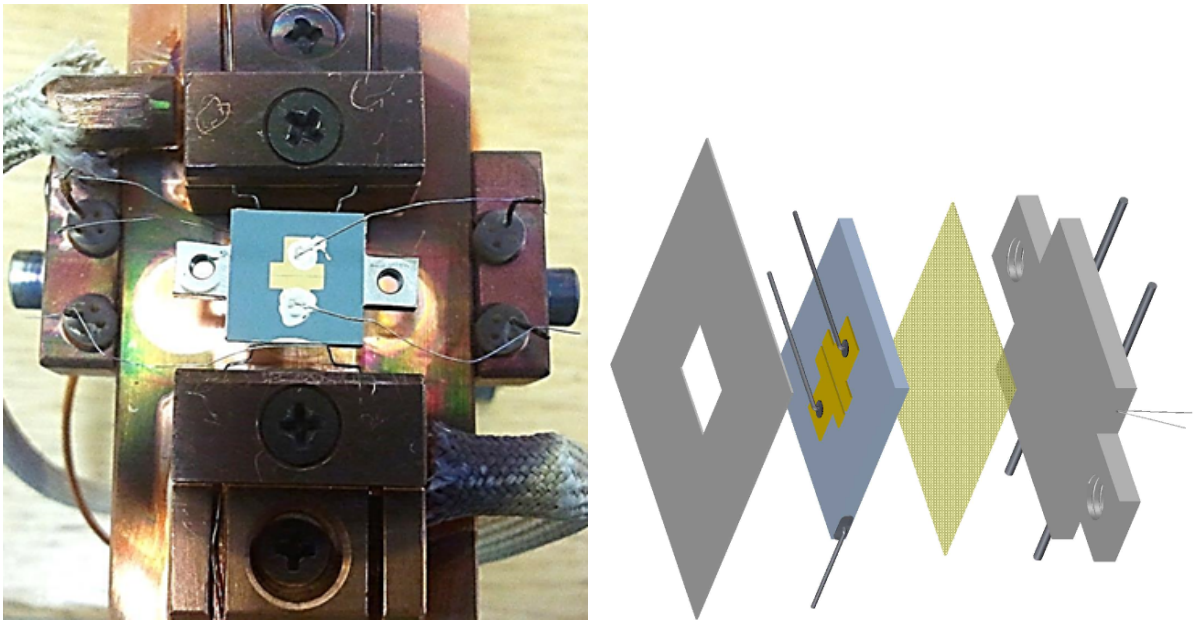

(a) (b)

Figure 3.2: Sample holder and draft of its arrangement. **(a.)** Picture of the sample holder copper block with the sample not yet screwed to the steel plate. The whole block is fastened to a rotatable hollow steel pole. **(b.)** From right to left: A steel plate is mounted on two heat resistance wires. A NiCr-Ni thermocouple is connected to the steel plate for temperature control. Between the sample and the steel plate a mica sheet is put for electrical isolation. Drain and source contacts are wired off the gold electrodes and the gate contact is attached to the highly p-doped Si substrate. In front of the transistor a shadow mask is limiting the area of pentacene deposition.

block. The whole block is fastened to a hollow rotatable steel pole which can be filled with liquid nitrogen for cooling. Within the whole rotatory sample holder an excavation is led to the copper block to ensure a good thermal contact for cooling. A *LabView* regulation loop is temperature controlling the steel plate by regulating the current flow through the tantalum wires. Stable temperatures from 150 K to 800 K can be achieved. In between the sample holder and the sample, a mica pane is mounted to electrically isolate the sample from the resistance-heating temperature system and allows electrical characterization when heating the sample. A draft of the sample holder - sample setup is pictured in fig. 3.2. In front of the sample a shadow mask is mounted that limits the area of evaporation. This minimizes the leaking current of the transistor.

3.1.2 Knudsen Cell

The Knudsen cell consists of a small metal cylinder that can be filled with materials for evaporation. A *NiCr-Ni* thermocouple is attached to the cylinder for temperature measurements and a heat resistance wire is spiraling around it and connected to a U/I source to manually adjust the heating current. Through a small hole in the cylinder the material can be evaporated directional onto the sample. A quartz crystal micro-balance (QCM) is mounted at the same distance and angle as the sample, when the sample holder is turned towards the Knudsen cell. Thus the amount of adsorbate can be accurately measured and controlled with sub-monolayer accuracy. A shutter unit can be manually set to allow evaporation only on the sample, the sample and the QCM, only the QCM and to shielding both at once. A picture of the evaporation unit is given in fig. 3.3.a.

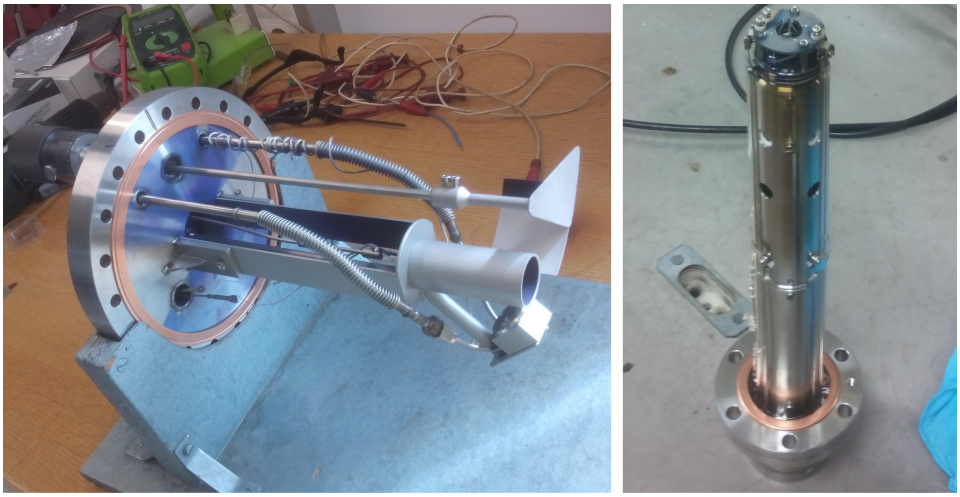

(a) (b)

Figure 3.3: Pictures of evaporation unit and QMS. **(a.)** Picture of the evaporation unit. The Knudsen cell is contained within the cylinder. The quartz crystal microbalance is installed at its bottom. If installed in the vacuum chamber, the sample could be placed in front of the cylinder. The shutter can then cover either the sample, the QCM, nothing or both. **(b.)** The ionization filament of the QMS and the quadrupole symmetry can be seen.

3.2 Experimental Methods

3.2.1 Quadrupole Mass Spectrometry - QMS

A *Balzers PRISMA 200* QMS is flange-mounted to the vacuum chamber. The uninstalled QMS is pictured in 3.3.b. It is capable of detecting and distinguishing between masses of up to 200 amu. Residual gas analysis and leakage investigations can be undertaken with the QMS. An important feature is the detection of the evaporation material. Since most organic compounds exceed the mass limit of 200 amu, characteristic cracking masses are usually measured instead. They can be either identified by multiplexing (measuring all masses after one another) or taken from literature data. For pentacene with 278 amu a dominant cracking mass of 125 amu was identified and used for further investigations.

The QMS evaluates the masses by ion counts per seconds. The sensitivity will therefore decrease with the distance between the desorption source and the QMS sensor. Because of the composition and versatility of our setup this distance is large for our system and thus exhibits a decreased sensitivity. To quantify the comparability of TDS spectra twelve samples with the same preparation (7 nm pentacene at 300 K) were put in front of the QMS. The films on the samples were thermally desorbed and the cracking mass of 125 amu was recorded. The absolute amount of counts was evaluated and compared and results in a standard deviation of 10%. This deviation is mostly attributed to poor adjustment when putting the sample in front of the QMS.

3.2.2 Thermal Desorption Spectroscopy - TDS

To conduct a TDS experiment the film has to be thermally desorbed off the sample and the amount of desorbent has to be monitored over time with the QMS. A *LabView* program controls the heating current and can execute temperature ramps. For our measurements temperature ramps with $\frac{\mathrm{d}T}{\mathrm{d}t} = 1\,\frac{\mathrm{K}}{\mathrm{s}}$ until a maximum temperature of $T = 650\,\mathrm{K}$ were conducted.

The counts per second are then plotted over the temperature. Because the thermocouple is attached to the steel plate and equilibrium is not achieved for this heating rate, a certain temperature lag for the sample is occurring. However, the temperature shift can be deduced by deposition of material onto the steel plate and successive desorption.

One can differentiate between three mechanisms of desorption. Zero-order desorption

appears when spectra for different coverages share the same rise of the peak and this signifies a non-dependence on the coverage. First-order desorption is present if the maxima for different coverages appear at the same temperature and signifies direct desorption of atoms or molecules. Second-order desorption is expressed in a shared fall of the curves for different coverages. It appears if two particles need to recombine before desorption is taking place. Spectra for the three kinds of desorption are pictured in fig. 3.4.

TDS is therefore a powerful method to characterize adsorbents and the mechanisms involved in de- and adsorption.

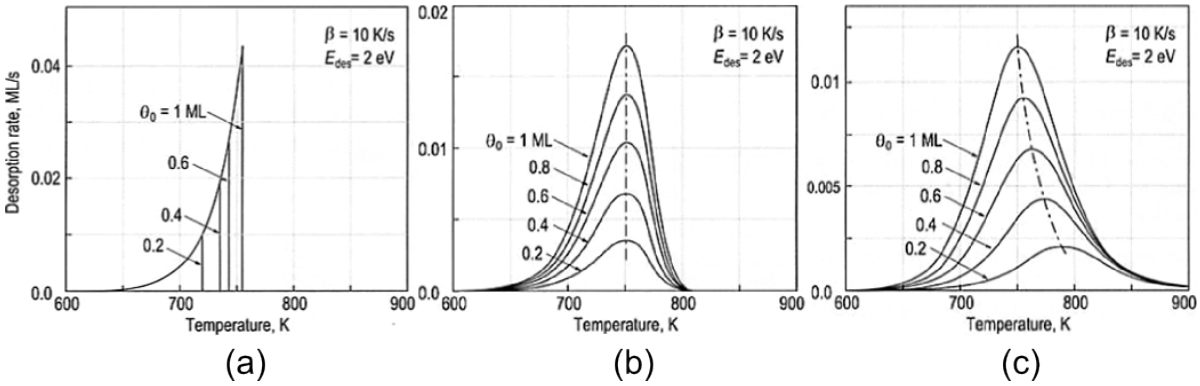

Figure 3.4: Examples for TDS spectra of different orders of desorption [37]. **(a.)** Zero-order desorption **(b.)** First-order desorption **(c.)** Second-order desorption

3.2.3 Sputter Cleaning

Traces of carbon, hydrogen and oxygen are not only present on the sample surface when being exposed to ambient environment, but also under ultra high vacuum conditions. To clean surfaces of environmental contaminants in-situ cleaning with a sputter gun can be performed. Atoms of an inert gas (mostly Argon) are ionized and then accelerated in an electric field towards the sample surface. Depending on the kinetic energy and the particle flux of the Argon ions, impurities and substrate atoms will be knocked out of the surface. Thus a clean surface can be achieved that will only slowly contaminate again with time, depending on the vacuum quality and the reactivity of the obtained surface.

A sputter gun is flange-mounted to the vacuum chamber. An Argon flask is connected to the gun in such a way that Argon ions may enter directly in front of the ionization

filament of the sputter gun. A precision valve allows the adjustment of a precise flow of Argon. To assure comparability in our experiments the valve was adjusted to result in a stable pressure of $\sim 8 \times 10^{-6}$ mbar. Before sputtering a device-operated *Degas* procedure is run to avoid ionization of filament contaminants. The sputter gun is then operated with an acceleration voltage of 0.8 kV.

In the case of thermally grown SiO_2, some Argon was found to penetrate the substrate and could only be removed by heating of the substrate to 800 K. The presence of non-metallic shadow masks (e.g. mica) when performing sputter experiments proofed to result in charging of the mica foil and the mask acting as an electric lens. This results in an inhomogeneous beam and edge effects of concentrated exposure.

3.2.4 Auger Electron Spectroscopy - AES

To characterize the elements present on a sample a surface-sensitive analysis is necessary. AES uses accelerated electrons to knock out inner core electrons of atoms. Electrons of higher levels will reoccupy the vacant state while emitting a photon of the element-characteristic energy-difference. This energy can be transferred to an outer core electron which will then leave the atom. When analyzing the energy of the emitted electrons the element composition of the surface can be deduced.

Because of the strong interaction of electrons, few will penetrate deep into the substrate with enough energy left to knock out inner core electrons. Additionally, *Auger* electrons created deep within the substrate are unlikely to leave the sample again. AES is therefore a highly surface sensitive instrument for material characterization.

A *STAIB Instruments, ESA 100* electron spectrometer is at our disposal. Auger spectroscopy measurements that were conducted within this work used the following instrument parameters:
Acceleration voltage: $U_A = 2\,\text{kV}$, Heating filament current: $i_F = 1.45\,\text{A}$, Emission current: $i_E = 1\,\mu\text{A}$, dwell time: $\tau = 50\,\text{ms}$, retracting time: $t = 1000\,\text{ms}$, energy increment: $\Delta E = 0.192\,\text{eV}$ and an energy range of: $E_{range} = 40\,\text{eV}$ to $600\,\text{eV}$.

3.3 Electrical Measurements

A *Keithley 2612 A* device with two source measurement units (SMUs) is used to measure the transistor curves. The wiring is arranged in a common-*low* circuitry, putting the

source contact on a common internal *low* level. The circuitry is sketched in fig. 2.9 and the functionality is explained in the corresponding chapter.

The instrument is controlled via an Ethernet connection by a *LabView* script using LabView's *VISA* for the interface communication. The *LabView* program is able to generate Keithley scripts, run them on the instrument and read the measurement data out of the instruments buffer storage. By either sweeping the voltage of *SMU A* (Source-Gate) and stepping the voltage of *SMU B* (Source-Drain) or in the opposite order, transfer and output characteristics can be recorded. Several conducted experiments advised us to use the empirically found maximum Gate-Drain potential of 60 V to avoid oxide breakthroughs. Because the threshold voltage was mostly found in the near negative regime, U_{GS} voltage sweeps of 10 V to −50 V were run for U_{DS} step functions within values of 0 V and −50 V. The Keithley script is designed to take measurements with a certain precision and is therefore self regulating the time for each measurement (AutoRange option). In between measurements of single current values the previously applied voltage is hold for 0.1 s.

It is an implication of the circuitry that occurring source/drain-gate leakage-currents will also appear partially as source-drain currents. This current is an artifact of the circuitry and its prefix depends on which electrode is conducting to the gate. To assure the functionality of the setup it was verified with a storage oscilloscope that no significant voltage spikes occur during the measurements. All consecutive measurements on a transistor are stored in a text-file generated by the LabView program.

A *Matlab* file was created to extract the data of the LabView file, enabling us to further process the data in *Matlab*. The source code for the program is given in ch. 6.1.1.

3.4 Atomic Force Microscopy - AFM

Atomic Force Microscopy (AFM) is a simple method of visualizing surfaces in the nm regime. The working principle of an AFM is depicted in fig. 3.5.a. Two *NanoSurf EasyScan 2* measurement heads (Fig. 3.5.b) with lateral and vertical scanning ranges of 10 μm and 70 μm and 2 μm and 10 μm, respectively, are at our disposal. As AFM measurements are very sensitive to vibrations the instrument is placed on an active vibration-damping socket, which is standing on a table, mounted to an outside wall of the building. Several modes of operation have been developed to enhance the performance of

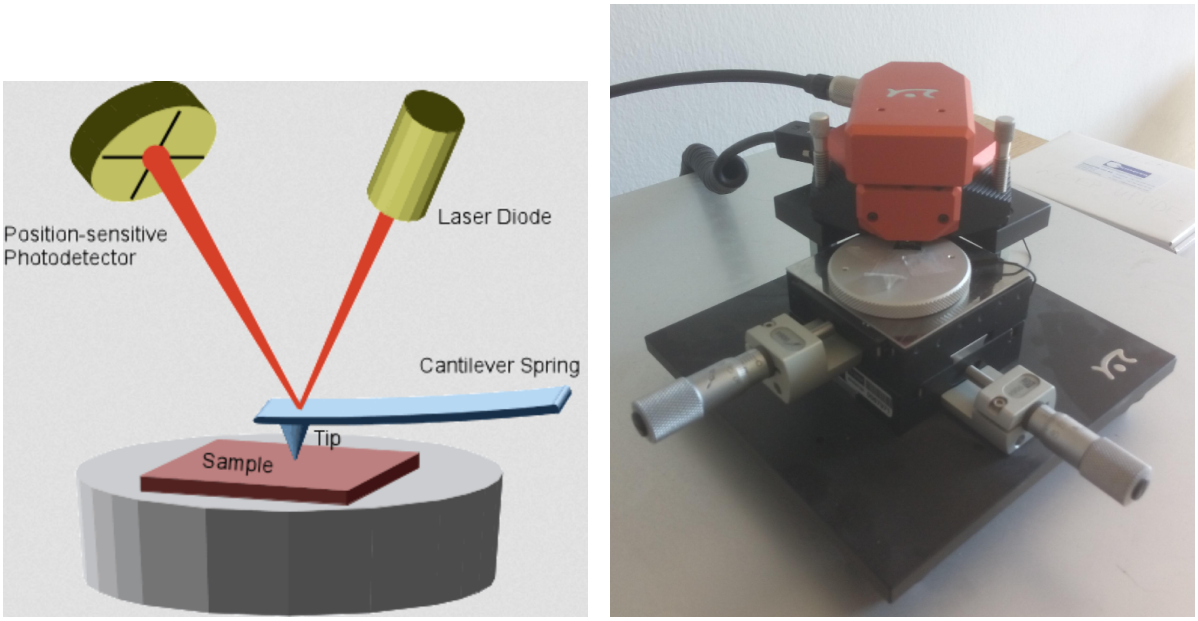

(a) (b)

Figure 3.5: Nanosurf EasyScan 2 - instrument and working principle of atomic force microscopy. **(a.)** A *cantilever* is drawn across a surface in a quadratic scanning pattern. A laser diode is projecting a beam on the cantilevers back. The reflection of the beam is analyzed in a four-quadrant photo-detector. Thus deviations of the cantilever can be precisely measured and calculated to a height profile of the investigated sample. A feed-back regulation loop evaluates the photo-diode information and keeps the cantilever on a relative height above the surface defined by the *Setpoint*. **(b.)** The 10 μm measurement head with installed video microscope, mounted on the instrument holder, which is set on an active vibration-damping socket. An x-y microstage allows sensitive repositioning of the sample with respect to the AFM.

AFM measurements. In the classical contact mode the tip is dragged along a surface with a contact pressure defined by the setpoint which is measured as the vertical deflection of the laser (bending of the cantilever). Although this mode achieves the best height resolution, big lateral shear forces are applied to the surface which can cause deformation of weakly bound surface materials such as organic thin films.

Dynamic Force Mode

To avoid the applied shear forces of the contact mode, the cantilever can be excited to sinusoidal oscillations when scanning the surface (*Dynamic Force Mode*). The feedback controller is then regulating the contact pressure by the amplitude of the oscillation. Because of its good results this method advanced to be the standard imaging mode for OFET samples. A *PPP-NCLR*[4] cantilever with a tip radius of <10 nm is used.

When run in the dynamic force mode three main channels of information can be extracted from the AFM, which are pictured in color-scale images of its dimension. The first channel states the vertical corrections of the feedback controller, keeping the cantilever on the predefined setpoint of its *amplitude*. The color-scale image yields good contrast for edge effects but neglects relative height differences of flat surfaces.

Integration of the noise-corrected *amplitude* channel yields the actual height information or *topography* channel. Because of the integration of the measured values this channel is most susceptible to imaging artifacts. The result resembles the actual surface of the sample although its representation can only poorly resolve sharp edges of little height difference. Since it yields the actual height information, 3D images can be constructed out of the topography channel information.

The third channel recorded by this mode is the *phase contrast*. It states the phase-difference between the excitation signal of the controller and the actual oscillation of the cantilever. This channel is hardest to interpret, since the phase shift depends on various properties such as adhesion, friction, viscosity, and energy dissipation. Because of the latter it is very sensitive to abrupt edges and can be used for observing very small steps. Since it is dependent on many material properties it is also capable of detecting material contrast, but, as multiple properties are contributing to the phase shift, caution has to be taken when interpreting the results.

Measurement Parameters and Artifacts

To obtain the most information for an image various measurement parameters can be set to match the surfaces properties. In the following a short explanation of the adjustable parameters for the *dynamic force mode* is given. The **free vibration amplitude** states the voltage amplitude used to excite the cantilever and corresponds to an oscillation

[4] Point Probe Plus - NonContact Long Reflective cantilever, for more information visit *www.nanosensors.com*

displacement of the cantilever in air. The **setpoint** regulates the vertical deflection and hence the contact pressure of the cantilever in such a way that the amplitude is decreasing to the **setpoint** percentage of the free vibration amplitude. A standard PID regulation (Proportional, Integral, Differential) is accessible to control the feedback loop for the vertical deflection. Additionally **points / line** define the resolution and **time / line** sets the time taken for the measurement.

A measured AFM image may differ from the actual surface to a point where it is represented by measurement artifacts rather then the actual height profile. This plays an important role to novice AFM users since the source of imaging errors is completely different to conventional light or electron microscopy. To better understand and to avoid this the artifacts need to be well understood in order not to misinterpret AFM results.

AFM artifacts are mostly subdivided to the sources causing the artifacts. The main sources are *tip artifacts*, caused by the shape of the tip which is subject to contamination, modification, cracking and splitting, *scanner artifacts* such as edge overshoot or piezo creep and various other artifacts caused by the *laser*, the *feedback loop*, *vibrations* and *thermal drifts* [38, 39]. A detailed discussion of AFM artifacts would go beyond the scope of this work. Artifacts will be present in all AFM images which can only be partly corrected by post-processing of the images. Hence, special care has to be taken when evaluating and interpreting images.

Especially for the work presented in this thesis, loose particles and *debris* proofed to contaminate the cantilever rather quickly. The presence of such contaminants is increasing in frequency with the amount of adsorbent, especially when the substrate exhibits material or morphological changes within the measurement range. Thus, it proofed to be difficult to obtain artifact-free images of transition areas or samples with thick films.

3.4.1 Gwyddion

Gwyddion is an open-source software project, primarily intended for visualization and analysis of *scanning probe microscopy (SPM)* data, which is the generic group also including AFM imaging. It is capable of reading all common data formats including the *NanoSurf* internal file format *.nid*. Because of the multitude of data processing options this program advanced to be one of the most used programs for processing AFM images.

All pictured images in this thesis were post-processed with Gwyddion[5].

[5]For more information visit: *http://gwyddion.net/*

4 Results and Discussion

4.1 Surface Characterization

4.1.1 Surface Roughness

Before discussing the growth of the semiconductor and the electrical properties of our OFETs, a short investigation of the samples, as prepared by *Joanneum Research Weiz* (Ch. 3.1.1), is done. The samples are dry-cleaned and then built into the vacuum chamber. Investigation of the carbon contamination levels with Auger spectroscopy (Ch. 3.2.4) on SiO_2 yield a high carbon level with little substrate signal (Fig. 4.1). After deposition of pentacene only carbon is to be seen. If the film is then thermally desorbed and sputter-cleaned for 10 minutes (Ch. 3.2.3) no carbon remains at the surface. Deposition and re-desorption (TDS - cycle) results in a carbon contamination which is growing with each consecutive TDS cycle. Measurements on the gold surface yield the same results with respect to the carbon contamination.

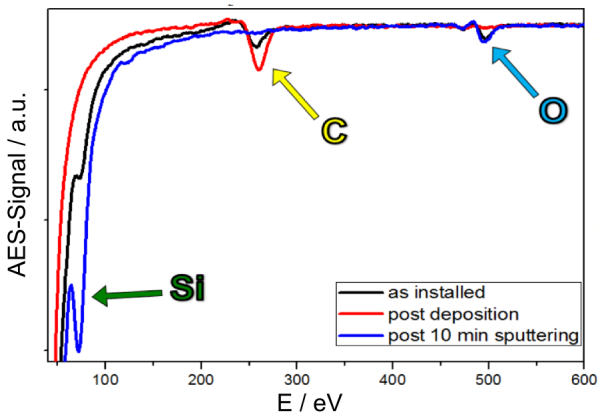

Figure 4.1: Development of carbon contamination on SiO_2, before, and after deposition, as well as after desorption with consecutive sputter-cleaning (Ch. 3.2.3).

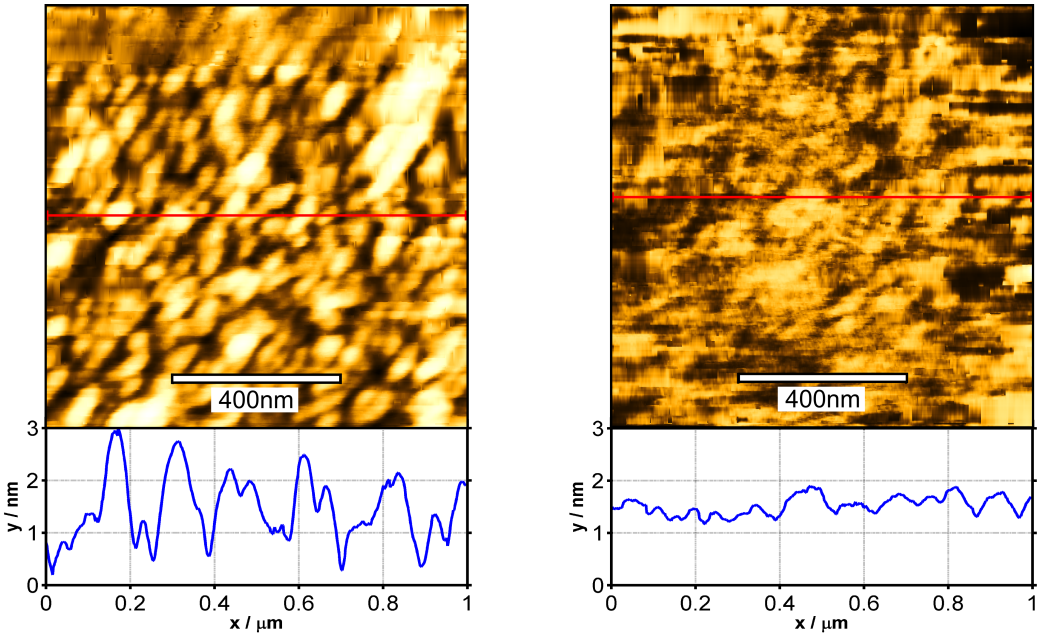

(a) $R_a = 0.50\,\text{nm}$

(b) $R_a = 0.16\,\text{nm}$

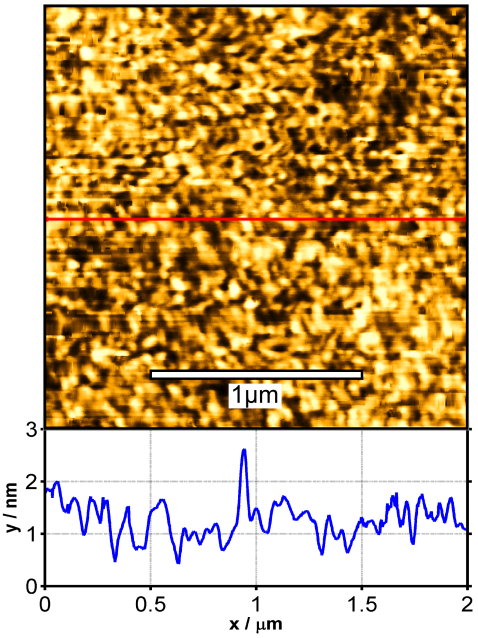

(c) $R_a = 0.31\,\text{nm}$

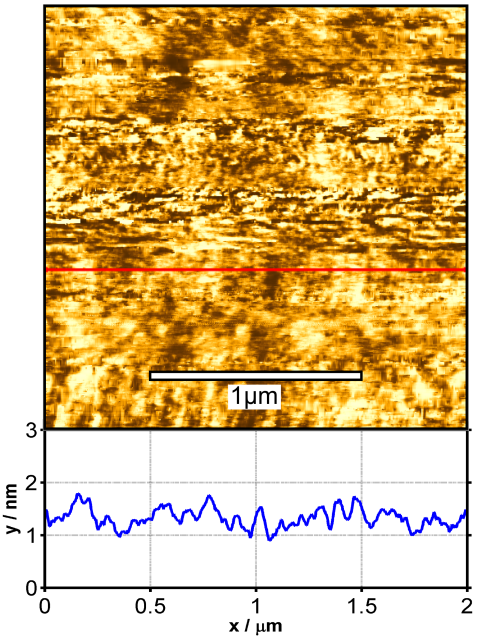

(d) $R_a = 0.20\,\text{nm}$

Figure 4.2: AFM topography images with corresponding roughness values. **(a.)** Gold, untreated. **(b.)** SiO_2, untreated. **(c.)** Gold, 30' sputter cleaned. **(d.)** SiO_2, 30' sputtered cleaned.

AFM measurements on *as received* samples and on heavily sputter-cleaned samples were carried out and their roughness values were evaluated (Fig. 4.2). Gold exhibits an overall greater roughness then SiO_2 which is decreasing when sputter-cleaned. SiO_2 has a roughness close to the AFMs resolution limit and is therefore difficult to image. The sputtered SiO_2 surface image thus contains measurement artifacts which artificially increase the roughness value (Fig. 4.2.d). It is therefore hard to verify a surface roughening due to sputter-cleaning which is, if present at all, very small. Another indication for little influence by sputter-cleaning on SiO_2 is observed when performing intense long-time sputtering, yielding that the gold films height is decreasing with respect to the SiO_2 surface. Thus the gold film is disappearing while the SiO_2 is not, or is disappearing only very slowly. Furthermore, these measurements are taken ex-situ and are therefore subject to external contamination.

4.1.2 Electrode-Dielectric Transition

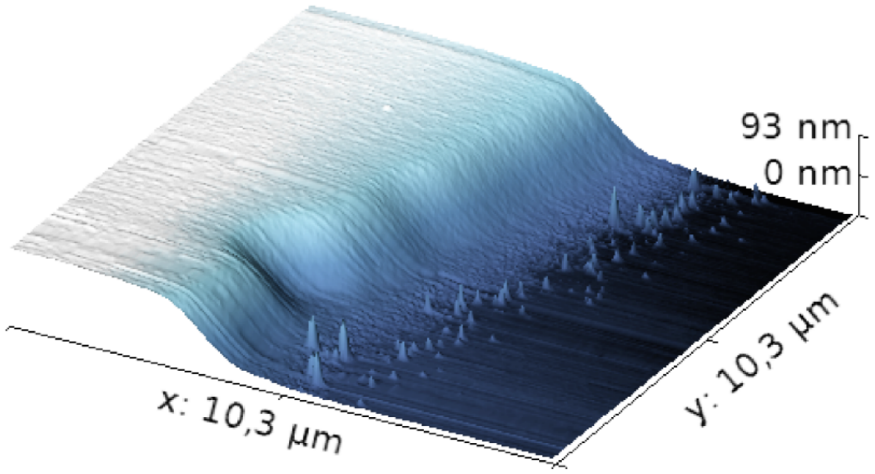

Figure 4.3: AFM 3D topography image of the gold-SiO_2 transition area. The 60 nm gold film descends over a distance of 2000 nm. The remote islands exhibit heights of 10 nm to 50 nm and diameters of 100 nm to 400 nm. The z-axis of the image is highly exaggerated.

The connection of a semiconductor-film with the electrodes is crucial for OFET performances. The development of a junction is strongly dependent on the substrate morphology, which is therefore investigated. AFM measurements discovered gold islands

growing inside the channel with ∼1 μm to ∼2 μm distance to the electrodes (Fig. 4.3). These islands are found to be a side-effect of the manufacturing process. The gold is evaporated onto the substrate via a shadow-mask containing a shadow-wire to create the channel. It is our understanding that gold atoms are able to diffuse beneath the shadow wire and clusterize beneath it. These islands are observed on all samples in a great variation of size (heights of 10 nm to 50 nm and diameters of 100 nm to 400 nm) and frequency of occurrence. This might be caused by the sample-specific wire-substrate contact and its clamping tension.

The descend of the gold electrodes exhibits a shallow slope of approximately 3°. The islands lead to an improper connection of the pentacene film which is discussed in ch. 4.4. Lithography manufactured samples would avoid this problem but are reported to contain photo-film residues which might also hamper the semiconductor-electrode connection [40].

Ultrasonic Cleaning

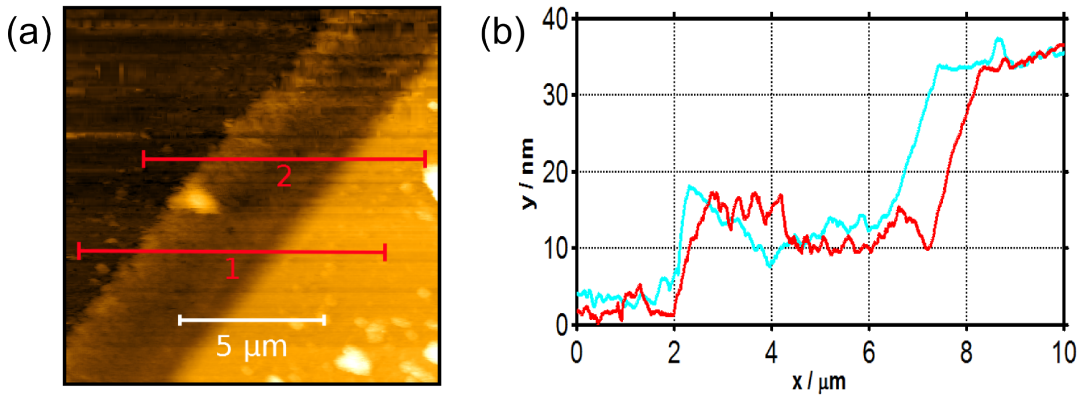

Figure 4.4: ((**a.**) AFM topography image of an US cleaned sample. SiO_2 in top left corner, gold electrode in bottom right corner. A terrace like gold film develops out of the former islands in front of the electrode bulk. **(b.)** Cross-section 1 (red) and 2 (blue) suggest a preceding gold-film-height of 10 nm.

An interesting effect was observed when cleaning the sample in an ultra-sonic (US) bath. The sample was put in a vial containing isopropanol and US cleaned for ten minutes. Although the AFM images exhibit many contaminating particles, the islands seem to vanish and combine to an approximately 10 nm high terrace in front of both

electrodes (Fig. 4.4). Because of the weak bonding of gold on SiO_2 this procedure may lead to loosening of whole electrodes. But, if optimized, this treatment could enhance the performance of samples produced via shadow-masking.

4.2 Quantifying Pentacene Deposition

A major issue when trying to relate morphological properties with electrical transistor characteristics is the evaluation of the amount of semiconductor which is actually deposited on the substrate. *Guo et al.* [41] suggest a temperature dependent sticking coefficient (Ch. 2.2.1) which is also strongly dependent on the substrate contamination and hence the substrate treatment. It is therefore important to reliably judge the amount of the deposited semiconductor. To relate the amount of adsorbed semiconductor material with our quartz crystal micro-balance (QCM), in-situ TDS measurements (Ch. 3.2.2) and ex-situ AFM measurements (Ch. 3.4) are at our disposal. Using the reshaped *Sauerbrey equation* [42]:

$$d = -\frac{\sqrt{\mu_{Qu}\rho_{Qu}}}{\rho_{ads}}\frac{\Delta f}{f^2} \tag{4.1}$$

μ_{Qu}... Shear modulus of quartz crystal, $2.947 \times 10^{11}\,\mathrm{g/cm\,s}$

ρ_{Qu}... Density of quartz crystal, $2.643\,\mathrm{g/cm^3}$

ρ_{ads}... Density of adsorbent, $1.33\,\mathrm{g/cm^3}$ for pentacene

f... Eigenfrequency of quartz crystal, 5.94 MHz

Δf... Frequency shift of QMC with adsorbent

d... Adsorbent film thickness

we find a nominal conversion factor of 0.94 Å/Hz assuming a perfect thin-film phase crystallite, a sticking coefficient of unity, and an identical amount of deposition on the QCM and the specimen.

4.2.1 AFM Thickness Evaluation

In the following, the determination of an empiric conversion factor for the frequency change of the QCM to a thickness value is discussed for a specimen with a nominal adsorption of 30 Hz deposited at $T = 300\,\mathrm{K}$. It is known from previous measurements that 30 Hz is well above a ML. Therefore the islands seen in fig. 4.5 correspond to the

nucleation of the second layer. We use two evaluation methods for the quantification of the amount of adsorbed pentacene on the SiO_2 surface.

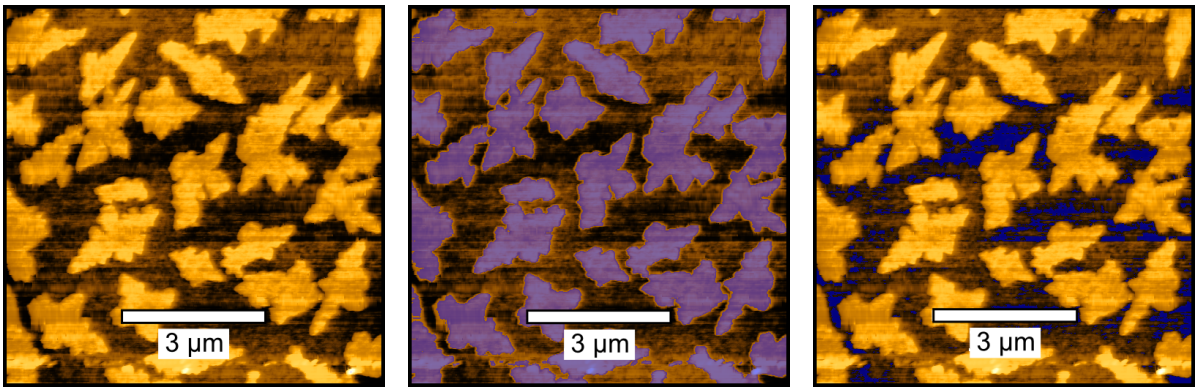

(a) (b) (c)

Figure 4.5: Topography image of a specimen with a 30 Hz pentacene layer deposited at 300 K on SiO_2. **(a.)** Original image. **(b.)** Islands marked by threshold. **(c.)** Mean Background marked by threshold.

Quantification by Calculation of Ad-layer Surface

In this attempt an AFM image of a pentacene layer on a SiO_2 surface is analyzed (Fig: 4.5.a). The image is processed to correct imaging artifacts and to achieve a flat background. Because of the tip radius of the cantilever coverages will be overestimated. Evaluation of the marked area in fig. 4.5.b results in a relative coverage of 44 %. Together with the full ML beneath this amounts to a deposition of 0.048 ML/Hz. Calculating with the nominal inter-planar spacing of the pentacene thin film phase of $d_{001} = 15.4$ Å/ML this is a deposition of 0.74 Å/Hz.

Quantification by Volume Calculation

In this method the volume of the film is calculated by integrating over the AFM height information with respect to the lowest data point. It is therefore crucial to achieve a precise leveling of the recorded image. Obvious artifacts, present as steep almost singular holes or spikes, are manually interpolated. Additionally, the mean corrugation-height of the layer below the topmost island-like structure is determined for the analyzed area of $A_{image} = 73.96\,\mu m^2$ by a threshold in fig. 4.5.c as $h_{mean} = 0.3$ nm. If calculating the volume with *Gwyddion* (Ch. 3.4.1) this results in $V = 0.063\,\mu m^3$. If the mean background

(e.g. top of the layer below the island structures) is subtracted ($V_{BG} = h_{mean} \cdot A_{image}$) this results in a layer volume of $V_{layer} = 0.041\,\mu\text{m}^3$ which amounts, together with a nominal wetting layer (the layer below the islands), to a volume of $V = 0.155\,\mu\text{m}^3$ or a thickness of $d = 2.09\,\text{nm}$. Considering the nominal deposition of 30 Hz for this sample this results in a conversion factor of 0.045 ML/Hz or 0.70 Å/Hz.

Both methods conclude in a similar conversion factor of $c_{QCM} = \sim 0.7\,\text{Å/Hz}$. This value is an approximation based on the accuracy of the AFM measurements and does not take into account the higher inter-planar spacing d_{001} of the first layer (underestimation) nor the tip-feature enlargement (overestimation). A non-dependence of the sticking coefficient with the coverage is assumed. Nevertheless, it is a conclusive conversion factor, enabling us to estimate film thicknesses and, as will be demonstrated in ch. 4.2.3, estimating the number of fully intact monolayers below the pyramidal island structure. Whereas the first method is more reliable, since it is not that sensitive to AFM artifacts, the latter allows for quick analysis and estimations. The good agreement of both methods approves for their application. The big deviation from the theoretically calculated value is probably due to slightly different distances between QCM and sample to the Knudsen cell and probable angular position because of poor alignment.

4.2.2 Thickness Evaluation using TDS

The preceding chapters discussed the film thickness to QCM frequency shift conversion factor for a film prepared at 300 K with several presumptions. To further improve the understanding of the film deposition and to check for temperature dependence, TDS series are evaluated. TDS have been recorded for films of 1.4 ML (30 Hz), 6.8 ML (150 Hz) and 22.7 ML (500 Hz) prepared at temperatures of 200 K, 300 K and 350 K each (Fig. 4.6). All films were deposited and re-evaporated from one and the same specimen. All measurements result in TDS peaks with a common rise. This corresponds to zero-order desorption (Ch. 3.2.2) and signifies a non-coverage dependent desorption and therefore similar binding energies for the wetting layer and the successive layers.

The normalized TDS areas are compiled in tab. 4.1. The relative average amount of pentacene of the 300 K and 350 K films compared to the 200 K film is 79 % and 85 % respectively. A smaller sticking coefficient for higher temperatures is expected as a greater temperature increases the possibility of desorption. The integrals over TDS spectra of films with different thicknesses exhibit a generally good agreement although

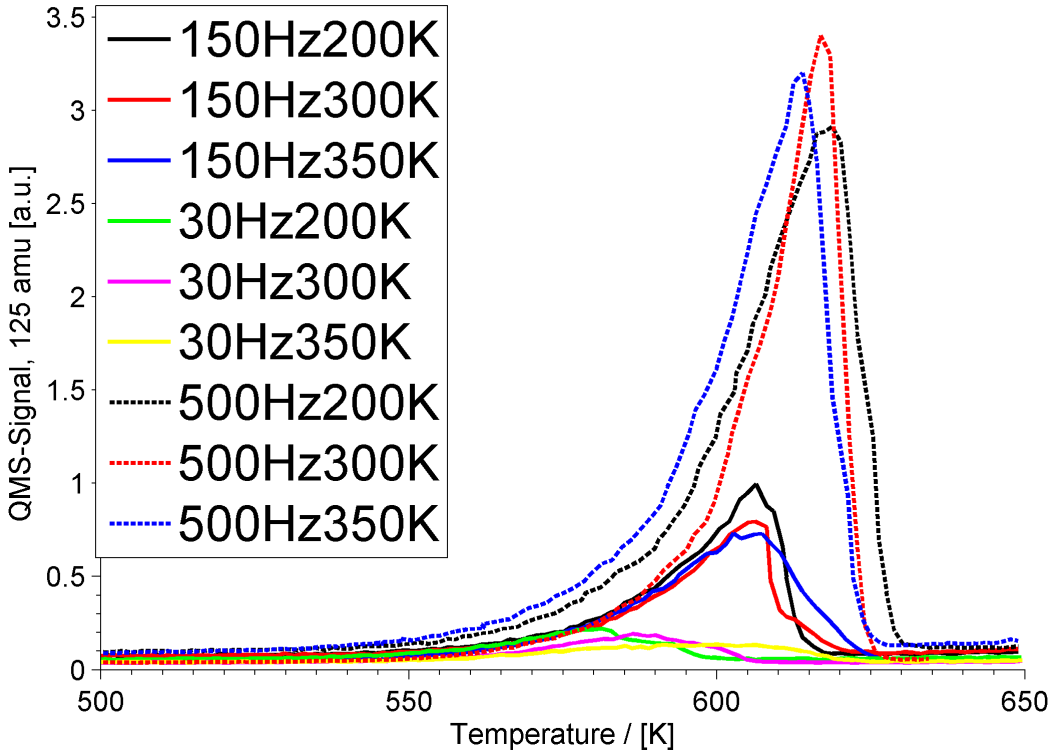

Figure 4.6: TDS spectra of pentacene films of different thicknesses and prepared at different temperatures. Spectra have been background corrected. Values for the integrated peaks are given in tab. 4.1.

the TDS signal is subject to many sources of errors (Ch. 3.2.2 - Standard deviation of 10 %). The 200 K film exhibits overall greater integrals, suggesting a slightly increased sticking coefficient for this temperature. The observed better sticking coefficient for the 350 K then the 300 K film appears unusual but is within the error range of the TDS evaluation and we suggest that no further decrease of the sticking coefficient from 300 K to 350 K takes place. Comparison of the lowest to the highest coverage hints to an improved sticking coefficient of the first ML, but the low precision of the TDS, especially for thin films, questions that conclusion. All measurements have been taken within an hour of deposition so that long-term desorption would not appear in the data. Both the 200 K and 350 K films were heated/cooled to 300 K before TDS which implies time for surface reconstruction whereas the 300 K film was deposited, electrically characterized and desorbed directly after.

With this evaluation it is shown that the previously derived conversion factor of

Table 4.1: Integration over TDS peaks of fig. 4.6. Spectra have been background corrected and normalized with respect to the greatest integral.

	200 K	300K	350 K
1.4 ML (30 Hz)	0.09	0.07	0.06
6.8 ML (150 Hz)	0.31	0.24	0.29
22.7 ML (500 Hz)	1.00	0.82	0.94

$c_{QCM} = 0.7\,\text{Å/Hz}$ can be approximately used for films prepared within a substrate-temperature range of 200 K to 350 K.

4.2.3 Layer Estimation for Thick Films

With the conversion factor of 0.7 Å/Hz derived in ch. 4.2 an estimation of the film growth of thicker films can be obtained. A specimen with a nominal thickness of $d = 10.5\,\text{nm}$ or 6.8 ML, corresponding to a deposition of 150 Hz, is investigated. In fig. 4.7 the planes of each step are marked by a threshold. Tab. 4.2 states the percentage of each layer facing the vacuum side as well as the absolute area coverage of each layer.

Table 4.2: Evaluation of the coverage of a specimen prepared with 10.5 nm at 300 K. The first row states the area percentage of the vacuum-facing sections of the layers, starting with the lowest, fully filled layer (Fig. 4.7)a-h. The second row states the absolute coverage of each layer.

	Layer 1	Layer 2	Layer 3	Layer 4	Layer 5	Layer 6	Layer 7	Layer 8
Surface / %	0.4	5.8	13.8	16.4	24.0	24.0	13.6	2
Area / %	100.0	99.6	93.8	80.0	63.6	39.6	15.6	2

It is notable that the lowest visible layer is almost fully closed whereas, starting with layer two, a significant roughening sets in. Adding up the absolute area of each layer (Layer 2-8 in tab. 4.2), for the investigated area of $A = 25\,\mu\text{m}^2$, times the step height $d_{001} = 15.4\,\text{Å}$ results in a volume of the investigated area of $V_{sur} = 0.153\,\mu\text{m}^3$. The nominal coverage is given by $V_{nom} = A \cdot \Delta f \cdot c_{QCM} = 0.263\,\mu\text{m}^3$, with the area A, the QCM frequency shift Δf and the empirical conversion factor $c_{QCM} = 0.7\,\text{Å/Hz}$. The difference in volume should amount to a number of fully closed layers below the visible

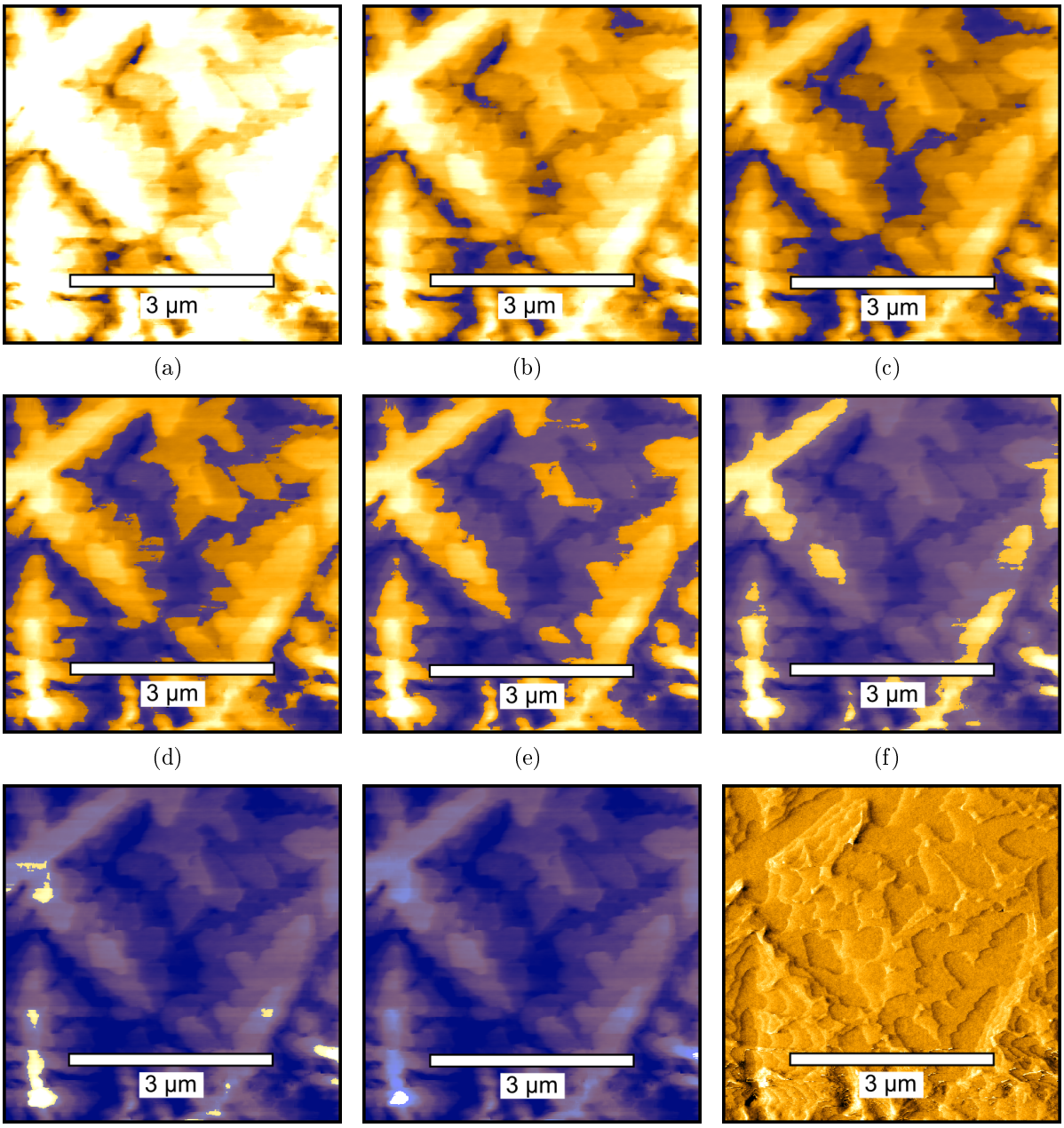

Figure 4.7: AFM topography images of a specimen prepared with 10.5 nm (150 Hz) at 300 K. **(a.-h.)** show the threshold-marked single-layers for the evaluation of the absolute pentacene deposition (Tab.4.2). **(i.)** shows the amplitude channel of the image for better visualization of the terrace growth.

surface: $\frac{V_{nom}-V_{sur}}{d_{001}} = 2.7\,\text{ML}$.

Applying the volume method (Ch. 4.2.1) results in $\frac{V_{nom}-V_{layer}}{d_{001}} = 2.9\,\text{ML}$. Both methods suggest that approximately three fully closed ML are developed beneath the surface and the fourth already covers 99.6 % of the surface. Possible micro valleys with steep and small cracks between grains cannot be resolved with AFM imaging. The uniformity of the films is strongly dependent on the growth process and therefore very temperature dependent.

In this investigation it has been shown that for films in this thickness and temperature regime already four, well connected, layers are established on top of the substrate.

4.3 Optical Measurements

To expand the microscopical imaging into larger scales, optical microscopy was performed. Pictures of the OFET channel with a pentacene film of 6.8 ML (150 Hz) prepared at $T = 200\,\text{K}$, 300 K and 350 K were taken and are depicted in fig. 4.8.

The 200 K film exhibits no visible change in film growth and only a change of reflectivity is observed at the gold-SiO_2 substrate transition. On the 350 K film the expected needle-like islands are growing on the gold surface, but a depletion of pentacene islands can be observed as far as $\sim 10\,\mu\text{m}$ into the gold electrode. Since the islands on the gold exhibit no particular variation in growth close to the depletion area, the missing pentacene needs to diffuse towards the channel. The transition area is therefore acting as a pentacene sink, accumulating great amounts of material. The diffusion length of pentacene on gold is thus in the magnitude of the depletion width. We suggest that this further hinders the development of a successful junction of the thin film phase with the gold electrodes. This effect is only weakly pronounced for the 300 K film, where the needle like growth persists until the edge, but the form and height of the islands changes within the last μm. This is consistent with AFM images.

The form and distribution of the islands are strongly dependent on the sample preparation and whether sputter-cleaning was performed directly before the measurements. The diffusion length of the pentacene monomers is therefore not only dependent on the temperature but also on the contamination of the surface. Fig. 4.8.d exhibits a change in the growth behavior on far greater scales around an external particle on gold substrate. The film was prepared with a coverage of 22.7 ML.

The randomly distributed particles emphasized with green circles in fig. 4.8.a-c are

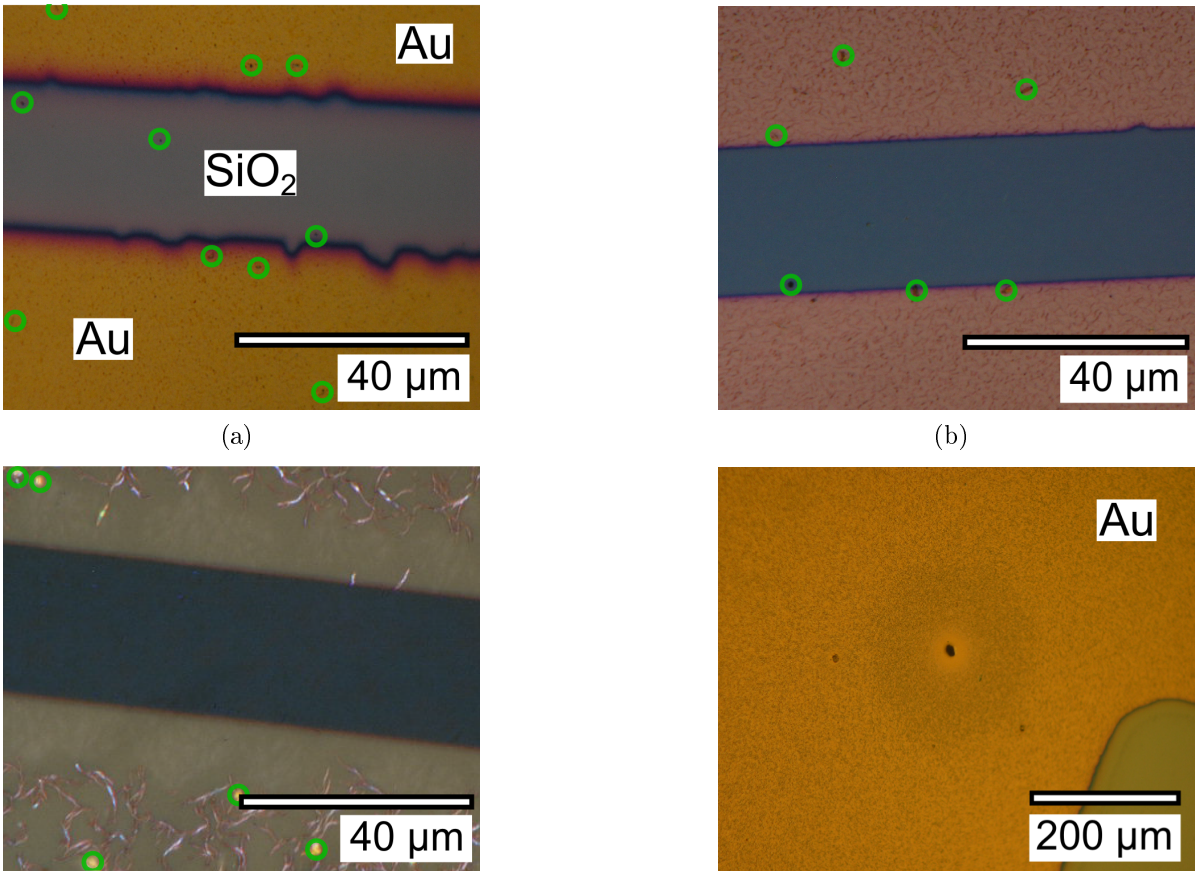

Figure 4.8: Optical images of pentacene OFETs. The green circles emphasize TDS residues. **(a.-c.)** Optical microscopy images of the OFET channel prepared at $T = 200\,\mathrm{K}$, $300\,\mathrm{K}$ and $350\,\mathrm{K}$ with $22.7\,\mathrm{ML}$, $6.8\,\mathrm{ML}$ and $6.8\,\mathrm{ML}$, respectively. **(d.)** Image of a $22.7\,\mathrm{ML}$ film prepared at $T = 350\,\mathrm{K}$. Influence on the growth behavior around an external particle on gold substrate within a radius of about $100\,\mu\mathrm{m}$.

always present after deposition of pentacene and can only be removed by sputtering. Due to the large distance between those particles, pentacene growth effects can be excluded as their origin. It is therefore probable that these particles are clusters or residues forming after desorption.

4.4 Pentacene Film-Morphology Correlation with Electrical Properties

The main object of this work was to investigate the growth behavior of pentacene in the gold-dielectric contact area and its dependence on temperature. For this reason samples of different coverages prepared at different temperatures were produced for AFM investigations. Temperatures of $T = 200\,\mathrm{K}$, $300\,\mathrm{K}$ and $350\,\mathrm{K}$ were chosen, resembling a very low temperature where little surface diffusion is assumed, room temperature and a temperature little above the often stated best temperature $T = \sim 330\,\mathrm{K}$ for high performance OFETs [12]. To investigate the film growth at this temperatures coverages of 1.4 ML (30 Hz), 6.8 ML (150 Hz) and 22.7 ML (500 Hz) were established for all of the stated temperatures. To attribute OFET performances to the pentacene film growth, according electrical measurements were performed. All films for the stated parameters exhibit transistor properties, which implies that at least one ML of standing pentacene molecules has to be present and is, at least partly, connected to the electrodes. The best transistor manufactured resulted in a mobility of $0.13\,\frac{\mathrm{cm}^2}{\mathrm{Vs}}$, comparable to coplanar bottom-gate transistors in literature [43].

For the following investigations several ad- and desorption cycles were carried out to establish a well defined carbon level on the substrates. Corresponding electrical measurements were also conducted after a saturated carbon contamination was achieved. The samples morphology, measured ex-situ, shall therefore resemble the in-situ morphology when the electrical measurements were conducted.

The number of intact wetting layers calculated for the obtained AFM images with method 4.2.1 is stated as $\mathrm{ML}_{\mathrm{Vol}}$ and values estimated by the cross-sections are given as $\mathrm{ML}_{\mathrm{CS}}$. The cross-sections given with the AFM images are normalized to the nominal film thickness.

4.4.1 Electrical Properties: Function of Temperature and Coverage

A well working sample was chosen to execute electrical measurements. Therefore we can assume the same preconditions for all produced transistors and assure a comparability between the devices. For substrate temperatures of 200 K, 300 K and 350 K the sample is successively evaporated with pentacene. After the deposition of a certain amount the

shutter is closed, a transfer characteristic is measured at the same temperature for which deposition is performed, and the shutter is reopened again. The saturation mobilities are evaluated according to ch. 2.4. The temperature dependency of the mobility is not considered in the shown figures. Before the formation of a conducting channel the definition of a charge carrier mobility is effectively invalid.

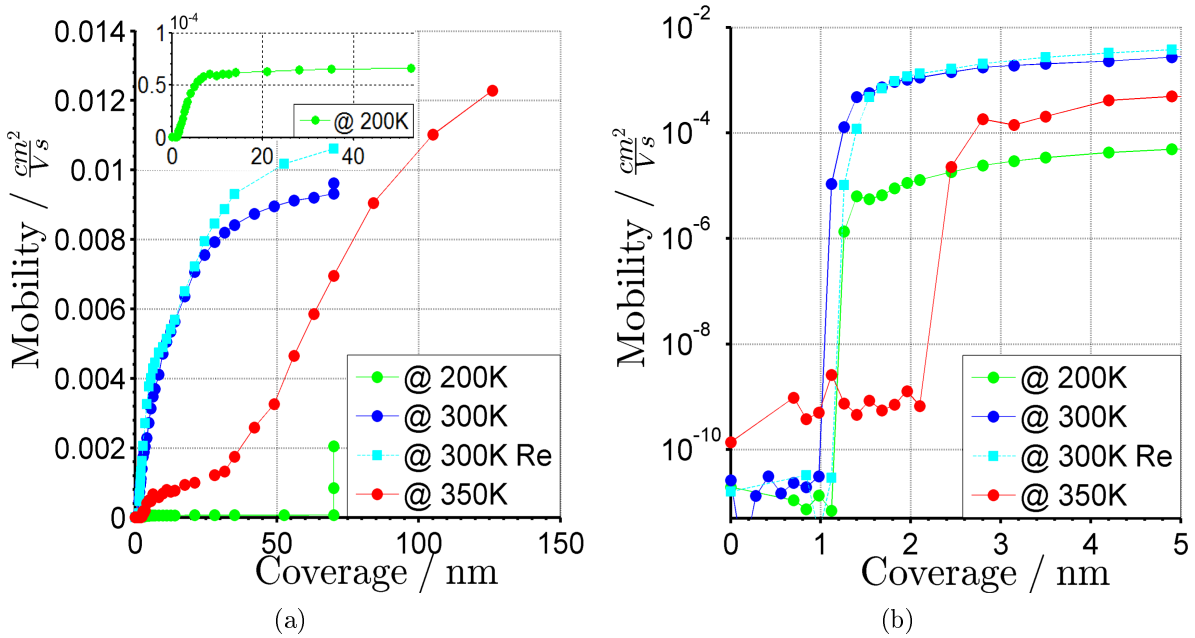

Figure 4.9: Coverage dependencies of OFET saturation mobilities. **(a.)** Coverage dependencies for films prepared at 200 K, 300 K and 350 K. After these measurements a retake: 300 K-Re was taken for comparability. The inset depicts the rescaled 200 K coverage dependency. **(b.)** Semilogarithmic plot of the mobilities for the first 5 nm.

In fig. 4.9 coverage dependencies of the mobility for surfaces with a well established carbon contamination were conducted. Fig. 4.9.a shows the linearly scaled coverage dependencies. An increase of mobility with temperature is expected as more energy is available to develop a lower grain density and a better internal grain structure [44]. Interestingly, the 350 K film only supersedes the 300 K film for high coverages. Fig. 4.9.b pictures a semilogarithmic plot for the first 5 nm of deposition. The onset of the mobilities for the 200 K and 300 K lies at ∼1 nm. This corresponds to 65 % of a ML and is therefore in good agreement with percolation theory, expecting the first paths connecting the electrodes at 67 % to 68 % [45]. However, the 350 K film exhibits first

transistor properties only at a coverage of ∼2 nm or 1.3 ML, which is confirmed in later experiments.

The 200 K film exhibits a distinct saturation at ∼7 nm or ∼4.6 ML whereas the 300 K film enters a damped saturation only at ∼40 nm or ∼26 ML. Interestingly, a minor kink can be observed at a coverage of ∼8 nm. Finally, the 350 K film shows a first saturation at ∼6 nm or ∼4 ML, but keeps growing until it supersedes the mobility of the 300 K film at ∼100 nm.

4.4.2 Morphology of 1.4 ML Films as a Function of Temperature

a.) Pentacene on SiO_2

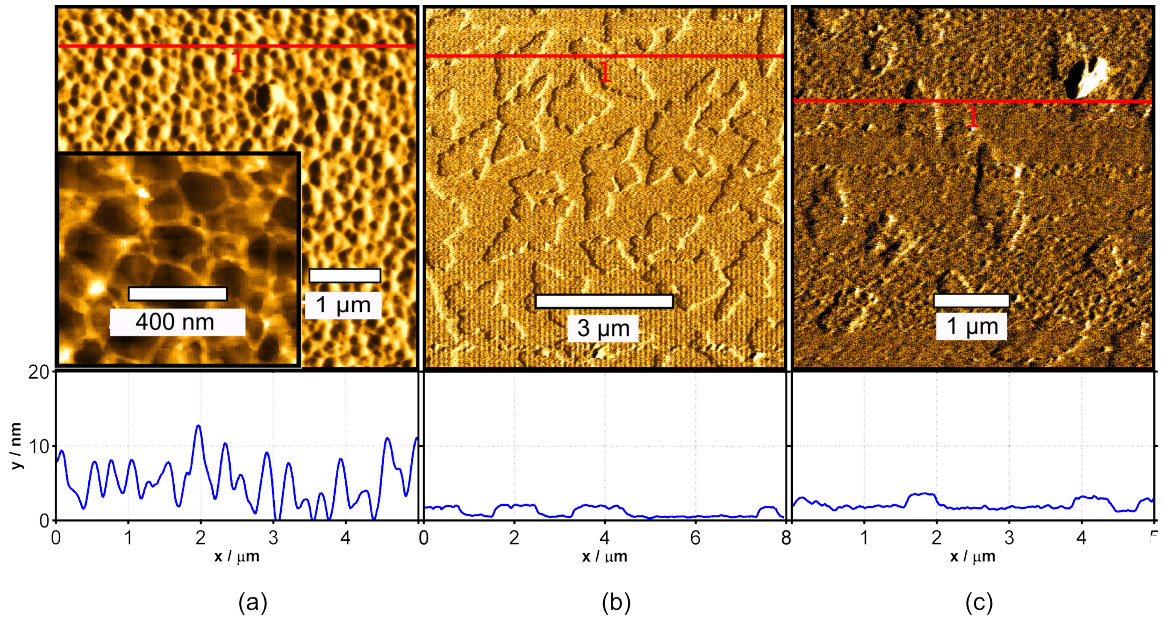

Figure 4.10: AFM images (derived data) of pentacene films on SiO_2 substrates with a nominal thickness of 1.4 ML for preparation temperatures of **(a.)** 200 K, **(b.)** 300 K, **(c.)** 350 K. Inset in **(a.)** depicts a phase channel image of a close up.

In fig. 4.10 the island growth on SiO_2 for a nominal thickness of 1.4 ML is pictured. Fig. 4.10.a exhibits a very disordered growth, caused by a very small diffusion length at low temperatures for the 200 K film. Interestingly the cross-section suggests a very high mean thickness which is in contradiction with the evaporated amount of pentacene.

This might be caused by a continuous overestimation of the islands by the AFM tip, caused by very pointy and high islands which are broadened by the probing tip. Whether these islands consist of standing or lying monomers cannot be told by the AFM images. However, because of its transistor properties, connected islands of standing monomers have to be present.

The 300 K film exhibits the growth of second layer islands on a fully intact first layer. This is consistent with the early formation of contact in the coverage dependency in ch. 4.4.1. At 350 K the second layer islands can also be observed, although the imaging proofs to be more difficult then on 300 K films. The troublesome AFM imaging of 350 K films is, although highly subjective, a persisting feature. It also turned out that previously sputter-cleaned samples made for easier AFM imaging. Albeit the development of an intact wetting layer, a conducting path between the electrodes is, according to the coverage dependency, not yet established. The reason for that is due to the growth behavior in the transition area (see ch. 4.4.2.c).

b.) Pentacene on Gold

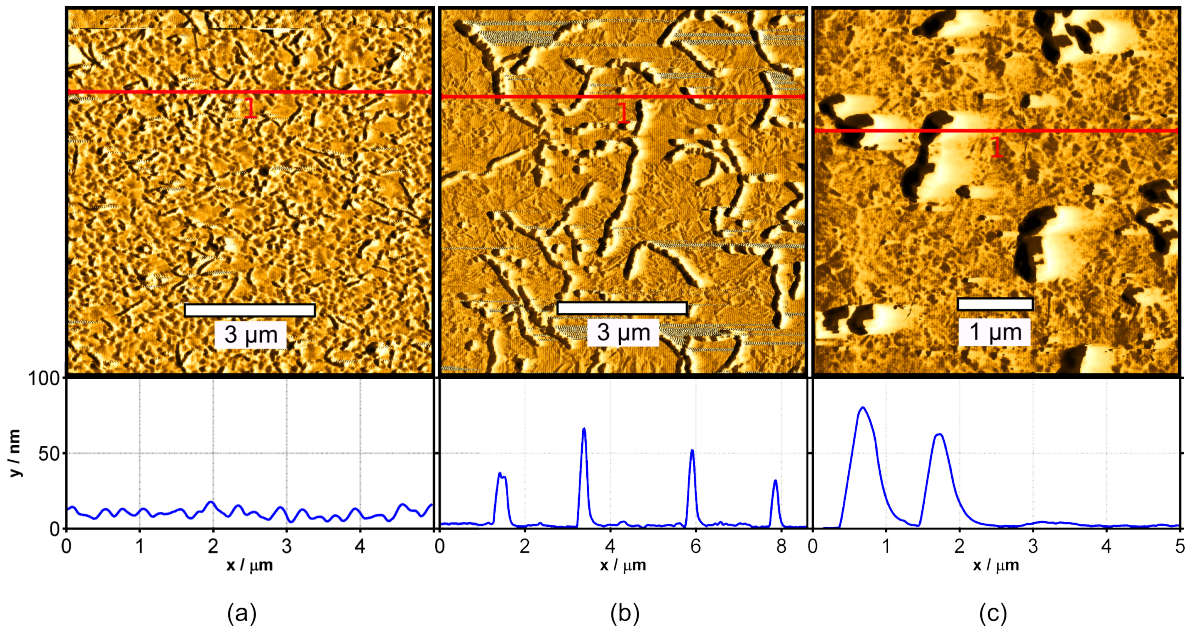

Figure 4.11: AFM images (derived data) of pentacene films on gold substrate with a nominal thickness of 1.4 ML for preparation temperatures of **(a.)** 200 K, **(b.)** 300 K, **(c.)** 350 K.

Pentacene film development on gold for a nominal thickness of 1.4 ML is pictured in fig. 4.11. 300 K and 350 K films exhibit a typical growth of *needle like* islands. Caused by the higher diffusion length, fewer but bigger islands develop at higher temperatures. Strong artifacts are present in the images due to the height of the islands. A crystallite structure is clearly visible beneath these islands which is strongly deviating from an untreated gold surface. Because of the higher bonding energy on gold a wetting layer of probably lying pentacene molecules develops beneath the islands. This is in good agreement with the pentacene growing behavior as described by *Käfer et al.* [21]. The 200 K film seems to exhibit both needle like islands of small height and disc like islands, similar as to the disc-like growth observed for low temperatures on SiO_2 substrates.

c.) Pentacene in Transition Area

In fig. 4.12.a the 200 K film exhibits a perfect connection of the semiconductor and the electrode. The isolated gold islands are visible only as a smoothed-out elevation of the film in front of the ascent to the electrode.

For the 300 K film the transition area consists of three regions: the growth in the channel, the growth on the electrodes and the growth between the ascent of the electrode and the isolated gold islands. The growth of the former two is discussed in the previous chapters. As for the latter, an undefined growth appears which is difficult to resolve with AFM imaging. Since we do not know whether the isolated gold islands are connected by a thin gold layer beneath the islands, two possibilities arise: (a.) The gold islands are connected and conductive, the real junction is where the pentacene on the SiO_2 touches the outmost gold islands. (b.) The gold islands are not connected and the junction consists of a mixed disordered pentacene island-growth. The transition area might function as a sink and gather more material then the nominal deposition amount as implied in ch. 4.3. Because of the isolated gold island structure it might even offer enhanced binding options which could lead to non desorbing carbon residues effecting the pentacene growth in other ways.

The AFM image in 4.12.b exhibits image artifacts of a broken tip or a picked up particle (triangular form often appearing in transition area). Within the channel a fully connected layer has developed and second layer islands are growing. It is notable that although within the channel very little third layer islands are visible, the inset in fig. 4.12.b pictures accumulated third layer islands developing at the junction. It is therefore

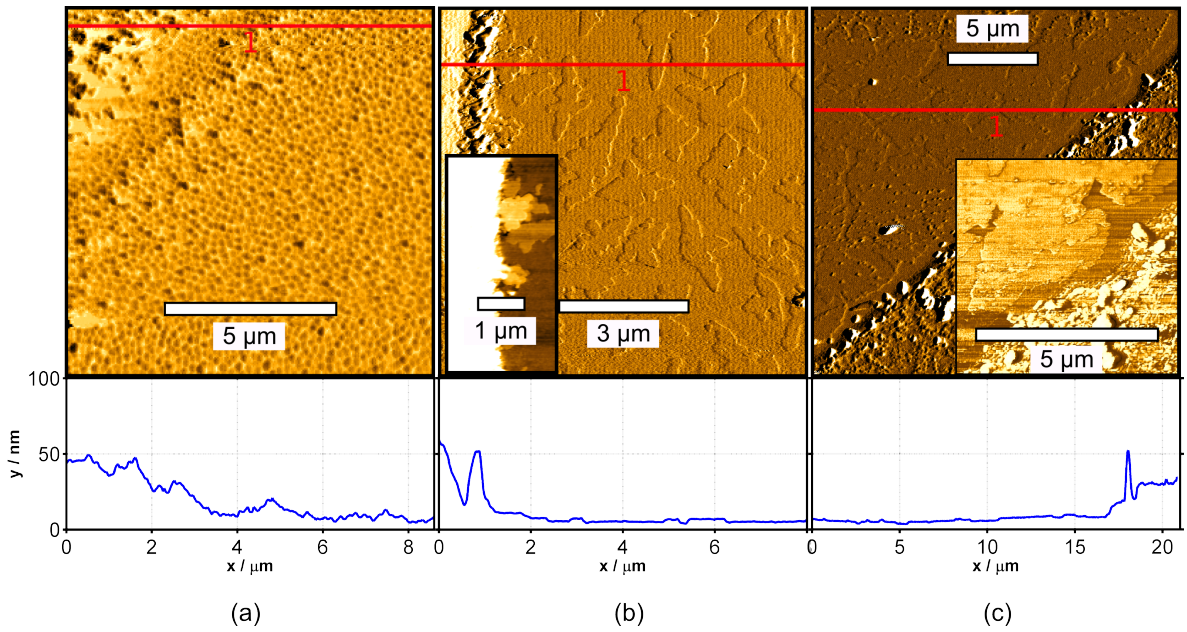

Figure 4.12: AFM images (derived data) of pentacene films in transition area with a nominal thickness of 1.4 ML for preparation temperatures of **(a.)** 200 K, Gold electrode in top left corner, SiO_2 in bottom right corner. **(b.)** 300 K, Gold electrode at left hand side, SiO_2 on right hand side. Inset depicting close-up of the AFM topography image with altered color scaling to emphasize multi-layer development. **(c.)** Coverage of 2.2 ML at $T = 350$ K, Gold electrode in bottom right corner, SiO_2 in top left corner (electrodes with lower height and no isolated gold islands due to intensive sputter experiments). Phase image inset of transition to emphasize pentacene dewetting effects.

already exhibiting an enhanced charge injection and high mobilities, which is shown in the electrical measurements (Fig. 4.9.b).

Because of difficulties resolving the junction at the 1.4 ML film prepared at 350 K, a different sample with 350 K and 2.2 ML is investigated in fig. 4.12.c. Various sputtering experiments reduced the electrode plateau to ∼20 nm and the isolated gold islands are gone. Nevertheless, the image exhibits the growth of a wetting layer and an almost completed second layer on top of it. Very little third layer islands are visible at this stage which resembles a layer by layer or Frank-van der Merwe mode. An interesting feature is the lack of an intact electrode-semiconductor junction which is emphasized

in the phase image inset in fig. 4.12.c. Over large parts of the transistor a depletion of the pentacene film in the vicinity of the gold contact of ∼1 μm is present which, in turn, strongly decreases or even prevents transistor properties. We suggest that this behavior is due to pronounced thermally activated dewetting as discussed in ch. 2.2.3. The 350 K film exhibits an onset of its mobility just at this coverage. The ex-situ AFM measurement may of course already differ from the morphology that was present at the time of the electrical measurements.

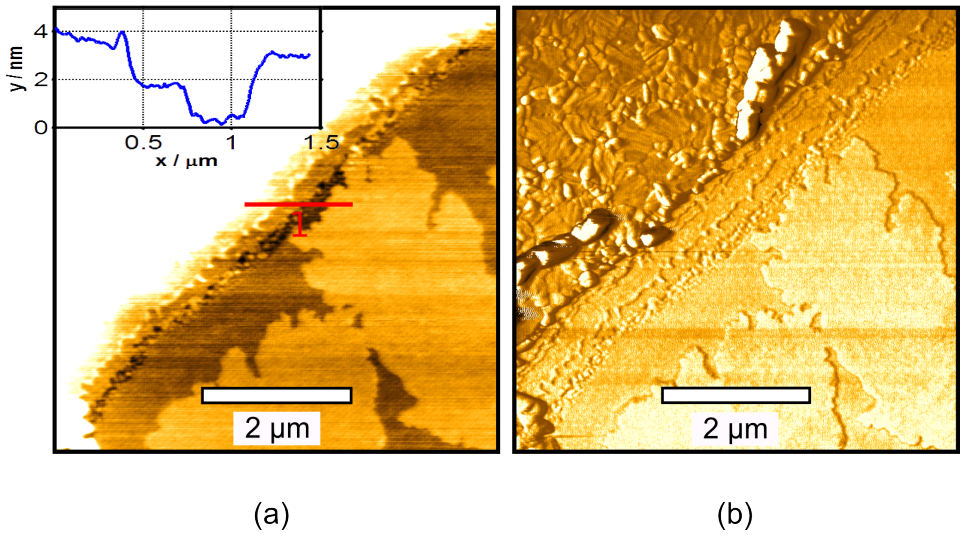

Figure 4.13: Sample with a coverage of 2.2 ML deposited at 350 K. **(a.)** Topography image with altered color scaling to emphasize the film growth development in the transition area. Inset picturing the cross-section sketched in the main image. **(b.)** Phase image of the same spot. Distinct lines can be seen in front of the electrode, suggesting a former multilayer connection of the film.

In fig. 4.13 a close-up on the transition area shows one of few preserved connections of the film with the electrode. The inset, picturing the cross-section marked with the red line, suggests sustained pentacene layers sticking to the electrode. In the phase image even multiple distinct lines are visible in front of the gold electrode, hinting to a former multilayer connection, as it is present at the 300 K film. This indicates that an initial connection of the film was achieved but developed into an improper connection. This might have been caused by thermal stress of the sample and might have ultimately resulted in the film *ripping* at its constraints after the film was grown.

Considering that the AFM images have to be taken ex-situ, care has to be taken

when relating morphological properties to electrical measurements. We strongly believe that the observed *ripping* of the films is a process with a larger time constant then the duration of consecutive electrical measurements performed for the coverage dependency. We associate the late onset of the mobilities at 350 K with respect to the 200 K and 300 K films to a different process. We suggest energetically unpreferable adsorption sites at the electrode-dielectric transition. At higher temperatures greater diffusion lengths lead to monomers avoiding these sites by augmented wetting layer completion in the middle of the channel, before the connection sites are filled up.

According to *Zhu et al.* monomers *hopping up* terraces is the dominating process in the pentacene thin film development [25]. By observing the roughness development of pentacene films the group concludes that hopping up of monomers occurs more often then hopping down, and is even present at room temperature. We believe that only when second layer islands develop, monomers from weakly bound sites, overcoming the *Schwoebel barrier*, can attach to the second layer, leading to the observed dewetting (Ch. 2.2). Because dewetting only occurs at high temperatures we conclude an increased *Schwoebel barrier* for hopping up transport for the first layer on SiO_2. Additionally, cracking of pentacene films was observed for large crystallites produced at high temperatures [46, 47]. Thus, we conclude that thermal cracks occur preferably at the gold-SiO_2 interface, generating weakly bound states which, at higher temperatures, lead to extensive dewetting.

4.4.3 Morphology of 6.8 ML Films as a Function of Temperature

a.) Pentacene on SiO_2

In fig. 4.14 the island growth for a nominal thickness of 6.8 ML is pictured. Fig. 4.14.a exhibits typical low temperature development for $T = 200$ K. Disordered islands dominate the surface instead of the typical terrace growth and no terraces can be resolved. The growth is governed by the drastically reduced diffusion length of the molecules. The cross-section suggests 4.7 intact ML below the surface above which the corrugated (measured) surface develops. A volume calculation yields $ML_{Vol} = 3.6$ ML. Because of the disordered growth the lower layers might only be poorly connected. Electrical measurements suggest that restructuring takes place if the sample is heated [44]. For 200 K films a saturation of the mobility is observed at 7 nm or 4.6 ML (ch. 4.4.1). The amount of layers contributing to the charge transport can be related to the number of

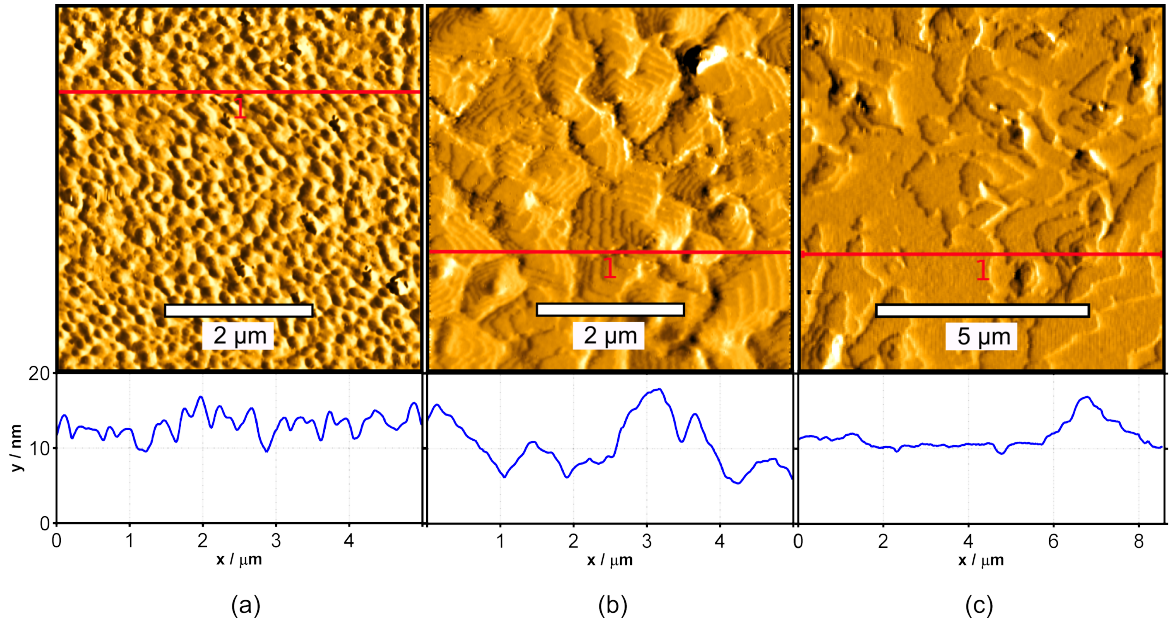

Figure 4.14: AFM images (derived data) of pentacene films on SiO_2 substrate with a nominal thickness of 6.8 ML for preparation temperatures of **(a.)** 200 K, **(b.)** 300 K, **(c.)** 350 K.

intact layers at the mobility-saturation coverage. For the regarded film with a nominal thickness of 6.8 ML this would amount to 4 ML. Considering a saturation of mobilities at 4.6 ML for 200 K films, this suggests that at least 1 ML less is involved, adding up to a maximum of contributing layers of 3 ML.

The 300 K sample (Fig. 4.14.b) shows a strong island development with a high roughness. Intact wetting layers of ML_{CS} = 3.6 ML and ML_{Vol} = 2.3 ML are estimated. The kink observed in the coverage dependency occurs at ∼8 nm or 5.2 ML, which would also fit an approximate 3 ML of intact layers.

Because of a higher diffusion length at 350 K the islands in fig. 4.14.c are flatter and better connected. The number of intact layers increases to ML_{CS} = 5.2 ML and ML_{Vol} = 4.9 ML. The first saturation of the mobility for this temperature sets in at 6 nm or 3.9 ML. Regarding the film growth for 2.2 ML in fig. 4.12 almost perfect layer by layer growth is observed. A 6 nm film would also result in a maximum number of connected layers of 3 ML contributing to the charge transport.

An additional sample was manufactured to evaluate the 200 K film growth on a pure SiO_2 substrate, directly after 10 minutes of sputter-cleaning. Fig. 4.15.(a,b) depicts a

3D representation and a 2D topography image of a 6.8 ML film. The cross-section yields evidence that even here steps of standing pentacene islands are present. The 3D view gives a better insight of how the island growth develops and demonstrates how the other represented 200 K film images can be interpreted. This is yet another demonstration of how sputter-cleaning directly before deposition makes for a more stable film which directly effects the quality of AFM images.

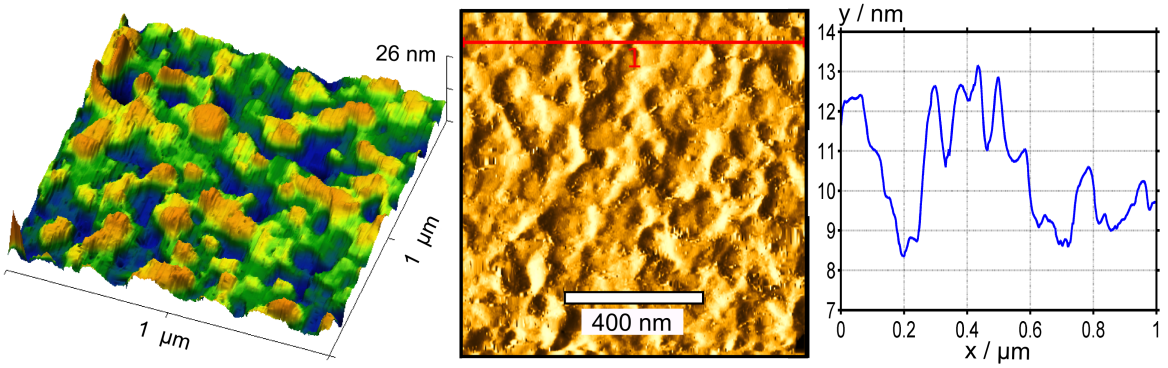

Figure 4.15: AFM images of a pentacene film on SiO_2 substrate deposited at 200 K, after 10 minutes of sputtering, with a nominal thickness of 6.8 ML. **(a.)** 3D topography image **(b.)** AFM image (derived data) **(c.)** Cross-section depicted as a red line in **(b.)**.

b.) Pentacene on Gold

In fig. 4.16 AFM images of a pentacene film with a nominal thickness of 6.8 ML on gold are pictured. The 200 K film (Fig. 4.16.a) develops almost the same on gold as on SiO_2. Image processing show that the grains on gold exhibit a slightly larger diameter then on SiO_2, which suggests a greater diffusion length of pentacene on gold. Whether the molecules in the islands on gold are lying or standing cannot be verified.

For the 300 K film (Fig. 4.16.b) few big islands of lying pentacene occur. The size and distribution of these islands is mostly governed by the diffusion length through the substrate temperature. The inset in fig. 4.16.b exhibits regular patterns beneath the islands, different to the pure gold surface and represents a wetting layer of probably lying pentacene molecules. For 350 K the development of a few big islands is, due to the higher temperature, even more pronounced. In between the bigger islands, small grains

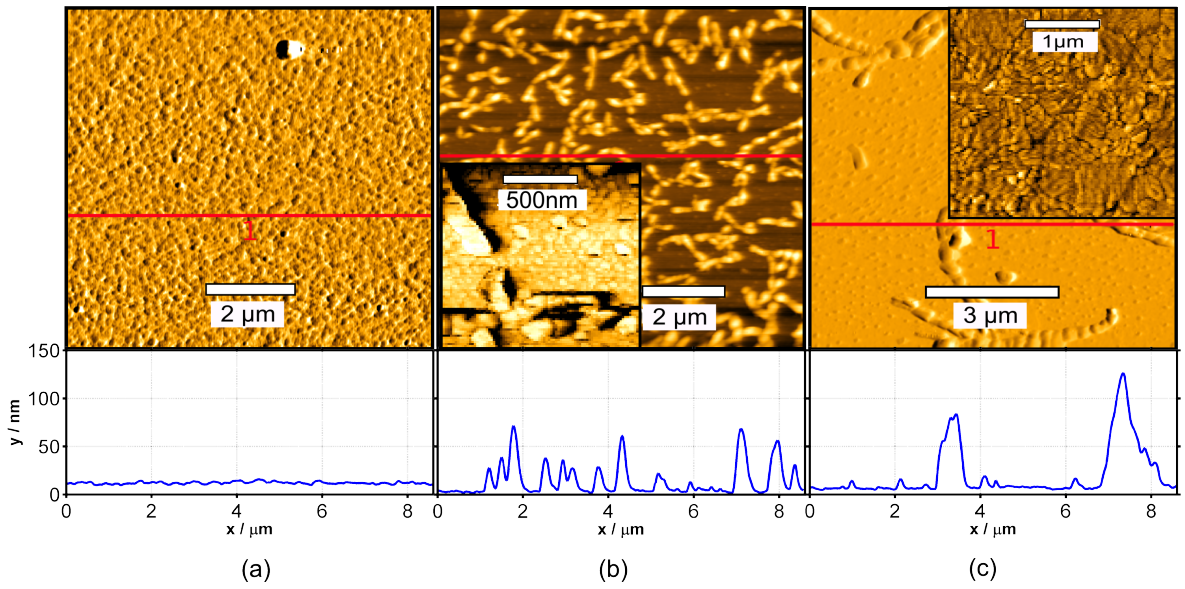

Figure 4.16: AFM images (derived data) of pentacene films on SiO_2 substrate with a nominal thickness of 6.8 ML for preparation temperatures of **(a.)** 200 K, **(b.)** 300 K, **(c.)** 350 K. Insets in **(b-c.)** are phase images depicting the lying ML of pentacene.

seem to be left of former islands, which are probably residues of former islands from previous TDS cycles. The inset of 4.16.c is an AFM phase-image zoom on the same sample. Here the crystallite structure of the wetting layer is even more distinct.

c.) Pentacene in Transition Area

In fig. 4.17 AFM images of the transition area are pictured with the gold electrode in the top-left corner and the SiO_2 surface in the bottom right corner. The 200 K film exhibits a remarkable smooth transition area with no obvious change in the growth, except for the grain sizes. A good connection of the pentacene film to the gold electrode is established. This suggests a non injection limited transport. Therefore the saturation of the charge carrier mobility with the coverage can be attributed to a maximum number of layers contributing to the charge transport as discussed at the beginning of this chapter.

In fig. 4.17.b the 300 K film is depicted. The needle like islands on the gold electrode develop until the edge of the transition with heights of ∼50 nm. A terrace like growth with high roughness is to be seen on the SiO_2 substrate. It is notable that the top of the pyramids start from the gold electrode and descend into the SiO_2 region. This

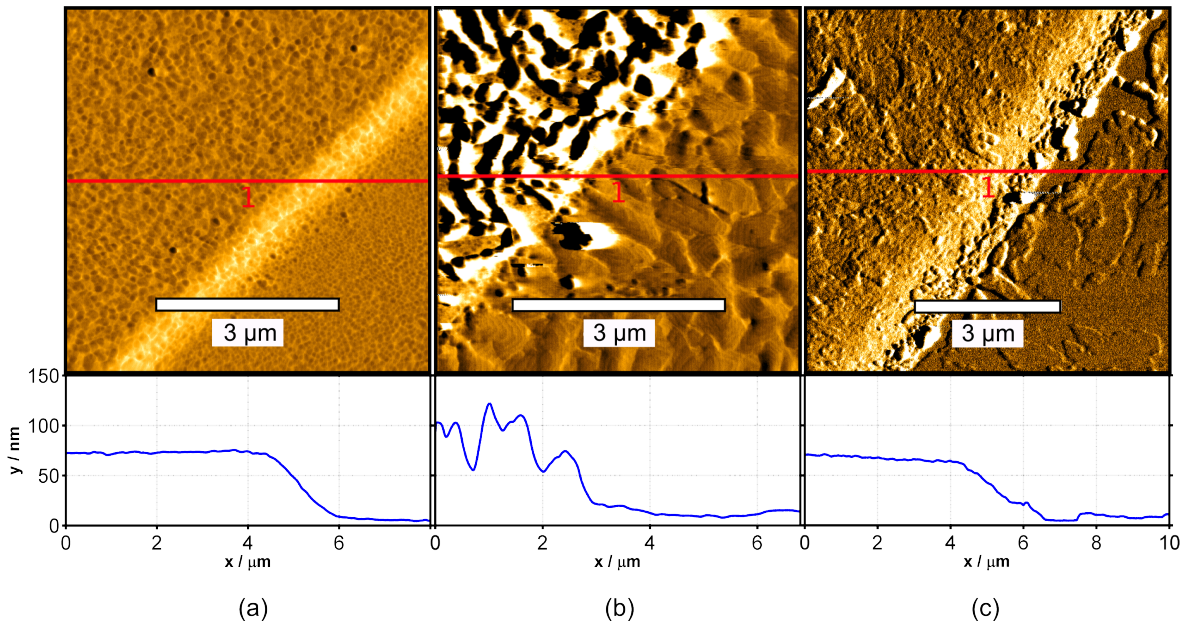

Figure 4.17: AFM images (derived data) of pentacene films in transition area with a nominal thickness of 6.8 ML for preparation temperatures of **(a.)** 200 K, **(b.)** 300 K, **(c.)** 350 K. Gold electrode in top-left corner, SiO_2 substrate in bottom right corner.

complements the observation of multilayers forming preferably at the contact, as seen in ch. 4.4.2 and displays an enhancement of the connection of the pentacene film with the gold electrode. Still, as the mobility keeps on growing with the coverage, a non-perfect connection has to be assumed, probably caused by the isolated gold islands resulting in mixed growth within the transition area. The well defined connection in this image might be attributed to a smooth gold-SiO_2 transition exhibiting no, or only few isolated gold islands. To test this assumption another sample with a coverage of 4.6 ML at 300 K was prepared. The sample was sputter cleaned for 10 minutes and one film of 4.6 ML was ad- and desorbed prior to the deposition of the final film. In fig. 4.18.a it exhibits few, big islands of many layers within the channel, but close to the contact an enforced development of many small-diameter islands of the same height as the islands within the channel is observed. This indicates a decreased diffusion length or an enhanced cluster formation in the area of the isolated gold islands, resulting in poorly connected lower layers and further decreases the development of a good film-electrode junction, which could explain the slow rise of the mobility in the coverage dependency (Ch. 4.4.1).

The change of growth between fig. 4.17.b and fig. 4.18.a indicates a difference in the substrate surface and hints to either, a different surface *in front* of the isolated gold island, or a difference in development of the carbon contamination after sputter cleaning in this area. This would be particularly strong for this sample with only one TDS cycle prior to deposition. However, this highlights the importance of the substrate transition area as the pentacene film growth demonstrably changes strongly, even within a wide range of the transition.

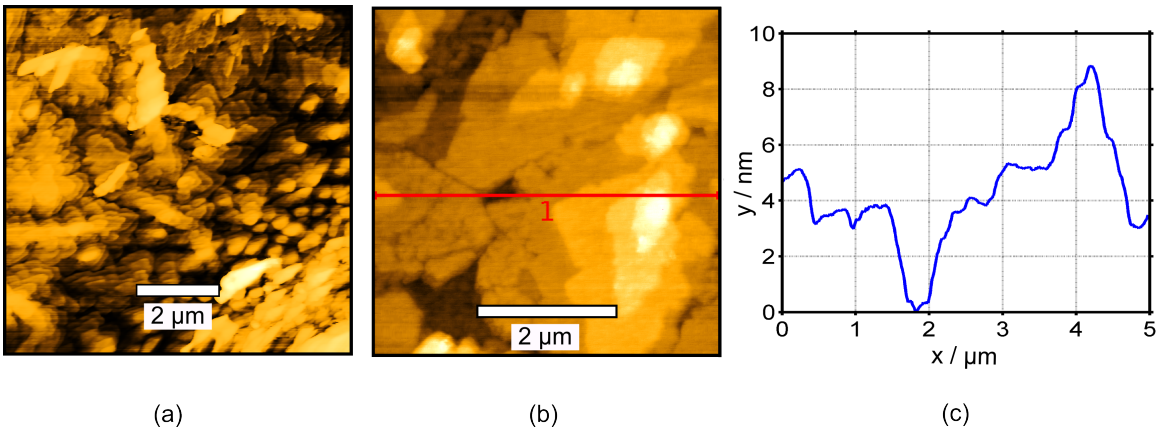

Figure 4.18: **(a.)** AFM topography image of a 4.6 ML, 300 K film in the transition area. Gold-electrode to the bottom right. Accumulation of smaller grains near electrode. **(b.)** AFM topography image of a 6.8 ML, 350 K film on pure SiO_2 substrate. Pentacene multilayer steps visible within the film. **(c.)** Cross-section depicted as a red line in **(b.)**.

Another process is active for the 350 K film in fig. 4.17.c, where pronounced dewetting at the transition takes place. The film is clearly avoiding the contact to the electrode and multilayer-steps occur where the film is rising within the channel. This must inevitable be of great influence on the electrical performance of the OFET. No needle like islands are seen on the gold surface close to the transition region because of the strongly increased diffusion length of the pentacene molecules at this temperature as discussed in ch. 4.3. The strong discrepancy of the growth between the 300 K and 350 K films is even more incomprehensible as the higher diffusion length of the 350 K film suggest a stronger pentacene *sink* in the transition area and therefore a larger amount of the semiconductor restricted to this area. A possible explanation for this phenomena is already discussed for the 350 K 1.4 ML film (Ch. 4.4.2). Higher temperatures lead to

thermal stress and micro-cracks within the film. Also because of the higher temperature, the large *Schwoebel-barrier* for *hopping up* of pentacene monomers can be overcome and energetically unpreferable sites can be avoided. This would be a strong indication for a high Schwoebel barrier only for the first layer (dewetting barrier).

Furthermore, fig. 4.18.b pictures a film prepared at 350 K on a SiO_2 substrate. Even within the film multilayer valleys are present (Fig. 4.18.c). The second lowest layer exhibits cracks and holes, contrary to the higher terraces, which appear to be smoothly developed. This indicates dissolving of parts of the lowest layer and formation of an ad-layer on top of it. This behavior only occurs at higher temperatures, further supporting temperature-assisted hopping transport. Although volume calculations propose more intact layers beneath the visible surface, the fact that this behavior only occurs within one specific layer, suggest an energetic particularity. It is therefore probable that either the first or the second layer exhibit this development. Similar cracks and holes are observed for high temperature films at the lowest layer. This indicates pre-deposition contamination close to the transition, causing structural disturbances in the lowest layer.

4.4.4 Morphology of 22.7 ML Films as a Function of Temperature

Approaching thick films, the thin film phase will slowly change into the bulk phase, especially for higher temperatures [9]. Imaging of thicker films proofs to be more troublesome as loose *debris* tends to stick to the AFM tip and results in image artifacts. It is notable that such behavior is not occurring when scanning thick films on pure SiO_2 substrate which is not contaminated by successive TDS cycles. Whether this is due to contamination after consecutive TDS cycles or a result of a large scale diffusion influence on the film growth caused by the gold electrodes could not be clarified.

a.) Pentacene on SiO_2

The development of the 200 K film proceeds as is expected from the low coverage measurements. The 300 K film exhibits particle like elevations within the channel (possibly bulk phase). The expected pyramid like structure is hard to resolve but is indicated as the background structure in fig. 4.19.b. The basic growth at 350 K is similar to the 300 K film although the pyramid islands between the particle structures exhibit a larger mean diameter. Between the elevations an image of the terrace structure was successfully taken in fig. 4.19.c. The mobility of the film for 300 K and 350 K keeps on

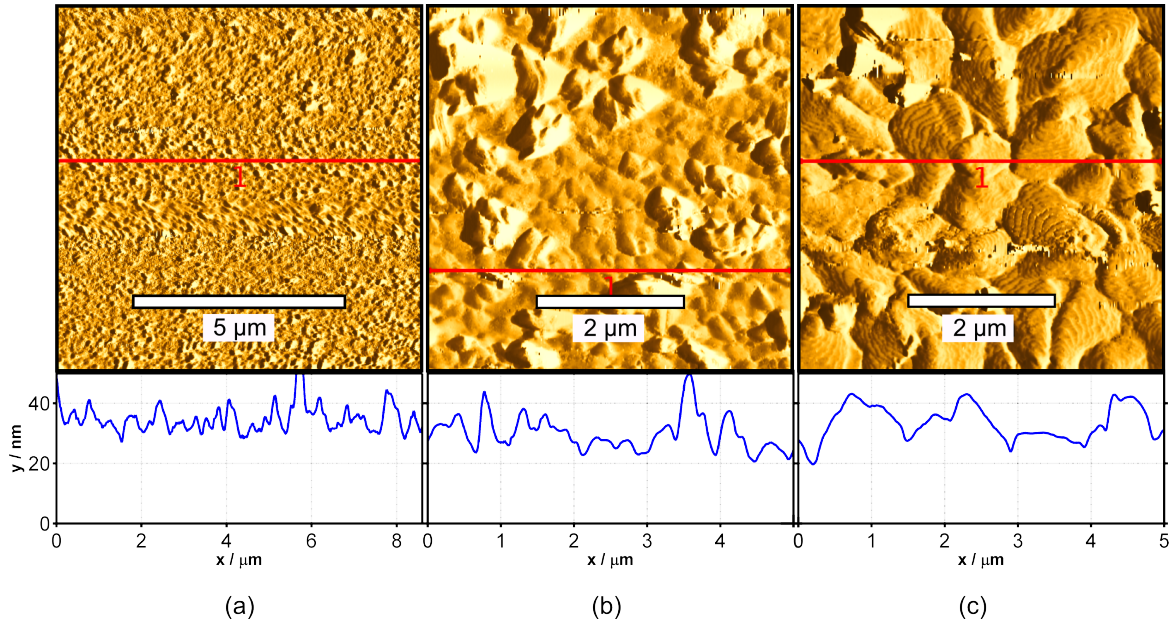

Figure 4.19: AFM images (derived data) of pentacene films on SiO_2 substrate with a nominal thickness of 22.7 ML for preparation temperatures of **(a.)** 200 K, **(b.)** 300 K, **(c.)** 350 K.

rising but, since we expect only the first 3 ML to participate in the charge transport, we attribute this to a better connection of the film with the electrodes with increasing coverage. As the 350 K mobility eventually supersedes the 300 K film we suggest that this is due to a better intrinsic mobility, caused by fewer grain boundaries of the lowest MLs and probably a better inner structure, and is only hampered by a poor connection to the electrode [44].

b.) Pentacene on Gold

For the 200 K film on gold the growth proceeds to resemble the one for low coverages. At 300 K the needle like islands from the lower coverages grow and start to connect, resulting in a rough film. The islands of the 350 K film grow bigger whereas the background evolves in an island like growth as well.

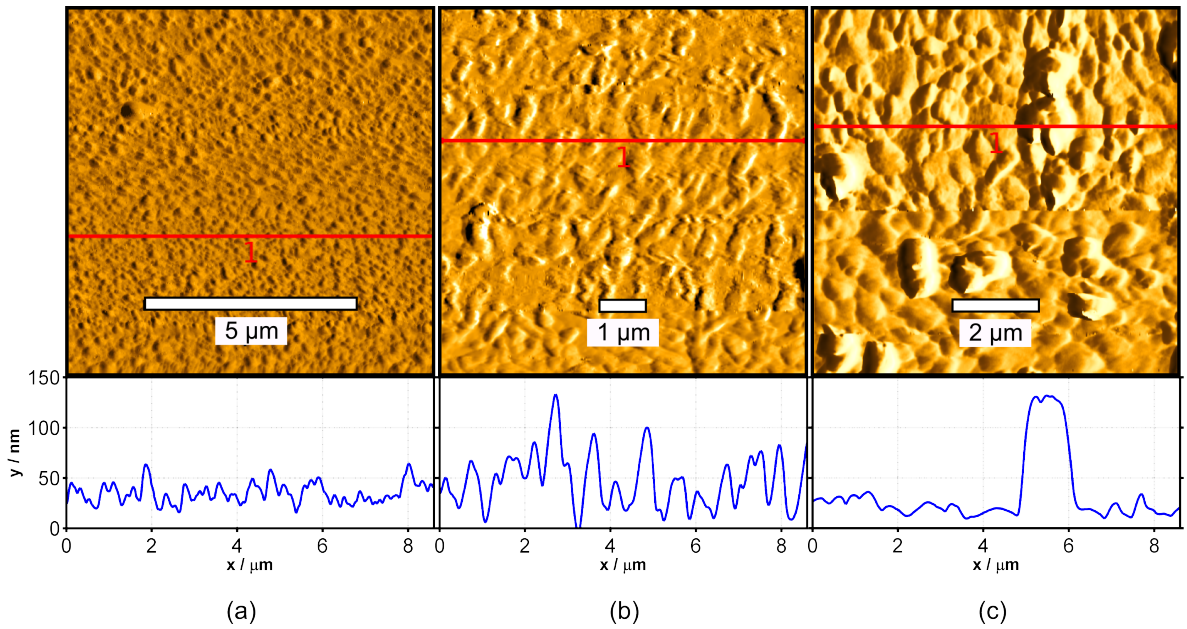

Figure 4.20: AFM images (derived data) of pentacene films on gold substrate with a nominal thickness of 22.7 ML for preparation temperatures of **(a.)** 200 K, **(b.)** 300 K, **(c.)** 350 K.

c.) Pentacene in Transition Area

The low temperature film continues its smooth development with increasing coverage. Again, slightly larger islands can be observed on the gold electrode.

A large scale image of the 300 K sample is shown in fig. 4.21.b where needle-like islands are stretching into the channel. Their appearance is concentrated parallel to the electrodes and might be caused by the isolated gold islands. In between the islands and the electrode the film is still developing a better connection with increasing coverage as the saturation of the mobility only sets in at ∼26 ML. Sole big grains can also be observed within the channel, which is probably bulk-phase, developing on top of the thin-film phase.

The 350 K film exhibits different growth in the outer channel compared to the middle of the channel. The outer channel region consists of similar sized islands with big gaps in between. In the inner part of the channel an augmented growth of large islands (probably bulk phase), similar to the 300 K film, can be observed. The mobility for the 350 K film keeps enhancing with ongoing coverage, superseding the 300 K only at coverages greater then ∼65 ML. As the junction exhibits strong dewetting, as shown

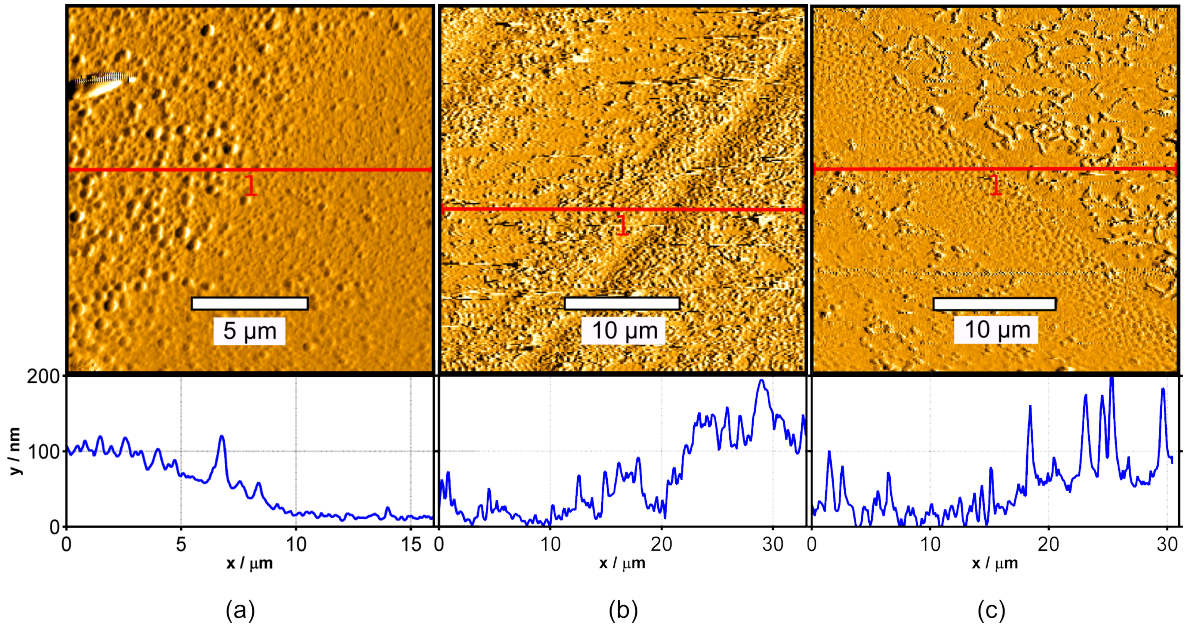

Figure 4.21: AFM images (derived data) of pentacene films in transition area with a nominal thickness of 22.7 ML for preparation temperatures of **(a.)** 200 K, Gold electrode in top-left corner, SiO_2 in bottom-right corner. **(b.)** 300 K, Gold electrode in bottom-right corner and emerging again in top-left corner. **(c.)** 350 K, Gold electrode in top-right corner, SiO_2 in bottom-left corner.

for smaller coverages, we suggest that the multilayer semiconductor-gold gap is only slowly filled when monomers are getting trapped within the gap, further enhancing the connection. Another reason for its slow rise in mobility with the coverage is the large amount of pentacene diffusing into the channel from the gold electrodes. As discussed in ch. 4.3 it collects more then four times the amount of pentacene compared to the 300 K film. As this pentacene is expected to grow in an island-like shape, similar to the on-gold growth, this will further hinder the development of a well connected junction.

4.5 Influence of Sputter Cleaning

4.5.1 AFM Investigation

In fig. 4.22 pentacene films on differently prepared, pure SiO_2 substrates are depicted. The images clearly show that fewer but bigger islands are growing on a freshly sputter-cleaned surface. The mean island density ρ_I, evaluated by a threshold height algorithm, is growing with the amount of carbon contamination. We could not verify that the amount and kind of carbon residues left after several TDS is similar to the initial atmospheric contamination.

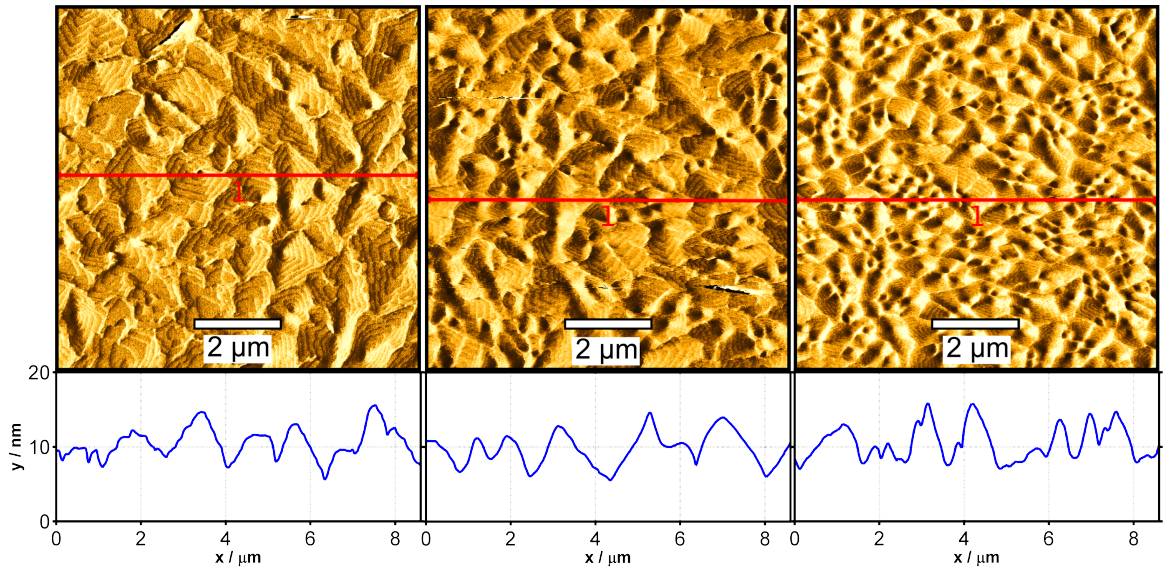

Figure 4.22: AFM images (derived data) of the pentacene film on SiO_2 substrate with a nominal thickness of 6.8 ML. **(a.)** Sample was sputter cleaned for 10 minutes and annealed at 650 K. $\rho_I = 2.9\,\text{Islands}/\mu\text{m}^2$ **(b.)** Sample was sputter-cleaned and annealed. A 6.8 ML film was then ad- and desorbed before depositing the final film. $\rho_I = 4.1\,\text{Islands}/\mu\text{m}^2$ **(c.)** Sample experienced no treatment at all. $\rho_I = 6.3\,\text{Islands}/\mu\text{m}^2$

Since the roughness of the surfaces is experiencing little or no change with sputtering as discussed in ch. 4.1.1, the change of growth has to be attributed to the surface contamination. It is also a persistent attribute that films on sputtered surfaces are better to resolve with AFM then their carbon contaminated counterparts. Both can be explained by a chemical interaction of the pentacene growth on carbon. If the carbon

occurs as an average polymeric carbon layer as suggested by *Seah et. al* [48] a chemical interaction can limit the diffusion length. Additionally, the layer might be more weakly bound and structured which could result in a deteriorated imageability with AFM.

Another explanation would be that carbon islands act as nucleation centers for the development of pentacene crystallites. This would support the development of new grains which would therefore cause a higher island density.

4.5.2 Electrical Characterization

Coverage dependencies as described in ch. 4.4.1 were performed. The samples were sputter-cleaned for 10 minutes (Ch. 3.2.3) and then heated to 650 K before depositing pentacene. The results are plotted in fig. 4.23. The saturation mobilities were evaluated according to ch. 2.4.

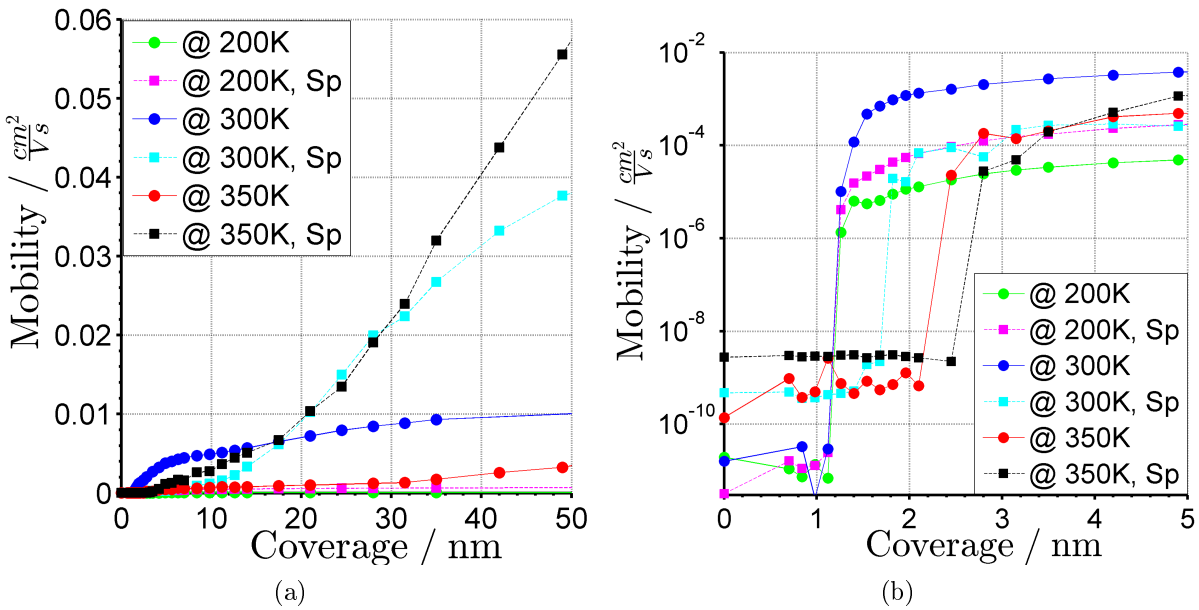

Figure 4.23: Comparison of coverage dependent mobilities for carbon contaminated (circles) and previously sputter-cleaned samples (squares). **(a.)** Charge carrier mobilities for films prepared at 200 K, 300 K and 350 K. **(b.)** Semilogarithmic plot of the mobilities for the first 5 nm.

It turns out that the sputter-cleaned samples supersede their carbon covered counterparts in terms of mobilities for all temperatures. The only exception is the sputter-cleaned 300 K film which exhibits a first saturation plateau at ∼5 nm or ∼3 ML and only

afterwards shows a strong rise in mobility, superseding the unsputtered counterpart only at ∼17 nm. The plateau behavior is very pronounced for the unsputtered 350 K film and also, in weaker development, visible for the 300 K film (Ch. 4.4.1).

The plateaus for the 300 K and 350 K films occur at 8 ML and 6 ML, respectively, which also matches the development of the first three intact layers. We therefore suggest that the first saturation or kink commences once the connected layers, contributing to the charge transport, are developed (Ch. 4.4.3).

Another obvious feature is the upwards and sidewards shifts of the mobility in fig. 4.23.b of the sputtered 300 K and 350 K and the non-sputtered 350 K sample. The upwards shift for mobilities, before the formation of a conducting channel sets in, is associated with an increased leakage current, which is understandable for the 350 K films. An increased leakage current might also be present after insufficient annealing of the substrate after sputtering (Ch. 3.2.3). The sidewards shift however is directly related to the channel formation and therefore to the film growth process. We suggest that the observed sidewards shift for the unsputtered 350 K film is associated with a thermally increased diffusion length and late filling of the energetically unpreferable junction sites. Consequently the shift for the sputtered 300 K and 350 K film has to be associated with an increased diffusion length due to the removal of contaminants.

4.6 Threshold Voltage

The threshold voltages of different devices exhibit significant shifts of up to 50 V. Traps have been associated with the origin of the shift and several models have been proposed in literature. Formation of long living volume traps by the application of a bias stress would result in immobile holes screening the gate bias [49]. The process of formation is discussed with different models, proposing the reversible creation of a change in the micro-structure, yielding traps, or the permanent integration of impurity molecules into the lattice. Misalignment within the lattice, caused by substrate roughness and impurities are supposed to further enhance the formation of trap states, proposing deep volume traps situated at the interface and shallow traps to be located within 1 nm to 4 nm of the interface [50, 51]. The preparation of the substrate is therefore crucial for the observed shift of the threshold voltage [52].

In fig. 4.24 the development of the threshold voltages V_{Th}, extracted from the saturation regime from the mobility-coverage dependencies (Ch. 3.2.3, Ch. 4.4.1) are depicted.

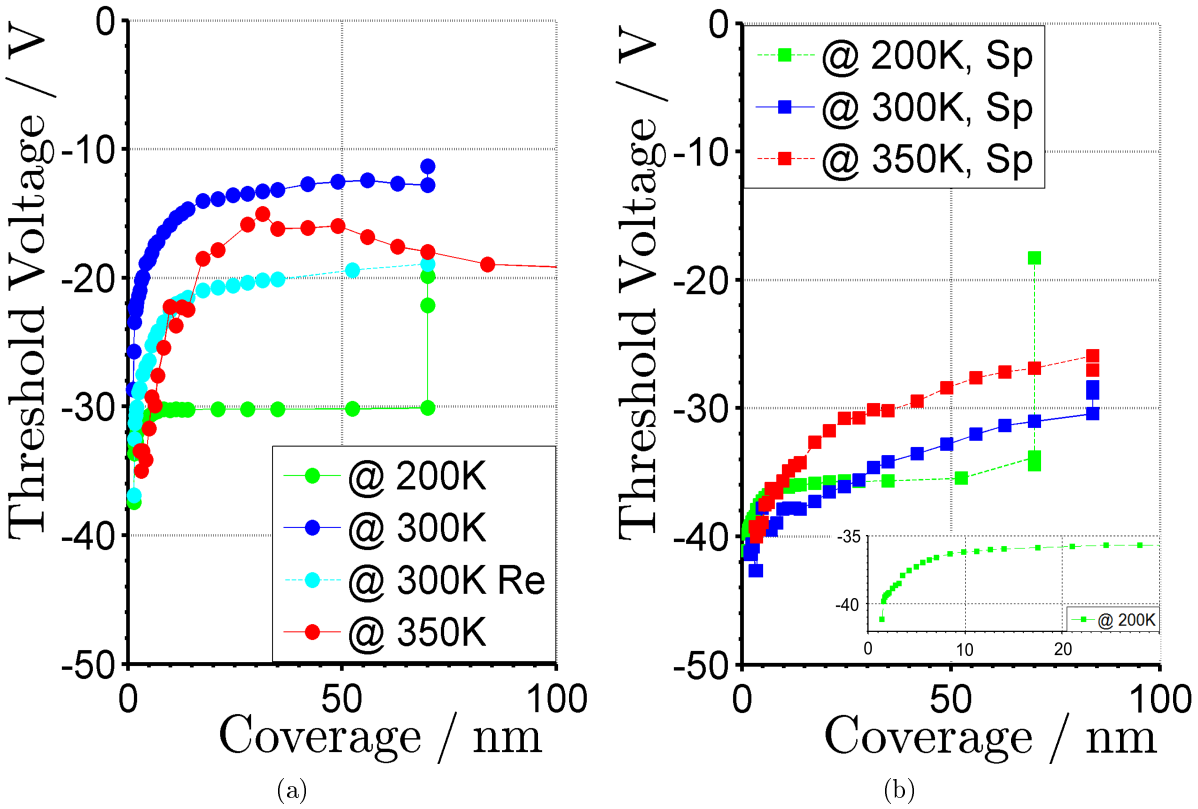

Figure 4.24: Development of threshold voltage with coverage. **(a.)** Executed on well carbon contaminated samples. **(b.)** 10 minutes sputter cleaned and annealed prior to deposition.

Multiple values occurring for the same final coverages signify the time and temperature development when heated/kept/cooled to 300 K. Fig. 4.24.a illustrates the development for a carbon covered substrate with temperatures of 300 K, 350 K and 200 K and the remeasured 300 K. Depositing the film is slowly compensating the interface trap states and is causing a rise in the threshold voltage. Development of shallow traps in ad-layers will further shift the threshold voltage upwards.

The 300 K films exhibit a strong saturation at ∼10 nm. This is close to the observed kink in the mobility dependence and suggests the amount of fully connected layers that are contributing to the charge transport and are therefore effected by the formation of traps. The strongest change is observed within the formation of the first layer.

A similar behavior with an earlier saturation is seen for the 200 K sample. This is expected because of an earlier formation of fully connected layers due to its different growth behavior.

The 350 K film however shows no saturation with the completion of the fully connected layers and even exhibits a peak in the threshold voltage at ∼30 nm, after which it starts to decay again. This coincides with the start of the second rise of the mobility with the coverage. It is our interpretation that massive restructuring takes place for critical substrate zones at high temperatures (transition areas, grain boundaries). In the dewetting areas of the former mentioned zones the film still exhibits thicknesses smaller then the amount of layers that are contributing to the charge transport (Ch. 4.4.3). Although the nominal deposition amount is already way above the amount of the contributing layers, restructuring in these zones still leads to the re- formation of trap states in these active layers and hence, influences the threshold voltage. Only for high coverages a change in the threshold voltages subsides and the final formation of the lowest layers is finished.

The overall offset between the first 300 K film and the successive coverage dependencies (350 K, 200 K and the remeasured 300 K) is caused by an increase of the carbon contamination due to an additional TDS cycle. As suggested by *Völkel et al.* [51] this shift has no effect on the calculated charge carrier mobilities (Ch. 4.4.1). It is peculiar that for the first 300 K coverage dependency the threshold voltages is not yet stabilized although already four TDS cycles (10 nm each) have been executed previous to its deposition. This indicates that a saturation of the carbon contamination was only achieved after the first coverage dependency measurement. Because the offset is only present for different contamination levels, the amount of interface traps is strongly governed by the substrate surface itself rather then the film-growth parameters.

Fig. 4.24.b depicts the threshold voltages for samples that were sputter cleaned and annealed prior to deposition. The 200 K film exhibits a similar development and saturates at the same coverage as its unsputtered counterpart. The inset depicts a rescaled illustration up to a coverage of 30 nm.

Both the 300 K and 350 K film are originating from the same threshold voltage as the 200 K film, hinting that the sputter-cleaning procedure always achieves a comparable surface, defining the volume trap states. The splitting of the curves only starts with the development of additional layers, starting at ∼4 nm, although the measurements exhibit great variations due to weakly defined transfer characteristics at low coverages. Apart from the grain boundaries it is at this coverage that the morphology of the 300 K film starts to divert from the 350 K film, as it is developing higher islands. It is therefore likely that the traps are not originated in the grain-boundaries but rather in the

SiO_2/pentacene interface and the successive pentacene/pentacene interfaces that are contributing to the charge transport. It is noteworthy that, starting with a coverage of ∼30 nm, both films exhibit an almost parallel development of the threshold voltage, indicating that the same process is now dominating the trap formation. The saturation is only weakly pronounced compared to their unsputtered counterparts. This might be caused by an overall enhanced restructuring process, originated in a better inner lattice structure due to higher diffusion lengths.

Another interesting feature is observed when regarding the final points in the graphs, representing the threshold voltages when heated/kept/cooled to 300 K. A great change in threshold voltage is observed for the 200 K films. This can be attributed to an irreversible restructuring process within the active layer as shown in our previous work [44].

The 300 K and 350 K films exhibit only minor changes, which, for the sputtered samples, even develop to the same final value. This is a further indication that the grain boundaries are not the cause for the trap states, as the threshold voltage nears the same value but the maximum drain currents, associated with the grain boundary density, keep apart.

5 Conclusion

Coplanar bottom-gate organic field effect transistors with field effect mobilities comparable to literature values are manufactured. Active pentacene films on SiO_2 with highly reproducible transistor properties are prepared by establishing either a saturated carbon contamination or a freshly sputter-cleaned surface for a given sample.

By evaluating the film growth for various temperatures and observing the mobility as well as the threshold voltage development, the first three monolayers are found to contribute the better part to the charge transport. By regarding the mobility development of transistors prepared at different temperatures and on differently prepared substrates, we conclude that the field effect mobility is mostly limited by grain boundaries and the inner crystal structure. Different values of field effect mobilities between samples are attributed to injection limitations, due to the development of an insufficient semiconductor-electrode junction. We suppose substrate morphologies and contamination effects in the transition area to cause these effects.

We demonstrate evidence of pronounced pentacene-dewetting at higher surface temperatures for pentacene deposition, exceeding the often stated *best temperature* of $\sim$330 K. Furthermore we introduce a novel model for film development and dewetting-processes, dominated by *hopping down* and *hopping up* transport of monomers between layers. For the wetting layer we propose an elevated *Schwoebel barrier* for *hopping up* transport which is only overcome by monomers at temperatures exceeding $\sim$330 K. Monomers hopping on top of the wetting layer will drop back as long as non-occupied adsorbent sites exist. Only if the first layer is fully formed and second layer grains develop, dewetting will occur. Then defects within the film act as a source for dewetting and result in depletion areas of several microns in diameter.

Finally we are able to attribute the offset in the threshold voltage solely to the dielectric interface, whereas the development of the threshold voltage with the film thickness is caused by intra-layer trap development. Furthermore we obtained data suggesting that grain boundaries are not involved in the shift of the threshold voltage.

6 Appendix

6.1 Matlab Analysis Code

6.1.1 LabView Data Processing

```
%% Reading LabView Data
clear all

counter = 0; SubFileCounter = 0;
Header = {{}}; Data = {{}};% Cell in cell, for indexing!
stop_sign = 1; %necessary for checking double occurence: 'Measurement End'

%%
[filename,pathname] = uigetfile('*.txt','Select the LabView data file');
cd (pathname)
infile = fopen(filename);

while not(feof(infile)) % feof is 1 if file is at end
    counter = counter+1; % noting lines, not necessary
    textline = fgetl(infile);  % read line
    if isempty(textline) % ignore empty lines
        ...
    elseif isletter(textline(1)) % check for letters
        if strfind(textline,'Measurement Seassion') %Trigger Word
% SubFile created for every session
            stop_sign = 0; % marking: in-between Meas Start and Meas End
% Measurement Start and Measurement End, Ignores Data Outside KeyWords
            SubFileCounter = SubFileCounter+1;
            Header{SubFileCounter,:} = []; Data{SubFileCounter,:} = [];
% new header sub-cell, empty input to avoid indexing problem
```

```
        elseif strfind(textline,'Measurement End')
            stop_sign = 1; % dont read values outside keywords
        else
            Header{SubFileCounter,:} = [Header{SubFileCounter,:}, ...
            {textline}]; % Write in header sub-cells
        end

     elseif isnumeric(sscanf(textline,'%f %f %f %f %f'))% check for numbers
         if strcmp(textline,...
           '0.000000E+0 0.000000E+0 0.000000E+0 0.000000E+0 0.000000E+0');
         % ignore inputs of zero values (LabView Error)
         elseif stop_sign == 0; % if in-between Meas Start and Meas End
% write data to file
            [a,b,c,d,e] = strread(textline,' %f %f %f %f %f','delimiter',',');
            Data{SubFileCounter,:} = [Data{SubFileCounter,:};a,b,c,d,e];
         else
             ...
         end
    end
end
fclose(infile); % closing file

%% Processing Data
Device = struct();
DataTypeArray = [];

for k = 1:SubFileCounter
    %% Splitting Data per stepped gate voltage
    testdata = Data{k};  % how to access data in new structure
    data_length = length(testdata);
    derivative = diff(testdata(:,5)); %whera are the voltage steps
    indices = find(derivative ~= 0); %find indices
    indices = [0;indices]; numel_steps = numel(indices); % How many steps?
    data = {}; % creat cell

    if indices == 0 % if no steps are detected,
        data (:,:,1) = {testdata}; %insert whole date - otherwise -> error
    else
        for l = 1:numel_steps-1
            a = testdata(indices(l)+1:indices(l+1),:);
```

```
% only data for the first step
            data(:,:,l)={a}; % appending other data
        end
        data(:,:,numel_steps) = ...
        {testdata(indices(end)+1:indices(end)+indices(2),:)};
% appending data for the final voltage step
    end

    %% Replacing characters not used in MatLab
    Header{k}(3) = strrep(Header{k}(3), 'Date:', '');
    Header{k}(3) = strrep(Header{k}(3), ' ', '_');
    Header{k}(2) = strrep(Header{k}(2), 'Measurement Name:', '');
    Header{k}(2) = strrep(Header{k}(2), ' ', '');
    Header{k}(2) = strrep(Header{k}(2), '-', '_');
    Header{k}(2) = strrep(Header{k}(2), '.', '_');
    Header{k}(2) = strrep(Header{k}(2), '''', 'Sp');
    Header{k}(2) = strrep(Header{k}(2), '<', '');
    Header{k}(1) = strrep(Header{k}(1), 'Device Name:', '');
    Header{k}(1) = strrep(Header{k}(1), ' ', '_');
    Header{k}(1) = strrep(Header{k}(1), '-', '_');
    Header{k}(1) = strrep(Header{k}(1), '.', '_');
    Header{k}(1) = strrep(Header{k}(1), '''', 'Sp');
    DataType = Header{k}{5}(24)== 'B'; DataTypeArray = ...
    [DataTypeArray,DataType]; % Identifies Transfer and Output curves
    Device = setfield(Device,['M',num2str(k),Header{k}{1},'__',...
    Header{k}{2}],{data,Header{k}});  % appending subfile number
end

%% Creating formatted .txt files for further processing
TextFiles = input('Do you want to create formatted Textfiles? (Type 1): ');

if TextFiles == 1;
    foldername = uigetdir; % Open directory to store data
    names = fieldnames(Device); %get all fieldnames for filenames
    basic_header = {'U_Sweep / [V]','U_Step_actual / [V]',...
    'I SourceDrain / [A]','I Gate / [A]','U_Step_nominal / [V]'};
    % Creat a basic header (here for transfer characteristics)

    for l = 1:SubFileCounter
        outfile = [foldername,'\',names{l},'.txt'];
```

```
        DataFile = eval(['Device.',names{l},'{1}']);
        % Header for .txt File
        Steps = size(DataFile,3); header_outfile={}; % number of steps
        % Writing only, Id, Vg, Vds. Ignoring other data
          if DataTypeArray(l) == 1
                index_data = [1,3,4]; %Transfer
          else
                index_data = [2,3,4]; %Output
          end
        MatrixData = cell2mat(DataFile); % Putting Data in Matrix form
        FormattedData = zeros(size(MatrixData,1),3*Steps);
% Preallocating Formatted Data Structure

        for k = 1:Steps
            I_SD = ['I_SD for U_SD = ',num2str(DataFile{k}(1,5)),'V / A'];
% writing Step SD Voltage in Header
            I_G = ['I_G for U_SD = ',num2str(DataFile{k}(1,5)),'V / A'];
            basic_header = {'U_Sweep / [V]',I_SD,I_G};
            header_outfile = [header_outfile,basic_header];
            StepData = MatrixData(:,index_data,k);
% Taking ImportantData from each Step series
            FormattedData(:,1+3*(k-1):3*k) = StepData;
% Adding Stepdata: 3 columns a step
        end

        header_outfile = [header_outfile,Header{l}(3)];
% Add Time Stamp to Header End

% writing header with fprint to append \n for importdata function
        fileID = fopen(outfile,'w');
        formatSpec = '%s\t';
        fprintf(fileID,formatSpec, header_outfile{1,:});
        fprintf(fileID,'\n');
        fclose(fileID);

        dlmwrite(outfile,FormattedData,'-append','delimiter','\t',...
        'newline','unix'); % writing Data
    end
end
```

6.1.2 Extraction of Mobility and Threshold Voltages

```
% Reading preprocessed data and extracting key value
clear all
close all

%% Fitting Parameters
% Fitting treshold data for values from I_max/Factor - I_max
Saturation_Division_Factor = 1.5; % Factor for saturation mobility
Linear_Division_Factor = 2; % Factor for linear mobility

%% Select Files and Load Data
[filename,pathname] = uigetfile('*.txt*','MultiSelect','on');
NumberOfFiles = length(filename); % Counting number of files
% Choosing SubFigure Size
if NumberOfFiles <= 6; SubFigSize = [3,2];elseif NumberOfFiles <= 12;
    SubFigSize = [4,3];
elseif NumberOfFiles <= 30; SubFigSize = [6,5]; else SubFigSize = [15,10];
end

AllData = {}; cd (pathname); % create cell and move to folder direction

for k = 1: NumberOfFiles
    ImportedData = importdata(filename{k},'\t');
    header = strsplit(ImportedData.textdata{1}, '\t');
% Split header to cell array
    header = [header,filename(k)];
% Append filename
    AllData(k).header = header;
    AllData(k).data = ImportedData.data;
end

Transfer_Data = strfind(filename,'Transfer'); %is transfer in filename?
emptyCells = cellfun(@isempty,Transfer_Data); % find empty cells
TransferFiles = find(emptyCells==0);
NumberOfTransfers = length(TransferFiles);
% choosing subfigure size for optimum representation
SubFigureSize = ceil(sqrt(NumberOfTransfers));
```

```
% predefining cell structure with expected size
DerivedData.Header = {'Filename','Slope','Treshhold','Mobility'};
DerivedData.Filename = cell(1,NumberOfTransfers);
DerivedData.Slope = zeros(1,NumberOfTransfers);
DerivedData.Treshhold_V = zeros(1,NumberOfTransfers);
DerivedData.Mobility = zeros(1,NumberOfTransfers);
DerivedData.Slope_linear = zeros(1,NumberOfTransfers);
DerivedData.Treshhold_V_linear = zeros(1,NumberOfTransfers);
DerivedData.Mobility_linear = zeros(1,NumberOfTransfers);

legend_timestamp = []; % for timestamp legends

%%
for m = 1:NumberOfTransfers
    %% Saturation Mobility
    % get 50V Data
    DataLength = size(AllData(TransferFiles(m)).data);
    highest_V = ...
    AllData(TransferFiles(m)).data(:,[DataLength(2)-2,DataLength(2)]);
    x = highest_V(:,1);
    y = highest_V(:,2);
    y_sqrt = sqrt(abs(y));    % square root plot

    % create mean values for "to and from" measurements
    s = size(y_sqrt); half_data = s(1)/2;
    y_mean_sqrt = (y_sqrt(1:half_data) +...
    flipud(y_sqrt(half_data+1:end)))./2;
    x_mean = (x(1:half_data) + flipud(x(half_data+1:end)))./2;

    % get slope by using only Imax to I_mac / Factor values;
    I_max = max(y_mean_sqrt)-min(y_mean_sqrt); % Max = Max - Min / Offsets
    I_half_logic = y_mean_sqrt >= I_max/Saturation_Division_Factor;
    if m == 2
        I_half_logic(1:25) = 0;
    end
    fit_parameter = polyfit(x_mean(I_half_logic),...
        y_mean_sqrt(I_half_logic),1);
    % Calculating Threshold, Slope, Saturation Mobility
    Treshhold_V = -fit_parameter(2)/fit_parameter(1);
    slope = fit_parameter(1);
```

```
mobility_saturation = (2*25)/(4000*23.02*10^-9)*slope^2;

%% Linear Mobility
DataLength_linear = size(AllData(TransferFiles(m)).data); linear_V =...
AllData(TransferFiles(m)).data(:,[4,6]); x_linear = linear_V(:,1);
y_linear = linear_V(:,2);
lin_MaxCurrent = max(abs(y_linear));
y_linear = abs(y_linear);
s_linear = size(y_linear);
half_data_linear = s_linear(1)/2;
y_mean_linear = (y_linear(1:half_data_linear) +...
flipud(y_linear(half_data_linear+1:end))./2;
x_mean_linear = (x(1:half_data) + flipud(x(half_data+1:end)))./2;
 % get slope over using I_max to I_max / Factor. I is actually sqrt I
I_max_linear = max(y_mean_linear)-min(y_mean_linear);
I_half_logic_linear = y_mean_linear >= ...
I_max_linear/Linear_Division_Factor;
fit_parameter_linear = polyfit(x_mean_linear(I_half_logic_linear),...
y_mean_linear(I_half_logic_linear),1);
% Calculate Threshold, Slope, Saturation Mobility
Treshhold_V_linear = -fit_parameter_linear(2)/fit_parameter_linear(1);
slope_linear = fit_parameter_linear(1);
% Calculating linear mobility, 3 V Data for 50V U_G are used
mobility_linear = 25/(4000*23.02*10^-9)*lin_MaxCurrent/...
((50-abs(Treshhold_V_linear))*3-4.5);

%%Write to Cell
DerivedData.Header = {'Filename','Slope','Treshhold','Mobility',...
'Slope_Lin','Treshhold_Lin','Mobility_Lin'};
% replacing chars causing erros
filename(TransferFiles(m)) = strrep(filename(TransferFiles(m)),'_','');
filename(TransferFiles(m)) = strrep(filename(TransferFiles(m)),...
'Transfer','');
filename(TransferFiles(m)) = strrep(filename(TransferFiles(m)),...
'.txt','');
filename(TransferFiles(m)) = strrep(filename(TransferFiles(m)),...
'P10','');
DerivedData.Filename(m) = filename(TransferFiles(m));
DerivedData.Slope(m) = slope;
DerivedData.Treshhold_V(m) = Treshhold_V;
```

```
    DerivedData.Mobility(m) = mobility_saturation;
    DerivedData.Slope_linear(m) = slope_linear;
    DerivedData.Treshhold_V_linear(m) = Treshhold_V_linear;
    DerivedData.Mobility_linear(m) = mobility_linear;

    figure(1) % Creating plot with polyfit data (Saturation Mobility)
    set(gca, 'box','off','TickDir','out','FontSize',8,'xMinorTick',...
    'on','YMinorTick','on','color','white');
    set(gcf,'color','white');
    subplot(SubFigureSize,SubFigureSize,m);
    plot(x_mean,y_mean_sqrt,'b-',x_mean,polyval(fit_parameter,x_mean),'-g')
    title(filename(TransferFiles(m)))
    grid on

    figure(2) % Creating plot with polyfit data (Linear Mobility)
    set(gca, 'box','off','TickDir','out','FontSize',8,'xMinorTick',...
    'on','YMinorTick','on','color','white');
    set(gcf,'color','white');
    subplot(SubFigureSize,SubFigureSize,m);
    plot(x_mean_linear,y_mean_linear,'b-',x_mean_linear,...
    polyval(fit_parameter_linear,x_mean_linear),'-g')
    title(filename(TransferFiles(m)))
    grid on
    % legend timestamps for mobility/treshhold plot
    timestamp = strrep(AllData(TransferFiles(m)).header(13), '_', '-');
    legend_timestamp = [legend_timestamp,timestamp{:},char(10)];
end

%% Plot Mobilities
figure(3)
x_data = 1:length(DerivedData.Mobility);
plot(1:length(x_data), DerivedData.Mobility, 'bo','MarkerSize',10,...
'MarkerFaceColor','b');
hold on
plot(1:length(x_data), DerivedData.Mobility_linear, 'ro',...
'MarkerSize',10,'MarkerFaceColor','r');
set(gca,'XTick',1:length(DerivedData.Mobility),'XTickLabel','')
lab = DerivedData.Filename';
hx = get(gca,'XLabel');  % Handle to xlabel
set(hx,'Units','data'); pos = get(hx,'Position'); ypos = pos(2);
```

```
for i = 1:size(lab,1)
    t(i) = text(x_data(i),ypos,lab{i,:});
end
set(t,'Rotation',10,'HorizontalAlignment','right')
legend(legend_timestamp);
grid on
set(gcf,'color','white');
ylabel('Mobility$_{Saturation}$ \ $\frac{cm^2}{Vs}$','interpreter','latex')
title('Saturation mobility (Blue) and Linear (Red) mobility')

%% Plot Threshold
figure(4)
x_data = 1:length(DerivedData.Mobility); % Plot with tilted x labels
plot(1:length(x_data), DerivedData.Treshhold_V, 'bo','MarkerSize',10,...
'MarkerFaceColor','b');
hold on
plot(1:length(x_data), DerivedData.Treshhold_V_linear, 'ro',...
'MarkerSize',10,'MarkerFaceColor','r');
set(gca,'XTick',1:length(DerivedData.Mobility),'XTickLabel','')
lab = DerivedData.Filename';
hx = get(gca,'XLabel');  % Handle to xlabel
set(hx,'Units','data'); pos = get(hx,'Position'); ypos = pos(2);
for i = 1:size(lab,1)
    t(i) = text(x_data(i),ypos,lab{i,:});
end
set(t,'Rotation',10,'HorizontalAlignment','right')
grid on
set(gcf,'color','white');
legend(legend_timestamp);
ylabel('Treshhold Voltage / V')
title('Treshhold Voltage (blue-Saturation / red-Linear ')

%% Plot Transfers
%Defining colors for different TransferLines:
colors = {'k','r','b','g','m','y','c','k--','r--','b--','g--','m--',...
'y--','c--','k-.','r-.','b-.','g-.','m-.','y-.','c-.'};
colors = [colors colors colors colors colors colors];
data_legend = []; legend_names = [];

figure(5) % Plotting transfer lines in saturation regime / SemiLog
```

```
for m = 1:NumberOfTransfers
    % Plotting Line of each Step
    DataLength = size(AllData(TransferFiles(m)).data);
    highest_V = AllData(TransferFiles(m)).data(:,[DataLength(2)-2,DataLength(2)]);
    h(m) = semilogy(highest_V(:,1),abs(highest_V(:,2)),colors{m});
    % Plotting style
    set(h(m),'LineWidth',2);  hold on
    % Generating plot handle vector and legend names
    data_legend = [data_legend;h(m)];
    legend_names = [legend_names;DerivedData.Filename(m)];
end
% replacing strings that lead to error when used in legend
legend_names = strrep(legend_names, '_', '-');
% Plotting style
set(gca, 'box','off','TickDir','out','FontSize',14,'xMinorTick','on','YMinorTick','on',
set(gcf,'color','white');
l = legend(data_legend,legend_names{:});
set (l,'location','NorthWest')
grid on
title('Transfer Lines - 50V')
xlabel('$U_{GS}$ / V','interpreter','latex')
ylabel('$I_{DS}$ / V','interpreter','latex')
data_legend = []; % resetting legend entries

figure(6) % Plotting transfer lines in linear regime / linear
for m = 1:NumberOfTransfers
    % Plotting Line of each Step
    DataLength = size(AllData(TransferFiles(m)).data);
    linear_V = AllData(TransferFiles(m)).data(:,[4,6]);
    k(m) = plot(linear_V(:,1),linear_V(:,2),colors{m});
    % Plotting style
    set(k(m),'LineWidth',2);   hold on
    % Generating plot handle vector and legend names
    data_legend = [data_legend;k(m)];
end
title('Transfer Lines - 3V')
xlabel('$U_{GS}$ / V','interpreter','latex')
ylabel('$I_{DS}$ / V','interpreter','latex')
% replacing strings that lead to error when used in legend
legend_names = strrep(legend_names, '_', '-');
```

```
% Plotting style
set(gca, 'box','off','TickDir','out','FontSize',14,'xMinorTick','on','YMinorTick','on',
set(gcf,'color','white');
l = legend(data_legend,legend_names{:});
set (l,'location','NorthWest')
grid on
```

List of Figures

2.1 Structural and skeletal formula of benzene. 5
2.2 Orbitals of a benzene molecule 6
2.3 Ball and stick model and STM image of the pentacene molecule 7
2.4 Pentacene in thin film and bulk phase with inter-planar spacings of $d_{001} = 15.4\,\text{Å}$ and $d_{001} = 14.4\,\text{Å}$, respectively. 8
2.5 Growth of pentacene on gold. 9
2.6 Growth modes of epitaxial films. 11
2.7 Diffusing pentacene monomers may overcome the Ehrlich-Schwoebel barrier in both directions. 12
2.8 Nomenclature of transistor structures for thin semiconducting films [28]. The figure shows a matrix of bottom and top gate contacted devices with SC between gate and electrodes (*staggered*) or on the dielectric (*coplanar*). 14
2.9 Geometrical setup of a coplanar bottom gate transistor. 15
2.10 OFET operating regimes with schematic output characteristic. 18
2.11 Output curves of self manufactured pentacene OFETs 19
2.12 Transfer curves of self manufactured pentacene OFETs 20
2.13 Extraction of the threshold voltage. 21
2.14 Lowering of vacuum level E_{vac} at the pentacene-gold interface due to polarization Δ_{dip}. 23

3.1 Vacuum chambers used for preparation and investigation of thin films. . 28
3.2 Sample holder and draft of its arrangement. 29
3.3 Pictures of evaporation unit and QMS. 30
3.4 Examples for TDS spectra of different orders of desorption. 32
3.5 Nanosurf EasyScan 2 - instrument and working principle of atomic force microscopy. 35

4.1 Development of carbon contamination on SiO_2, before, and after deposition, as well as after desorption with consecutive sputter-cleaning (Ch. 3.2.3). 39
4.2 AFM topography images with corresponding roughness values. 40
4.3 AFM 3D topography image of the gold-SiO_2 transition area. 41
4.4 AFM topography image of an US cleaned sample. 42
4.5 Topography image of a specimen with a 30 Hz pentacene layer deposited at 300 K on SiO_2. 44
4.6 TDS spectra of pentacene films of different thicknesses and prepared at different temperatures. 46
4.7 Threshold marked AFM images of a 10.5 nm specimen prepared at 300 K. 48
4.8 Optical microscopy images of the OFET channel prepared at T =200 K, 300 K and 350 K with 500 Hz, 150 Hz and 150 Hz, respectively. 50
4.9 Coverage dependencies of OFET saturation mobilities. 52
4.10 AFM images (derived data) of pentacene films on SiO_2 substrate with a nominal thickness of 1.4 ML for preparation temperatures of **(a.)** 200 K, **(b.)** 300 K, **(c.)** 350 K. 53
4.11 AFM images (derived data) of pentacene films on gold substrate with a nominal thickness of 1.4 ML for preparation temperatures of **(a.)** 200 K, **(b.)** 300 K, **(c.)** 350 K. 54
4.12 AFM images (derived data) of pentacene films in transition area with a nominal thickness of 1.4 ML for preparation temperatures of **(a.)** 200 K, **(b.)** 300 K. **(c.)** Coverage of 2.2 ML at T = 350 K. 56
4.13 Sample with a coverage of 2.2 ML deposited at 350 K. 57
4.14 AFM images (derived data) of pentacene films on SiO_2 substrate with a nominal thickness of 6.8 ML for preparation temperatures of **(a.)** 200 K, **(b.)** 300 K, **(c.)** 350 K. 59
4.15 AFM (3D) images of a pentacene film prepared at 200 K. 60
4.16 AFM images (derived data) of pentacene films on gold substrate with a nominal thickness of 6.8 ML for preparation temperatures of **(a.)** 200 K, **(b.)** 300 K, **(c.)** 350 K. 61
4.17 AFM images (derived data) of pentacene films in transition area with a nominal thickness of 6.8 ML for preparation temperatures of **(a.)** 200 K, **(b.)** 300 K, **(c.)** 350 K. 62

4.18 AFM close ups of 300 K and 350 K films. 63
4.19 AFM images (derived data) of pentacene films on SiO_2 substrate with a nominal thickness of 22.7 ML for preparation temperatures of **(a.)** 200 K, **(b.)** 300 K, **(c.)** 350 K. 65
4.20 AFM images (derived data) of pentacene films on gold substrate with a nominal thickness of 22.7 ML for preparation temperatures of **(a.)** 200 K, **(b.)** 300 K, **(c.)** 350 K. 66
4.21 AFM images (derived data) of pentacene films in transition area with a nominal thickness of 22.7 ML for preparation temperatures of **(a.)** 200 K, **(b.)** 300 K, **(c.)** 350 K. 67
4.22 AFM images (derived data) of the pentacene film on sputter-cleaned SiO_2 substrate with a nominal thickness of 6.8 ML. 68
4.23 Comparison of coverage dependent mobilities for carbon contaminated and previously sputter-cleaned samples. 69
4.24 Development of threshold voltage with coverage. 71

7 Bibliography

[1] H. E. Katz and J. Huang, "Thin-film organic electronic devices," *Ann. Rev. Mater. Res.*, vol. 39, no. 1, p. 71, 2009.

[2] Y. Guo, G. Yu, and Y. Liu, "Functional organic field-effect transistors," *Adv. Mater.*, vol. 22, no. 40, p. 4427, 2010.

[3] G. Horowitz, R. Hajlaoui, and P. Delannoy, "Temperature dependence of the field-effect mobility of sexithiophene. determination of the density of traps," *J. Phys. III*, vol. 5, p. 355, Apr. 1995.

[4] G. Horowitz, M. E. Hajlaoui, and R. Hajlaoui, "Temperature and gate voltage dependence of hole mobility in polycrystalline oligothiophene thin film transistors," *J. Appl. Phys.*, vol. 87, p. 4456, May 2000.

[5] V. Coropceanu, J. Cornil, D. A. da Silva Filho, Y. Olivier, R. Silbey, and J.-L. Brédas, "Charge transport in organic semiconductors," *Chem. Rev.*, vol. 107, p. 926, Apr. 2007.

[6] M. Kitamura and Y. Arakawa, "Pentacene-based organic field-effect transistors," *J. Phys.: Condens. Matter*, vol. 20, p. 184011, May 2008.

[7] Y. Yamashita, "Organic semiconductors for organic field-effect transistors," *Sci. Technol. Adv. Mater.*, vol. 10, p. 024313, Apr. 2009.

[8] R. Ruiz, D. Choudhary, B. Nickel, T. Toccoli, K.-C. Chang, A. C. Mayer, P. Clancy, J. M. Blakely, R. L. Headrick, S. Iannotta, and G. G. Malliaras, "Pentacene thin film growth," *Chem. Mater.*, vol. 16, p. 4497, Nov. 2004.

[9] T. Kakudate, N. Yoshimoto, and Y. Saito, "Polymorphism in pentacene thin films on SiO_2 substrate," *Appl. Phys. Lett.*, vol. 90, p. 081903, Feb. 2007.

[10] M. Fiebig and D. Beckmeier, "Thickness-dependent in situ studies of trap states in pentacene thin film transistors," *Appl. Phys. Lett.*, vol. 96, no. 8, p. 083304, 2010.

[11] B.-N. Park, S. Seo, and P. G. Evans, "Channel formation in single-monolayer pentacene thin film transistors," *J. Phys. D: Appl. Phys.*, vol. 40, p. 3506, June 2007.

[12] S. C. B. Mannsfeld, A. Virkar, C. Reese, M. F. Toney, and Z. Bao, "Precise structure of pentacene monolayers on amorphous silicon oxide and relation to charge transport," *Adv. Mater.*, vol. 21, p. 2294, June 2009.

[13] Wikipedia, "By vladsinger [cc-by-sa-3.0 (http://creativecommons.org/licenses/by-sa/3.0) or gfdl (http://www.gnu.org/copyleft/fdl.html)], via wikimedia commons," 2013. [Online; Stand 24. Oktober 2014].

[14] Z. Bao and J. Locklin, *Organic Field-Effect Transistors*. CRC Press, May 2007.

[15] L. Gross and F. Mohn, "The chemical structure of a molecule resolved by atomic force microscopy.," *Science (New York, N.Y.)*, vol. 325, no. 5944, p. 1110, 2009.

[16] C. C. Mattheus, A. B. Dros, J. Baas, A. Meetsma, J. L. d. Boer, and T. T. M. Palstra, "Polymorphism in pentacene," *Acta Crystallogr., Sect. C*, vol. 57, p. 939, Aug. 2001.

[17] L. B. Roberson, J. Kowalik, L. M. Tolbert, C. Kloc, R. Zeis, X. Chi, R. Fleming, and C. Wilkins, "Pentacene disproportionation during sublimation for field-effect transistors," *J. Am. Chem. Soc.*, vol. 127, p. 3069, Mar. 2005.

[18] V. Butko, X. Chi, D. Lang, and A. Ramirez, "Field-effect transistor on pentacene single crystal," *Appl. Phys. Lett.*, vol. 83, p. 4773, Dec. 2003.

[19] D. Nabok, P. Puschnig, C. Ambrosch-Draxl, O. Werzer, R. Resel, and D.-M. Smilgies, "Crystal and electronic structures of pentacene thin films from grazing-incidence x-ray diffraction and first-principles calculations," *Phys. Rev. B*, vol. 76, p. 235322, Dec. 2007.

[20] H. Yoshida, K. Inaba, and N. Sato, "X-ray diffraction reciprocal space mapping study of the thin film phase of pentacene," *Appl. Phys. Lett.*, vol. 90, p. 181930, Apr. 2007.

[21] D. Käfer, L. Ruppel, and G. Witte, "Growth of pentacene on clean and modified gold surfaces," *Phys. Rev. B*, vol. 75, p. 085309, Feb. 2007.

[22] E. Bauer, "Phänomenologische Theorie der Kristallabscheidung an Oberflächen. I," *Z. Kristallogr.*, vol. 110, p. 372, Jan. 1958.

[23] P. Jensen, "Growth of nanostructures by cluster deposition: Experiments and simple models," *Rev. Mod. Phys.*, vol. 71, p. 1695, Oct. 1999.

[24] B. Stadlober, U. Haas, H. Maresch, and A. Haase, "Growth model of pentacene on inorganic and organic dielectrics based on scaling and rate-equation theory," *Phys. Rev. B*, vol. 74, p. 165302, Oct. 2006.

[25] H. Zhu, Q. L. Li, X. J. She, and S. D. Wang, "Surface roughening evolution in pentacene thin film growth," *Appl. Phys. Lett.*, vol. 98, p. 243304, June 2011.

[26] D. Käfer, C. Wöll, and G. Witte, "Thermally activated dewetting of organic thin films: the case of pentacene on SiO_2 and gold," *Appl. Phys. A*, vol. 95, p. 273, Apr. 2009.

[27] H. Shirakawa, E. J. Louis, A. G. MacDiarmid, C. K. Chiang, and A. J. Heeger, "Synthesis of electrically conducting organic polymers: halogen derivatives of polyacetylene, (CH)x," *Chem. Commun.*, no. 16, p. 578, 1977.

[28] Wikipedia, "Cepheiden [gfdl (http://www.gnu.org/copyleft/fdl.html) or cc-by-sa-3.0-2.5-2.0-1.0 (http://creativecommons.org/licenses/by-sa/3.0)], via wikimedia commons," 2013. [Online; Stand 24. Oktober 2014].

[29] M. Weis, "Gradual channel approximation models for organic field-effect transistors: The space-charge field effect," *J. Appl. Phys.*, vol. 111, p. 054506, Mar. 2012.

[30] G. Horowitz, "Organic field-effect transistors," *Adv. Mater.*, vol. 10, p. 365, Mar. 1998.

[31] C. H. Kim and A. Castro-Carranza, "A compact model for organic field-effect transistors with improved output asymptotic behaviors," *IEEE Transactions on Electron Devices*, vol. 60, no. 3, p. 1136, 2013.

[32] J. J. Brondijk, F. Torricelli, E. C. P. Smits, P. W. M. Blom, and D. M. de Leeuw, "Gate-bias assisted charge injection in organic field-effect transistors," *Org. Electron.*, vol. 13, p. 1526, Sept. 2012.

[33] F. Amy, C. Chan, and A. Kahn, "Polarization at the gold/pentacene interface," *Org. Electron.*, vol. 6, no. 2, p. 85, 2005.

[34] D. R. Lide, *CRC Handbook of Chemistry and Physics, 85th Edition*. CRC Press, June 2004.

[35] R. M. Hochstrasser, "Organic molecular crystals: interaction, localization and transport phenomena by E. A. Silinsh and V. Cápek," *Acta Crystallogr., Sect. A: Found. Crystallogr.*, vol. 53, p. 855, Nov. 1997.

[36] E. J. Meijer, *Charge transport in disordered organic field-effect transistors*. Doctoral Thesis, Delft University of Technology, June 2003.

[37] K. Oura *et al.*, eds., *Surface science: an introduction*. Advanced texts in physics, Berlin, New York: Springer, 1. Aufl. ed., 2003.

[38] D. Ricci and P. C. Braga, "Recognizing and avoiding artifacts in AFM imaging," in *Atomic Force Microscopy* (P. C. Braga and D. Ricci, eds.), no. 242 in Methods in Molecular Biology, p. 25, Humana Press, Jan. 2004.

[39] F. Gołek, P. Mazur, Z. Ryszka, and S. Zuber, "AFM image artifacts," *Appl. Surf. Sci.*, vol. 304, p. 11, June 2014.

[40] B. Nickel, "Pentacene devices: Molecular structure, charge transport and photo response," in *Organic Electronics* (C. Wöll, ed.), p. 299, Wiley-VCH Verlag GmbH & Co. KGaA, 2009.

[41] D. Guo, S. Ikeda, and K. Saiki, "Pentacene films grown on surface treated SiO_2 substrates," *Thin Solid Films*, vol. 515, p. 814, Oct. 2006.

[42] G. Sauerbrey, "Verwendung von Schwingquarzen zur Wägung dünner Schichten und zur Mikrowägung," *Z. Physik*, vol. 155, p. 206, Apr. 1959.

[43] B. Nickel, M. Fiebig, S. Schiefer, M. Göllner, M. Huth, C. Erlen, and P. Lugli, "Pentacene devices: Molecular structure, charge transport and photo response," *phys. stat. sol. (a)*, vol. 205, no. 3, p. 526, 2008.

[44] R. Lassnig, B. Striedinger, M. Hollerer, A. Fian, B. Stadlober, and A. Winkler, "In situ preparation, electrical and surface analytical characterization of pentacene thin film transistors," *J. Appl. Phys.*, vol. 116, p. 114508, Sept. 2014.

[45] S. Sreenivasan, D. R. Baker, G. Paul, and H. E. Stanley, "The approximate invariance of the average number of connections for the continuum percolation of squares at criticality," *Physica A*, vol. 320, p. 34, Mar. 2003.

[46] R. Ruiz, B. Nickel, N. Koch, L. Feldman, R. Haglund, A. Kahn, and G. Scoles, "Pentacene ultrathin film formation on reduced and oxidized Si surfaces," *Phys. Rev. B*, vol. 67, p. 125406, Mar. 2003.

[47] I. Yagi, K. Tsukagoshi, and Y. Aoyagi, "Growth control of pentacene films on SiO_2 / Si substrates towards formation of flat conduction layers," *Thin Solid Films*, vol. 467, p. 168, Nov. 2004.

[48] M. P. Seah and S. J. Spencer, "Ultrathin SiO_2 on Si. I. Quantifying and removing carbonaceous contamination," *J. Vac. Sci. Technol., A*, vol. 21, p. 345, 2003.

[49] D. Knipp, R. A. Street, A. Völkel, and J. Ho, "Pentacene thin film transistors on inorganic dielectrics: Morphology, structural properties, and electronic transport," *J. Appl. Phys.*, vol. 93, p. 347, Jan. 2003.

[50] K. Suemori, S. Uemura, M. Yoshida, S. Hoshino, N. Takada, T. Kodzasa, and T. Kamata, "Influence of fine roughness of insulator surface on threshold voltage stability of organic field-effect transistors," *Appl. Phys. Lett.*, vol. 93, p. 033308, July 2008.

[51] A. R. Völkel, R. A. Street, and D. Knipp, "Carrier transport and density of state distributions in pentacene transistors," *Phys. Rev. B*, vol. 66, p. 195336, Nov. 2002.

[52] J. Lee, J. H. Kim, S. Im, and D.-Y. Jung, "Threshold voltage change due to organic-inorganic interface in pentacene thin-film transistors," *J. Appl. Phys.*, vol. 96, p. 2301, Aug. 2004.